EMERGENT PROPERTIES OF SMALL SYSTEMS OF TRAPPED ULTRACOLD ATOMS

A Dissertation
Presented to
The Academic Faculty

By

Benedikt Bruno Brandt

In Partial Fulfillment
of the Requirements for the Degree
Doctor of Philosophy in the
School of Physics

Georgia Institute of Technology

August 2018

EMERGENT PROPERTIES OF SMALL SYSTEMS OF TRAPPED ULTRACOLD ATOMS

Approved by:

Prof. Uzi Landman
School of Physics
Georgia Institute of Technology

Dr. Constantine Yannouleas
School of Physics
Georgia Institute of Technology

Prof. Michael Pustilnik
School of Physics
Georgia Institute of Technology

Prof. Mostafa El-Sayed
School of Chemistry and Biochemistry
Georgia Institute of Technology

Prof. Martin Mourigal
School of Physics
Georgia Institute of Technology

Date Approved: July 13, 2018

To Agnes and Michael, my wonderful parents, without whose support and encouragement none of this would have been possible.

ACKNOWLEDGEMENTS

Many people have supported and encouraged me during the course of my studies. First I want to thank my professor Uzi Landman for his dedicated mentoring and the support that he provided during my PhD. His guidance was essential for completing my PhD and enabled steady progress, resulting in five published papers. Furthermore I want to thank Dr. Constantine Yannouleas for his extensive advising and the many patient explanations on various aspects of quantum physics. The quantum physics and numerical computing skills that I acquired thanks to Uzi and Constantine, will serve me well in my future career.

I also want to express my gratitude to Prof. Michael Pustilnik, who has been member of my thesis committee since the initial thesis proposal and to Prof. Martin Mourigal and Prof. Mostafa El-Sayed for serving on my thesis committee.

Furthermore, I want to thank Chris Crowley, for the many great, humorous and uplifting conversations over the last five years. I also want to thank Jean Philipp, Oliver Pierson and the students who joined the program with me in 2013 for the welcoming attitude and the good camaraderie.

I am also deeply grateful to my friends from ORGT, Morris Satin, David MacNair, Aaron Mosher, Michael Delfanti and many more, who made my time at Georgia Tech a pleasant one and helped me maintain a good work life balance.

TABLE OF CONTENTS

*

LIST OF TABLES

LIST OF FIGURES

CHAPTER 1
INTRODUCTION AND LITERATURE REVIEW

Today the preparation, control and measurement of trapped ultracold atoms is one of the most actively researched fields in physics. Systems of ultracold atoms are very well isolated from their external environment and they are virtually unaffected by thermal noise due to their ultra low temperature. This makes them ideal systems to explore fundamental questions in quantum mechanics and there are a multitude of promising experimental applications to be realized and theoretical insights to be gained. The following sections give a brief historical overview over the field and how it developed and situate this thesis within the current experimental and theoretical effort.

1.1 The beginnings of laser cooling and trapping

The foundations of laser cooling and trapping were laid 50 years ago, when the idea to trap atoms with laser light first surfaced in 1968 with a proposal by Letokhov [1] and in 1970 by Ashkin [2]. Laser-cooling was introduced by T.W. Hänsch and A.L. Schawlow in 1975 with a proposal to use counter-propagating laser beams to cool neutral atoms [3]. The laser beams would be tuned slightly below an electronic transition so that atoms flying towards a laser source absorb photons due to the Doppler shift in laser frequency. The resulting momentum transfer from the photons slows the atoms. Due to the underlying Doppler effect this cooling technique is known as Doppler cooling. In the 1970s and 80s further theoretical and experimental progress followed that advanced the ideas of laser cooling and trapping [4–6]. However it would take until 1985 for the first experimental observations of trapped ultracold neutral atoms to be achieved [7–10]. In 1987 the magneto-optical trap (MOT) was developed [11] which would become a cornerstone of many modern cold atom experiments.

In 1988 precise temperature measurements of the laser cooled atoms revealed a temperature that was below the theoretical limit for Doppler cooling [12]. Study of this phenomenon yielded new insights into cooling techniques and led to the establishment of sub-Doppler (Sisyphus) cooling in which multiple atomic energy levels are contributing to the cooling process [13]. Since laser cooling involves the absorption and re-emission of a photon the fundamental limit to the cooling temperature now seemed to be the recoil energy, which is bestowed onto the atom by the emission of a single photon.

But even this barrier was soon overcome by the development of velocity selective coherent population trapping (VSCPT), in which atoms with energies below the recoil temperature are optically pumped into a non-absorbing dark state and become invisible to the doppler cooling lasers [14–16].

All these developments were honored in 1997 when Chu, Cohen-Tannoudji and Phillips won the Nobel Price in physics for their foundational contributions to laser cooling and trapping [17]. *Detailed information on laser cooling and trapping can be found in many reviews and books on the topic, i.e. [17–21].*

Another big step in cooling technology for atoms was the development of evaporative cooling, pioneered by Hess in 1986 [22]. The idea behind evaporative cooling is to let the highest energy atoms escape the trap until only the low energy and therefore coldest atoms are left. This is experimentally achieved by slowly lowering the barriers that are trapping the atomic gas, so that the higher energy atoms will spill (tunnel) out of the trap.

1.2 Ultracold bose and fermi gases

It was the combination of laser cooling techniques with evaporative cooling that led to the next breakthrough discovery in cold atom physics. After having been theoretically proposed by Einstein in 1925 [23, 24], the experimental techniques had finally advanced enough to measure a BEC. In 1995 several groups realized Bose Einstein Condensation (BEC) in dilute gases [25–27]. The physical significance of this discovery was immediately

evident and only six years later in 2001, the Nobel Price in Physics was awarded to Carl Wieman, Eric Allin Cornell and Wolfgang Ketterle [17] for being the first to experimentally measure a BEC [25, 26]. *Further details on the history and creation of BECs can be found in many good reviews on the topic, i.e. [28–32].*

But the experimental revolution wasn't restricted to just bosons. Only a few years after the initial discovery of the BEC, degenerate Fermi gases were realized [33]. This development was particularly intriguing since ultracold Fermi gases exhibit an even richer phase diagram than Bose gases. Groundwork for the understanding of this phase diagram was laid in 1957 when Bardeen, Cooper and Schrieffer (BCS) proposed the BCS theory explaining superconductivity by the formation of Cooper pairs [34]. For their work they were awarded the Nobel price in physics in 1972 [35]. The BCS theory had originally been developed to explain superconductivity in solids, more than 10 years before ultracold atom experiments were even envisioned, but connections soon became apparent, i.e. a weakly attractive gas of ultracold spin $1/2$ fermions should be able to form cooper pairs and be described by BCS theory. Furthermore Eagles (in 1969) and Leggett (in 1980) independently realized that the BCS wavefunction is able to describe an evolution from a BCS state to a BEC [36–38]. The basic idea being that weakly repelling fermions should be able to form pairs which obey Bose statistics and condense into a BEC. Further theoretical studies predicted that close to the unitary limit (near infinite interaction strength) the fermions exhibit yet another superfluid phase [21, 39, 40]. Trapped ultracold gases finally allowed experimental observation of these states. The crossover region at the unitary limit was first studied in 2002 [41, 42], Fermionic dimers (the BEC region) were discovered in 2003 [43–46] and in 2004 superfluidity of fermionic pairs (the BCS region) was observed [47, 48]. *Reviews with information on the topic of ultracold fermionic gases and the BEC-BCS crossover are i.e. [38, 49, 50].*

A key characteristic feature of systems of ultracold atoms that made the experimental observation of the BCS-BEC transition possible is the tunability of the interaction strength.

This is enabled by exploiting Fano-Feshbach resonances [51, 52]. If the energy of the scattering process between two particles in a certain spin state (the so called open channel) is close to the bound state energy of the pair in a different spin state (the so called closed channel) the scattering length diverges. If the magnetic moments of these two spin states are different one can tune the energy difference between these two states by varying an external magnetic field. This changes the scattering length (and therefore the interaction strength) [50]. Today Fano-Feshbach resonances are a cornerstone of ultracold atom experiments. *For an extensive review of Fano-Feshbach resonances in ultracold gases see [53].*

1.3 Ultracold atoms as quantum simulators

So far we have reviewed experiments involving a single trap, which only represents a small part of the ultracold atom landscape. A multitude of interesting systems have been experimentally realized using optical lattices. The reason for the tremendous attention that optical lattices are given lies in the promise of using them as quantum simulators. Richard Feynman first suggested quantum simulators in 1982 [54, 55]. The idea is to solve "simplified theoretical models" like the Hubbard model (which are still too difficult to tackle analytically or with conventional computers) with a quantum simulator. One can think of quantum simulators as special-purpose quantum computers which are good at solving specific tasks, i.e. finding the solution to a particular minimization problem or to a specific Hamiltonian. General purpose quantum computers in contrast would be build from quantum logic gates and would be able to tackle any problem for which a quantum computing algorithm exists.

But first the optical lattice system and the experimental techniques had to be better understood. The first experimental measurements in optical lattices in the early 90s were focused on the atomic motion of atoms in the lattice [56–59] and the first imaging techniques to observe the atoms in the lattice were developed in 1995 [60, 61]. Soon Bloch oscillations [62] and Wannier-Stark ladders [63] were observed. Experiments with bosonic BECs loaded into optical lattices shortly followed [64–66]. But none of these systems had

been a true quantum simulator yet. This however was about to change. The possibility of simulating the superfluid to Mott insulator transition in an optical lattice had been first proposed in a seminal paper by Jacksch et al [67] in 1998. According to this proposal the superfluid and Mott insulating states of the Bose Hubbard model can be accessed using atoms in optical lattices at different interaction strengths, which would arguably be the first true experimental simulation of a model Hamiltonian. This was achieved and reported in a seminal paper by Greiner, Mandel, Esslinger, Hänsch und Bloch in 2002 [68]. While the first experiments mostly involved bosons or Bose-Fermi mixtures [68–73], the rapidly progressing developments in optical lattices and Feshbach resonances enabled the creation of a fermionic Mott insulators [74, 75] and great technological and experimental advances have been made [21, 69, 70, 76–80]. Among them are the realization of a one dimensional Tonks-Girardeau gas in 2004 [81] and the observation of a Kosterlitz-Thouless-Berezinskii transition (KTB) in 2 dimensions [82–85]. In 2016 Thouless and Kosterlitz, together with Haldane, won the Nobel Price "for theoretical discoveries of topological phase transitions and topological phases of matter" part of which was the prediction of the KTB transition [86].

Presently quantum simulators with applications in the analysis of quantum magnetism [87–91], high T_c superconductivity [80, 92], the study of topological insulators [92] and the quantum Hall effect [92] are envisioned and systems of ultracold atoms are also promising candidates for scalabale quantum computation [93–95]. Interest in these systems is further driven by significant advances in experimental techniques that allow the creation of optical lattices with a well defined number of particles [96–100].

There are two main experimental avenues for realizing ultracold atom systems in optical lattices. One is to use an extended array of optical traps forming an optical lattice with a large number of sites and particles (on the order of 10^3 [96]), like the one used by Greiner in 2002 [68]. These systems are very promising to study ensembles of small quantum systems and allow to probe many body physics like quantum phases and fermi

surfaces [101]. They offer a top down approach to quantum simulation and high T_c superconductivity [80]. The downside to such a top down approach is that one doesn't have individual control over specific sites in the lattices. The other experimental approach aims at unraveling these phenomena from the bottom up using few particles and few sites. In this approach one uses optical tweezers [102, 103] to trap the ultracold atoms and a lot of progress has been made on single [97, 98, 100, 104, 105] and double trap [99, 106, 107] experiments with a selected number of atoms. While theses systems are harder to scale to a large number of sites, they allow pristine control over the external potentials and the interatomic interactions, which makes them a most highly desirable building block for larger systems. Consequently a strong experimental and theoretical effort is currently aimed at understanding these systems. *There are many good reviews on optical lattice and tweezer experiments, i.e. [21, 49, 50, 108].*

To date most bottom-up experimental studies have focused on the quantum magnetism in single-trap systems with a few ultracold atoms in 1D [109–112]. The appeal of these systems is that theoretical solutions are known in certain limits like the non-interacting limit or the infinitely repulsive Tonks-Giradeau limit [113–115] (also called the fermionization limit [98]). Away from the infinitely repulsive limit some theoretical solutions for 1D harmonically trapped systems have been obtained using a Lippman-Schwinger equation approach [116–118]. However despite these results a comprehensive theoretical understanding and analysis for arbitrary interaction strengths and more complex geometries has been lacking.

Given the complexity of these systems and the experimental challenges to control few ultracold atoms with high fidelity, theoretical guidance is paramount for future developments. This thesis aims to provide some of the previously lacking theoretical understanding. We investigate few-particle few-site ultracold atom systems, in particular two, three and four ultracold atoms in single, double and multi-well confinement. A central challenge in studying these systems are the strong correlations that are present for intermediate and

strong interactions. It is therefore imperative to go beyond mean field methods. In this thesis we are using a numerical diagonalization method to study the microscopic Hamiltonian that yields accurate results for all interaction strengths. This method is known as full configuration interaction (full CI) [119] and, given a sufficiently large basis set, provides an exact solution to the Hamiltonian. We further augment our full CI results with analytical results based on effective spin models and establish guidance when such effective spin models are sufficient for the description of the microscopic Hamiltonian. We hope that these results provide a useful foundation for both experimentalists and theorists.

1.4 Structure of this thesis

This thesis is organized as follows:

- In chapter 2 we give a detailed description of our microscopic Hamiltonian and the methodology that we employ to solve it. Furthermore we explain several methods of studying the resulting many body wavefunctions, e.g. single particle densities, natural orbitals, higher order correlation functions and entanglement.

- In chapter 3 we give an introduction to several spin models that are used throughout this thesis. Those spin models assist in the later sections of this thesis with the interpretation of our CI results. The comparison with our CI results also allows us to explore the validity of the spin models for different parameter ranges.

- In chapter 4 we describe the main results from our Nano Letters paper that we published in 2015 [120]. In this chapter we study the two-particle double well system at varying interaction strengths and analyze the entanglement properties of the particles.

- In chapter 5, which is based on our New Journal of Physics paper [121], we analyze a double well systems with three and four particles in a linear and parallel configuration. We place particular emphasis on the Wigner molecule formation that enables

the mapping to Heisenberg and $t-J$ models and we compare and assess the accuracy of these spin models against our microscopic CI results.

- In chapter 6 we analyze the building block of unconventional superconductivity - a single plaquette. This chapter is based on our publication [122] and studies the appearance of an RVB state and the formation of pairing gap. We compare our CI results with results from the Hubbard model and describe circumstances in which the standard Hubbard model fails to produce the correct results.

- In chapter 7 we describe the results from our PRA paper [123] that was published in 2017. This chapter focuses on second-order correlation maps in position and momentum space as they have recently become experimentally accessible. We show detailed CI results and provide an analytical methodology based on the Heisenberg model to accurately calculate the 2nd order correlation maps.

- In chapter 8, which is based on our publication [124], we extend our analysis from [123] to a wide range of interactions and introduce an analytical modeling procedure based on the Hubbard model that is able to yield the correct correlation maps for all values of the interaction strength.

CHAPTER 2

MICROSCOPIC HAMILTONIAN AND METHODOLOGY

This chapter provides a detailed explanation of the Hamiltonian and the methods used in this thesis. In section 2.1 we introduce the Hamiltonian in full generality and describe the 2-body interaction terms used in this thesis. In the sections that follow we specialize the Hamiltonian to particular confining potentials. The double well potential is described in section 2.2, the triple and quadruple well potential is described in section 2.3, the single plaquette potential is described in section 2.4 and the multi plaquette potential is described in section 2.5. We then discuss numerical methods for solving our microscopic Hamiltonian in section 2.6. Afterwards, in section 2.7, we explain several approaches that are used to analyze and understand the resulting wavefunction (i.e single particle density (SPD) and conditional probability densities (CPDs)). In the last section of this chapter (section 2.8) we introduce position and momentum space density matrices and correlation maps.

> This chapter is intended to serve as a reference and can therefore be skipped until the details become relevant to the reader.

2.1 General form of the Hamiltonian

The Hamiltonians we are considering in this thesis are 2-dimensional ($\boldsymbol{r} = (x, y)$) and can be written in their most general form as:

$$H = \sum_{i=1}^{N} H(i) + \sum_{i=1}^{N} \sum_{j>i}^{N} V(\boldsymbol{r_i}, \boldsymbol{r_j}) \tag{2.1}$$

where:

N:	number of particles
$H(i)$:	single particle Hamiltonian
$V(\boldsymbol{r_i}, \boldsymbol{r_j})$:	interaction potential
$\boldsymbol{r_i}, \boldsymbol{r_j}$:	position of particle i, j

The interaction potential $V(\boldsymbol{r_i}, \boldsymbol{r_j})$ is a short range Gaussian or delta function potential, see Equation 2.3 and Equation 2.4 respectively. The single particle Hamiltonian $H(i)$ contains the kinetic energy terms and the external confining potential. $H(i)$ is given as

$$H(i) = \frac{p_{yi}^2}{2m} + \frac{p_{xi}^2}{2m} + V_x(x_i) + V_y(y_i) \tag{2.2}$$

---

where:

x_i, y_i:	x and y coordinates of particle i
V_x:	the external potential in the x-direction
V_y:	the external potential in the y-direction
m:	is the mass of the atoms

As is evident by the form of our single particle Hamiltonian $H(i)$, in this thesis we are only considering external confining potentials that are separable in x and y. In order to realize different systems (single well, double well, single plaquette, etc.) we change the potential terms V_x and V_y. Section 2.2 specifies the Hamiltonian for a double well system, section 2.3 specifies the Hamiltonian for triple and quadruple well system, section 2.4 details the single plaquette Hamiltonian and section 2.5 explains the double (multi) plaquette Hamiltonian.

In this thesis we use two different interaction potentials $V(r_i, r_j)$. For the calculations in sections chapter 4 and chapter 5 we use a delta function contact interaction. Since those calculations are quasi one-dimensional[1], we do not need to regularize the delta function [49, 125, 126]

[1]The code that was used in this thesis is inherently two-dimensional (it implements the Hamiltonian in equation (2.2)). Whenever we speak of quasi-one dimensional calculations in this thesis, we mean calculations for which only one basis function along the strongly confined direction was used. The resulting wavefunctions are products in x and y with only a single common orbital along y. The calculations therefore become effectively one-dimensional. This is justified as long as the energy scale in the strongly confined direction is much larger than the other energy scales in the problem (i.e. achieved by setting $\hbar\omega_y = 100\hbar\omega_x$).

$$V(\boldsymbol{r_i}, \boldsymbol{r_j}) = g_{xy}\delta(\boldsymbol{r_i} - \boldsymbol{r_j}) \tag{2.3}$$

---

where:

g_{xy}:	specifies the interaction strength
δ:	is the Dirac Delta function
$\boldsymbol{r_i}, \boldsymbol{r_j}$:	position of particle i, j

For truly 2 dimensional calculations however (i.e. when studying plaquette systems) we would have to regularize the delta function. In order to avoid numerical intricacies we instead use a short range Gaussian potential with width σ in chapters 6 to 8. The Gaussian is chosen such that it yields a delta function in the $\sigma \to 0$ limit. Such a potential is a good approximation to a delta function for a sufficiently small Gaussian width σ as described in [127] and used in several places throughout literature [128–131].

$$V(\boldsymbol{r_i}, \boldsymbol{r_j}) = \frac{g_{xy}}{\sigma^2\pi} e^{(\boldsymbol{r_i}-\boldsymbol{r_j})^2/\sigma^2} \tag{2.4}$$

---

where:

g_{xy}:	specifies the interaction strength
σ:	is the width of the Gaussian
$\boldsymbol{r_i}, \boldsymbol{r_j}$:	position of particle i, j

2.2 Microscopic double well Hamiltonian

The Hamiltonian for the double well potential used in this thesis was first introduced in [132] and is given as

$$H(i) = \frac{p_{yi}^2}{2m} + \quad V_{ho}(y_i) \quad + \frac{p_{xi}^2}{2m} + V_{dw}(x_i) \tag{2.5}$$

$$H(i) = \frac{p_{yi}^2}{2m} + \underbrace{\frac{1}{2}m\omega_y y_i^2}_{\text{harmonic oscillator in y}} + \frac{p_{xi}^2}{2m} + \underbrace{\frac{1}{2}m\omega_{xk}x_{ik}'^2 + V_{neck}(x_i) + h_k}_{\text{double well in x}} \tag{2.6}$$

---

where:

x'_{ik}:	$x'_{ik} = x_i - x_k$ with x_k fixed (the x_k represent the positions of the potential minima)
k:	$k = 1$ for $x < 0$ (left) and $k = 2$ for $x > 0$ (right)
V_{neck}:	$V_{neck}(x_i)$ smoothly connects the wells centered around x_k
h_k:	h_k controls the relative well depth
w_y, w_{xk}:	the frequencies of the confinig potential
m:	is the mass of the atoms

and we define the tilt Δ between the wells as $\Delta = h_{k=2} - h_{k=1}$. The smooth neck, previously used in i.e. [121, 132–134], is defined as

$$V_{neck}(x) = \frac{1}{2}mw_{xk}^2 \left[C_k x_k'^3 + D_k x_k'^4\right] \theta(|x| - |x_k|) \tag{2.7}$$

---

where:

θ:	θ is the Heaviside function
x'_{ik}:	$x'_{ik} = x_i - x_k$ with x_k fixed (the x_k represent the positions of the potential minima)
k:	$k = 1$ for $x < 0$ (left) and $k = 2$ for $x > 0$ (right)
C_k:	$C_k = (2 - 4\epsilon_k^b)/x_k$
D_k:	$D_k = (1 - 3\epsilon_k^b)/x_k^2$
ϵ_k^b:	$\epsilon_k^b = (V_b - h_k)/V_{0k}$
V_{0k}:	$V_{0k} = mw_{xk}^2 x_k^2/2$
x_k:	represents the position of the potential minima
h_k:	h_k controls the relative well depth
w_{xk}:	the frequencies of the confining potential along x

Unless otherwise noted in this thesis $x_{k=1}$ and $x_{k=2}$ are combined into one parameter $d = x_{k=2} - x_{k=1}$ with $x_{k=1} = -x_{k=2}$. Furthermore we use equal frequencies in the left and

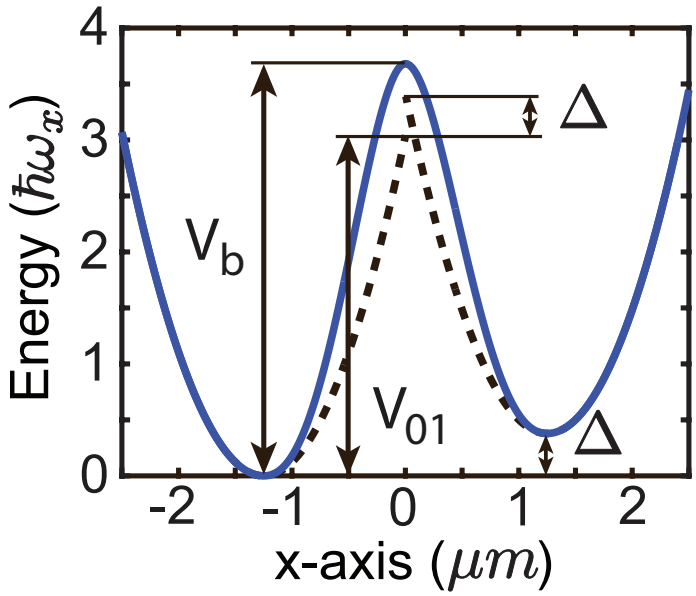

Figure 2.1: Plot of a double well potential in which the parameters Δ, V_{01} and V_b are illustrated. V_{01} denotes the intersection of the left parabola (dashed line, without a smooth neck) with the vertical axis at $x = 0$. The dashed curve is in general not continuous at $x = 0$. This is corrected with the smooth neck. The minima of the potential wells are at $x_{k=1}$ and $x_{k=2} = -x_{k=1}$, the maximum of the interwell barrier is at $x = 0$. In this plot $\hbar\omega_x = 6.6\,\mathrm{kHz}, V_b = 24.30\,\mathrm{kHz}, d = 2.5\,\mu\mathrm{m}, \Delta = 2.51\,\mathrm{kHz}$.

right well $w_{xk=1} = w_{xk=2}$. We also set $h_{k=1} = 0 \Rightarrow \Delta = h_{k=2}$ with no loss of generality ($h_{k=1} \neq 0$ represents a global energy shift.).

final parameters

Therefore the parameters used to control the double well potential in this thesis are

w_x, V_b, Δ, d

This potential is very flexible and allows us to obtain results for a single well ($d = 0,\ \ V_b = 0$), a fully separated double well ($d \neq 0,\ \ V_b \gg \min(\hbar w_{xk}, \hbar w_y)$), a tilted double well $\Delta > 0$ and all possible configurations in between. It also forms the building block for the single (see section 2.4) and multi (see section 2.5) plaquette Hamiltonian.

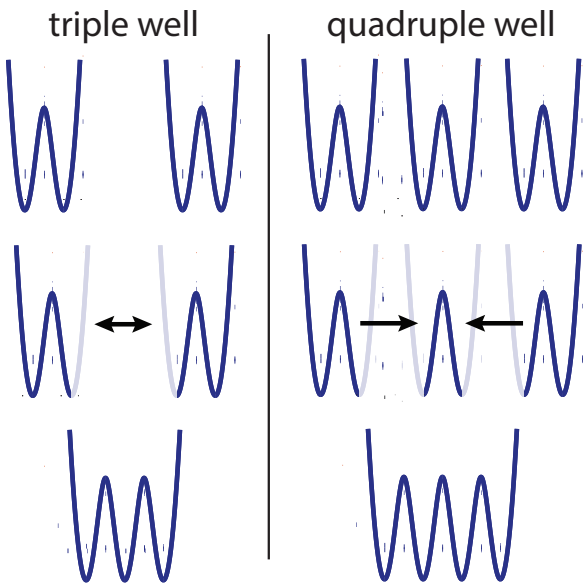

Figure 2.2: Schematic of how to assemble a triple (quadruple) well potential. Starting from separate double well potentials (where each double well potential has the functional form $V_{dw}(x)$, see equations (2.5) and (2.6)) the inward facing potential walls are removed and the resulting pieces connected. This creates a triple (quadruple) well potential with smooth necks. Since we used double well potentials as building blocks we have full control over the individual barriers, the distance between the minima and the tilts between the minima.

2.3 The microscopic triple and quadruple well Hamiltonian

We can use our double well potential as a building block to build systems with more wells. To create a triple well potential V_{tw} we start with two displaced double well potentials and remove the inward facing potential wells by multiplying the function for the double well potential with a heaviside theta function ($\theta(x)$):

$$V_{tw}(x) = V_{dw}(x - d/2)\theta(x) + V_{dw}(x + d/2)\theta(-x) \tag{2.8}$$

Figure 2.2 illustrates how to build a triple well potential. To create a quadruple well potential we start out with three double well potentials and use Heaviside theta functions to cut the inward facing potential walls to the right and/or left of the minima. We then combine the resulting potentials. This procedure is illustrated in figure 2.2.

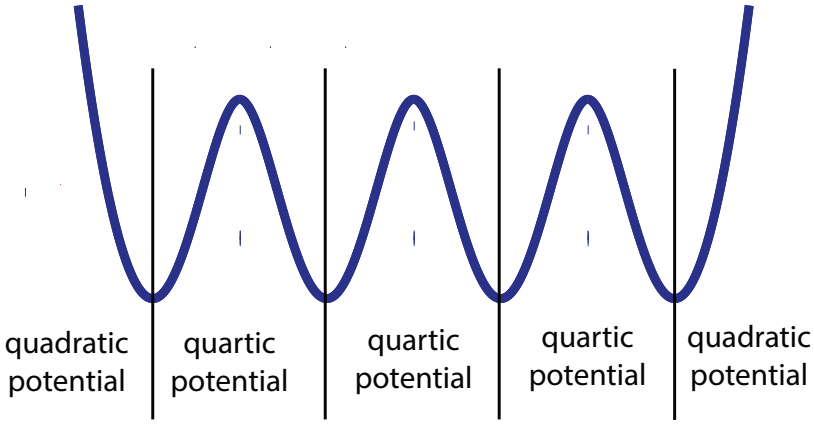

Figure 2.3: Schematic of a quadruple well potential with quadratic and quartic sections annotated.

2.3.1 Harmonic edge potential

The procedure described in section 2.3 to create a triple or quadruple well microscopic Hamiltonian results in subtle differences between the individual sites. Looking at the fully assembled quadruple well (see figure 2.3) it is apparent that the leftmost and rightmost wells are slightly different from the middle wells. The lefmost and rightmost wells end in a harmonic potential on the outside ($c_{ho}x^2$) and a quartic potential on the inside ($c_{qi}x^4 + c_{hi}x^2$). The quartic potential arises from the presence of the smooth connecting neck (see section 2.2 for full details of these terms). In contrast the two inner wells are bordered by quartic potentials on all sides.

This difference in potential shape between the wells can slightly lift degeneracies in the energy levels, even when the quartic potentials are chosen such that they locally (around the potential minima) approximate the outer harmonic potentials very well. The ordering of almost degenerate energy levels can therefore sometimes be perturbed. Whether this has any impact on the measurements depends on the exact configuration of the system and what states are being studied.

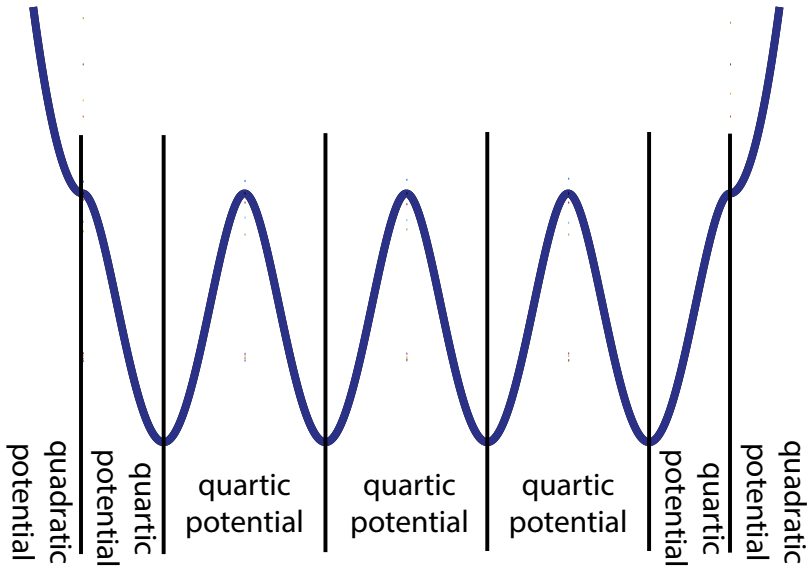

Figure 2.4: Schematic of a quadruple well potential with mirrored edges with quadratic and quartic sections annotated. Compare to figure 2.3.

2.3.2 "Mirrored middle barrier" edge potential

To mitigate the effects of the harmonic edge potentials (see section 2.3.1) one can "mirror" the middle barriers for the outside potential and smoothly connect them to a harmonic potential at their maxima. The resulting potential shape is illustrated in figure 2.4. With this procedure the potentials look the same for every well (up to the barrier height V_b).

2.4 The microscopic single plaquette Hamiltonian

For our single plaquette calculations we use the double well external potential from section 2.2 in both x and y direction.

$$V(x_i, y_i) = V_{dw}(x_i) + V_{dw}(y_i). \tag{2.9}$$

This results in a confining potential that has four minima (on the edges of a rectangle) and smooth connecting necks between them. We have full control over the distances between

the minima in x and y and we have full control over the barriers and tilts between them. This allows for calculations with varying degrees of coupling between the sites and allows us to run calculations for a fully four-fold symmetric plaquette as well as for configurations with a lower symmetry.

2.5 The microscopic double (multi) plaquette Hamiltonian

For our double plaquette calculations we use a repetition of the single plaquette external potential from section 2.4. We keep the potential along y as is, but use a quadruple well potential along x.

To form even larger systems we can use 1D confining potentials with even more wells for both the x and y direction, allowing for the formation of multi plaquette systems. The limiting factor eventually becomes the memory required for the calculation given the increasing number of particles and single-particle basis functions.

2.6 Methods for solving the microscopic Hamiltonian

Our microscopic Hamiltonian (see section section 2.1) consists of a single particle part and a two particle part. The single particle part contains the terms for the external confining potential and the kinetic energy and the two particle part contains the terms for the interaction between the particles. In the following we discuss how to best solve this Hamiltonian.

2.6.1 Methods for solving the Hamiltonian - full CI

Solving the two particle part of the Hamiltonian is significantly more complex than the single particle part, since the proper fermionic symmetries of the many body system need to be respected. Furthermore the Hilbert space and therefore the computational cost scales exponentially with the number of particles. Due to the resulting complexity of the many-body problem a large part of the literature focuses on approximate methods (i.e. DFT, Monte Carlo), or spin models to analyze a many body system. Such an approach has the

disadvantage that the assumptions underlying the approximate methods have to be carefully checked which is potentially difficult depending on the experimental realizations of the system. Furthermore using such models restricts one's analysis to only a subset of all possible experimental configurations. For this thesis we therefore decided to use microscopic full configuration interaction (full CI) to calculate the solutions of our Hamiltonian. Full CI is capable of providing an exact solution for the microscopic Hamiltonian given sufficient computational resources.

In full CI the many body wavefunction $\Phi^{CI}_{Nq}(\boldsymbol{r_1}, \boldsymbol{r_2}, \ldots, \boldsymbol{r_N})$ is expressed as a superposition of Slater determinants $\Psi^N_I(\boldsymbol{r_1}, \boldsymbol{r_2}, \ldots, \boldsymbol{r_N})$ which span the many body Hilbert space. The Slater determinants are build from spin orbitals $\chi_j(\boldsymbol{r})$. Namely

$$\Phi^{CI}_{Nq}(\boldsymbol{r_1}, \boldsymbol{r_2}, \ldots, \boldsymbol{r_N}) = \sum_I C^q_I \Psi^N_I(\boldsymbol{r_1}, \boldsymbol{r_2}, \ldots, \boldsymbol{r_N}) \tag{2.10}$$

$$\Psi^N_I(\boldsymbol{r_1}, \boldsymbol{r_2}, \ldots, \boldsymbol{r_N}) = \frac{1}{\sqrt{N!}} \begin{vmatrix} \chi_{j_1}(\boldsymbol{r_1}) & \cdots & \chi_{j_N}(\boldsymbol{r_1}) \\ \vdots & \ddots & \vdots \\ \chi_{j_1}(\boldsymbol{r_N}) & \cdots & \chi_{j_N}(\boldsymbol{r_N}) \end{vmatrix} \tag{2.11}$$

$$\chi_{j_1}(\boldsymbol{r_1}) = \begin{cases} \psi_j(x,y)\alpha, & \text{if } 1 \leq j \leq K \\ \psi_{j-K}(x,y)\beta, & \text{if } K < j \leq 2K \end{cases} \tag{2.12}$$

---

where:

- C^q_I: a complex coefficient determined through the diagonalization of the Hamiltonian
- q: index representing the state (ground state, 1st excited, ...)
- I: master index representing the number of arrangements $\{j_1, j_2, \ldots, j_N\}$ under the restriction that $1 \leq j_1 \leq j_2 \leq \ldots \leq j_N \leq 2K$ (without loss of generality since determinants are equivalent up to a sign under permutation)
- j_{1-N}: index representing the particles
- α, β: denote up and down spins (we are considering a spin $1/2$ system)
- N : is the number of particles
- K : is the number of single particle basis functions (spbf)

Writing the CI wavefunction as in equation (2.10) transforms the Hamiltonian into a matrix diagonalization problem. The result of this diagonalization yields the coefficients C_I^q and the eigenergies $\mathcal{E}_q$. The matrix elements between the basis determinants $\left\langle \Psi_{I1}^N \middle| H \middle| \Psi_{I2}^N \right\rangle$ are calculated using Slater rules. The basic idea is that a matrix element for a N-body operator will only be non-zero if no more than N basis functions in the determinant are different. Additional time saving relationships can be derived using the symmetry of the determinants. An excellent description of the Slater rules can be found in Szabo "Modern quantum chemistry" [119] section 2.3.3 (p. 68). Furthermore we want to note that the Slater determinants conserve the third spin projection $\boldsymbol{S_z}$ but not the total spin $\boldsymbol{S^2}$. However all the Hamiltonians ($\boldsymbol{H}$) considered in this thesis are spin independent. Therefore $\boldsymbol{H}$ and $\boldsymbol{S^2}$ commute, and consequently the solutions of the CI, in the absence of degeneracies, are also eigenstates of $\boldsymbol{S^2}$. Further details on the full CI methodology employed by us can be found in i.e.: [133] (supplemental material) [135] [119].

On the importance of microscopic full CI calculations

Full CI calculations are a pivotal benchmark for the comparison with experimental results or other theoretical predictions obtained by different methods. Since full CI uses the microscopic Hamiltonian no fundamental assumptions need to be made (as is for instance the case in the Hubbard model or in mean-field models). Microscopic full CI calculations are therefore the most accurate numerical tool available to study physical systems.

2.6.2 Methods for solving the single particle part of the Hamiltonian

For quick convergence of the full CI calculations it is often beneficial to use a basis set that already diagonalizes the single particle part of the Hamiltonian. Many of the single particle parts of the Hamiltonians used in this thesis are separable in x and y and we can therefore solve two one-dimensional Hamiltonians (the only Hamiltonians that are not sep-

arable are the ones involving a magnetic field). A software package that can solve one dimensional Hamiltonians with high performance and high accuracy is Chebfun [136]. It uses Chebychev polynomials as an efficient and highly accurate approximation of the true wave function. From the documentation:

> The implementation of Chebfun is based on the mathematical fact that smooth functions can be represented very efficiently by polynomial interpolation in Chebyshev points, or equivalently, thanks to the Fast Fourier Transform, by expansions in Chebyshev polynomials [...] Chebfun makes use of adaptive procedures that aim to find the right number of points automatically so as to represent each function to roughly machine precision, that is, about 15 digits of relative accuracy.

We have confirmed the accuracy of the chebfun solutions with both symbolic and numeric calculations in Mathematica and the agreement was excellent which chebfun being significantly faster.

2.7 SPD, SR-CPD, $\mathrm{N}-1$ SR-CPD, SPOL, natural orbitals, von Neumann entropy and correlation functions

This section provides an overview over the methodologies that we use to analyze our wavefunctions.

First we are going to describe the *single particle density* (SPD, see section 2.7.1), which provides a visualization of the particle density distribution of the wavefunction. Thereafter we are explaining the *spin resolved conditional probability density* (SR-CPD, see section 2.7.2), which provides a visualization of the correlations that are present in the many body wavefunction. This is achieved by fixing the position of one particle with a defined spin at one position and looking at the density distribution of the remaining particles (which also have a specified spin). I.e. the position of a spin-down atom is fixed at the

origin and the spatial density distribution of all the spin-up atoms is calculated. Afterwards we are describing the *spin resolved* $N-1$ *body conditional probability density* ($N-1$ SR-CPD, see section 2.7.3). It is similar to the SR-CPD, but instead of fixing one particle, one fixes $N-1$ particles and their spins and looks for the density distribution of the remaining particle. In section 2.7.5 we give a short introduction into the theory of natural orbitals. In a nutshell natural orbitals are the single particle basis functions that achieve the most rapid convergence when representing the true many body wavefunction as a superposition of slater determinants. In the second to last section of this chapter (section 2.8) we describe n-th order density matrices and correlation functions. They are the subject of considerable interest as first experimental measurements of position and momentum space correlation functions in optical traps have recently been achieved [137, 138]. In the last section of this chapter (section 2.8.4) we summarize some important properties of density matrices and their connection to the von Neumann entropy.

2.7.1 Single particle density (SPD)

The single particle density (SPD), in the following denoted by $\rho(\boldsymbol{r})$, is given as

$$\rho(\boldsymbol{r}) = \left\langle \Phi_{Nq}^{CI} \middle| \sum_{i=1}^{N} \delta(\boldsymbol{r} - \boldsymbol{r_i}) \middle| \Phi_{Nq}^{CI} \right\rangle \tag{2.13}$$

---

where:

Φ_{Nq}^{CI}: the wave function obtained through our CI calculation (see section 2.6.1)

$\boldsymbol{r_i}$: position of particle i, with $\boldsymbol{r_i} = (x_i, y_i)$

Note that using this definition the SPD is normalized to the number of particles. The SR-SPD is the spin resolved (SR) version of the SPD. It yields the spatial density distribution of all the particles with a defined spin and is given by:

$$\rho(\boldsymbol{r},\sigma) = \left\langle \Phi_{qN}^{CI} \middle| \sum_{i=1}^{N} \delta(\boldsymbol{r}-\boldsymbol{r_i})\delta_{\sigma\sigma_i} \middle| \Phi_{qN}^{CI} \right\rangle \tag{2.14}$$

---

where:

Φ_{Nq}^{CI}: the wave function obtained through our CI calculation (see section 2.6.1)

$\boldsymbol{r_i}$: position of particle i, with $\boldsymbol{r_i} = (x_i, y_i)$

σ_i: spin of particle i

The SPD yields a representation of the spatial distribution of the wavefunction, it is the sum of the spatial probability amplitudes of all the particles. The SR-SPD is the spin resolved version of the SPD (i.e. for a spin 1/2 system the SPD associated with the spin up or down particles).

2.7.2 Spin resolved conditional probability density (SR-CPD)

The spin resolved conditional probability density (SR-CPD) in the following denoted $P_{\sigma\sigma_0}(\boldsymbol{r},\boldsymbol{r_0})$ is defined as

$$P_{\sigma\sigma_0}(\boldsymbol{r},\boldsymbol{r_0}) = P_{\sigma\sigma_0}^{cf}(\boldsymbol{r},\boldsymbol{r_0}) / \int P_{\sigma\sigma_0}^{cf}(\boldsymbol{r},\boldsymbol{r_0})\, d\boldsymbol{r} \tag{2.15}$$

$$P_{\sigma\sigma_0}^{cf}(\boldsymbol{r},\boldsymbol{r_0}) = \left\langle \Phi_{Nq}^{CI} \middle| \sum_{i\neq j} \delta(\boldsymbol{r}-\boldsymbol{r_i})\delta(\boldsymbol{r_0}-\boldsymbol{r_j})\delta_{\sigma\sigma_i}\delta_{\sigma_0\sigma_j} \middle| \Phi_{Nq}^{CI} \right\rangle, \tag{2.16}$$

---

where:

σ_0: denotes the spin of the fixed particle

$\boldsymbol{r_0}$: is the space coordinate of the fixed particle

σ_i, σ_j: is the spin of particle i, j

Φ_{Nq}^{CI}: is the CI wavefunction (see section 2.6.1)

$\boldsymbol{r_i}, \boldsymbol{r_j}$: position of particle i, j

The function $P_{\sigma\sigma_0}^{cf}$ is also known in literature as the spin resolved two-point anisotropic

correlation function. For more details see [139][140][141][142]. Also note that while the SPD is unique for a given many-body wavefunction the SR-CPDs depend on the spatial coordinates of the fixed particle and the spin configuration.

The SR-CPD gives the probability for finding an atom in position r with spin projection σ, under the condition that an atom with spin projection σ_0 is localized at position r_0.

2.7.3 $\mathbf{N-1}$ body spin resolved conditional probability density ($\mathbf{N-1}$ SR-CPD)

To obtain the $N-1$ body spin resolved conditional probability density ($N-1$ SR-CPD) we fix $N-1$ particles and their spins and calculate the single particle density for the remaining particle. As an operator the $N-1$ body SR-CPD can be written as:

$$O_{N-1\ SR-CPD} = \prod_{i=0}^{N-1} \delta(\boldsymbol{r_i} - \boldsymbol{r_{i0}})\delta_{\sigma_i\sigma_{i0}} \tag{2.17}$$

---

where:

δ:	is the dirac delta function
$\boldsymbol{r_i}$:	is the position of particle i
$\boldsymbol{r_{i0}}$:	is the fixed position of particle i
σ_i:	is the spin of particle i
σ_{i0}:	is the fixed spin of particle i

This is an $N-1$ body operator and therefore can't be evaluated using the Slater rules described in [119] (except of course for the special case of $N \leq 3$). Instead we expand the determinants in our full CI wavefunction and select the components whose spin primitives match the fixed spins σ_{i0}. Furthermore we fix the coordinates of $N-1$ particles in the wavefunction according to the fixed positions r_i. As a result the wavefunction only has one space degree of freedom left, for which we plot the density. This density is the $N-1$ body SR-CPD. Of course for a given many-body wavefunction there are many $N-1$ body

SR-CPDs that can be plotted (by varying the spatial coordinates of the fixed particles and the spin configuration).

The $N-1$ body SR-CPD gives the probability distribution of the remaining particle after fixing $N-1$ particles and their spins at specified positions.

2.7.4 Spin polarization densities (SPOL)

The SPD $\rho(\boldsymbol{r})$ is defined as the sum of the spatial probability amplitudes of all the particles (irrespective of their spin). It can be written as the sum of the spin resolved SPDs $\rho(\boldsymbol{r}) = \rho(\boldsymbol{r},\uparrow) + \rho(\boldsymbol{r},\downarrow)$. However in some cases it can be useful to look at the difference of the spin resolved SPDs, which we call the spin polarization density (SPOL). It is defined as

$$\rho_{\text{pol}}(\boldsymbol{r}) = \rho(\boldsymbol{r},\uparrow) - \rho(\boldsymbol{r},\downarrow) = \left\langle \Phi_{Nq}^{CI} \middle| \sum_{i=1}^{N} \delta(\boldsymbol{r}-\boldsymbol{r_i})(\delta_{\uparrow\sigma_i} - \delta_{\downarrow\sigma_i}) \middle| \Phi_{Nq}^{CI} \right\rangle \tag{2.18}$$

The SPOL is able to visualize imbalances in the spin-component of the wavefunction, whereas the SPD is able to visualize the particle position space distribution. We can therefore think of them as complementary tools, that we can employ depending on which quantity we want to study.

The SPOL visualizes the spin imbalance (the difference between the up and down spin SPD) in a wavefunction.

2.7.5 Natural orbitals

The natural orbitals were introduced by Löwdin [143, 144] and represent a single particle basis set that is optimally adapted to the many body problem. A superposition of slater determinants built from natural orbitals exhibits the most rapid convergence to the true many

body wave function. The natural orbitals are defined as the set of orbitals that diagonalize the single particle density matrix (SPDM). The eigenvalues of the SPDM are known in literature as the occupation numbers [143]. The natural orbitals also offer a tremendous simplification when calculating the von Neuman entropy (see section 2.7.6). Once the SPDM has been diagonalized the calculation of the von Neumann entropy is simply a trace over a product of diagonal matrices. For a detailed description of Natural Orbitals and example plots for a double well system see [133].

The basis formed by the natural orbitals is the basis for which the expansion of the many body wavefunction in determinants gives the most rapid convergence. In the case of a finite expansion, the number M is called the Slater rank of the many body wave function.

2.7.6 Von Neumann entanglement entropy

In our studies we use the Von Neumann entropy [145] as a measure of entanglement. It is defined as

$$S_{vN} = \mathrm{Tr}(\rho \log_2(\rho)) + C \tag{2.19}$$

$$C = -\log_2(N) \tag{2.20}$$

---

where:

ρ : is the single-particle density matrix

N : is the number of particles

The constant C has been chosen such that $S_{vN} = 0$ for an uncorrelated state (a state which can be described by a single determinant). The results of our full CI calculation are a superposition of determintants, for which a convenient formula to calculate the single-particle density matrix exists, see e.q. 56 in [143]. In a system with two particles which we

are studying in chapter 4 the natural orbitals have some interesting additional properties. I.e. for a two-particle singlet it is known that [144]

$$\Phi^{CI}(\boldsymbol{r},\boldsymbol{r'}) = \frac{1}{\sqrt{2}}(\alpha\beta' - \beta\alpha')\sum_{j=1}^{M} d_j \phi_j^{NO}(\boldsymbol{r})\phi_j^{NO}(\boldsymbol{r'}) \tag{2.21}$$

$$d_j = \pm(p_j)^{1/2} \tag{2.22}$$

---

where:

M:	is the total number of natural orbitals
ϕ_j^{NO}:	is the j-th natural orbital
α, β :	up and down spin for the particle with coordinate $\boldsymbol{r}$
α', β' :	up and down spin for the particle with coordinate $\boldsymbol{r'}$
d_j:	is the coefficient of the j-th natural orbital
p_j:	is the occupation number of the j-th natural orbital. The sign in front of the $p_j^{1/2}$ can be uniquely determined, see [143].

and a similar expression applies for the triplet [144].

2.8 Density matrices and correlation functions in position and momentum space and noise maps

In order to analyze the many-body wavefunction it can be insightful to look at density matrices and correlation functions. The SR-CPD introduced in section 2.7.2 is one way of visualizing a second-order correlation function. Here we present a more general definition of correlation functions (and their underlying density matrices), which will be particularly useful for our analysis of second-order correlation functions in quasi one dimensional traps (see chapter 7 and chapter 8).

2.8.1 Real space density matrices and correlation functions

Since the p-th order correlation function is the diagonal element of the p-th order density matrix we first introduce density matrices. Given an N-body wavefunction $\Phi(\mathbf{x}_1, \mathbf{x}_2, \mathbf{x}_3, ..., \mathbf{x}_N)$

the p-th order density matrix D_p in position space is defined as [143]

$$D_p(\mathbf{x}_1, \mathbf{x}'_1, \mathbf{x}_2, \mathbf{x}'_2, \ldots, \mathbf{x}_p, \mathbf{x}'_p) = \int_{-\infty}^{\infty} \Phi^\dagger(\mathbf{x}'_1, \mathbf{x}'_2, \ldots, \mathbf{x}'_p, \ldots, \mathbf{x}_N)\Phi(\mathbf{x}_1, \mathbf{x}_2, \ldots, \mathbf{x}_p, \ldots, \mathbf{x}_N)d\mathbf{x}_{p+1} \ldots d\mathbf{x}_N, \quad (2.23)$$

where $\mathbf{x}_i$ represents the space x_i and spin coordinate σ_i of particle i. There are three commonly used choices for the normalization of density matrices. Here we are normalizing all correlation functions to 1, however some authors [146] prefer to multiply the integral in Equation 2.23 with $N!/(N-p)!$ and the normalization found in Löwdin's original papers [143] multiplies Equation 2.23 by $N!/((N-p)!p!)$.

Since the first and second-order density matrices are frequently used in chapter 7 and chapter 8, we introduce the following special notation:

$$\mathcal{P}(\mathbf{x}_1, \mathbf{x}'_1, \mathbf{x}_2, \mathbf{x}'_2) \equiv D_2(\mathbf{x}_1, \mathbf{x}'_1, \mathbf{x}_2, \mathbf{x}'_2) \quad (2.24)$$

$$\rho(\mathbf{x}_1, \mathbf{x}'_1) \equiv D_1(\mathbf{x}_1, \mathbf{x}'_1) \quad (2.25)$$

This is consistent with the notation in our papers [123, 147]. Also note that the first order density matrix, can be obtained from the second-order density matrix:

$$\rho(\mathbf{x}_1, \mathbf{x}'_1) = \int_{-\infty}^{\infty} \Phi^\dagger(\mathbf{x}'_1, \mathbf{x}_2, \mathbf{x}_3, \ldots, \mathbf{x}_N)\Phi(\mathbf{x}_1, \mathbf{x}_2, \mathbf{x}_3, \ldots, \mathbf{x}_N)d\mathbf{x}_2 \ldots d\mathbf{x}_N \quad (2.26)$$

$$= \int_{-\infty}^{\infty} \mathcal{P}(\mathbf{x}_1, \mathbf{x}'_1, \mathbf{x}_2, \mathbf{x}_2)d\mathbf{x}_2. \quad (2.27)$$

The p-th order correlation function is the diagonal element of the p-th order density matrix. In this thesis we distinguish the p-th order correlation function from the p-th order density matrix by the absence of the primed coordinates:

$$D_p(\mathbf{x}_1, \mathbf{x}_2, \ldots, \mathbf{x}_p) \equiv D_p(\mathbf{x}_1, \mathbf{x}_1, \mathbf{x}_2, \mathbf{x}_2, \ldots, \mathbf{x}_p, \mathbf{x}_p), \quad (2.28)$$

We are particularly interested in the first and second-order correlation functions since they have recently been experimentally observed [137, 138]. We introduce the following special notation

$$\mathcal{P}(\mathbf{x}_1, \mathbf{x}_2) \equiv \mathcal{P}(\mathbf{x}_1, \mathbf{x}_1, \mathbf{x}_2, \mathbf{x}_2), \tag{2.29}$$

$$\rho(\mathbf{x}_1) \equiv \rho(\mathbf{x}_1, \mathbf{x}_1), \tag{2.30}$$

where we distinguish the correlation functions from the density matrices by the absence of the primed coordinates. It is worth noting that the first and second-order correlation functions are in literature sometimes referred to as one and two-point correlation functions.

2.8.2 Momentum space density matrices and correlation functions

Density matrices and correlation functions can be written in position and momentum space and can be converted from position to momentum space and vice versa via Fourier transforms. I.e. the first and second-order momentum density matrices can be obtained via:

$$\mathcal{G}(\mathbf{k}_1, \mathbf{k}_1', \mathbf{k}_2, \mathbf{k}_2') = \frac{1}{4\pi^2} \int_{-\infty}^{\infty} e^{-i\mathbf{k}_1\mathbf{x}_1} \int_{-\infty}^{\infty} e^{i\mathbf{k}_1'\mathbf{x}_1'} \int_{-\infty}^{\infty} e^{-i\mathbf{k}_2\mathbf{x}_2} \int_{-\infty}^{\infty} e^{i\mathbf{k}_2'\mathbf{x}_2'} \mathcal{P}(\mathbf{x}_1, \mathbf{x}_1', \mathbf{x}_2, \mathbf{x}_2') d\mathbf{x}_1 d\mathbf{x}_1' d\mathbf{x}_2 d\mathbf{x}_2', \tag{2.31}$$

$$\tau(\mathbf{k}_1, \mathbf{k}_1') = \frac{1}{4\pi^2} \int_{-\infty}^{\infty} e^{-i\mathbf{k}_1\mathbf{x}_1} \int_{-\infty}^{\infty} e^{i\mathbf{k}_1'\mathbf{x}_1'} \rho(\mathbf{x}_1, \mathbf{x}_1') d\mathbf{x}_1 d\mathbf{x}_1', \tag{2.32}$$

where $\mathbf{k}_i$ represents the momentum k_i and spin coordinate σ_i of particle i. Again the first and second-order momentum correlation functions are easily obtained as the diagonal elements of the respective density matrices:

$$\mathcal{G}(\mathbf{k}_1, \mathbf{k}_2) \equiv \mathcal{G}(\mathbf{k}_1, \mathbf{k}_1, \mathbf{k}_2, \mathbf{k}_2), \tag{2.33}$$

$$\tau(\mathbf{k}_1) \equiv \tau(\mathbf{k}_1, \mathbf{k}_1). \tag{2.34}$$

The momentum correlation functions are especially important for experiments that perform time of flight measurements after releasing the atoms from the trap, since such measurements can be directly related to the momentum correlation functions.

2.8.3 Noise maps

Another quantity that is sometimes discussed in conjunction with the correlation functions is the noise distribution. Once one has obtained the first and second-order correlation functions the calculations of noise distributions in position and momentum space is straightforward:

$$\mathcal{N}_{\mathcal{P}}(\mathbf{x}_1, \mathbf{x}_2) = \mathcal{P}(\mathbf{x}_1, \mathbf{x}_2) - \rho(\mathbf{x}_1)\rho(\mathbf{x}_2), \tag{2.35}$$

$$\mathcal{N}_{\mathcal{G}}(\mathbf{k}_1, \mathbf{k}_2) = \mathcal{G}(\mathbf{k}_1, \mathbf{k}_2) - \tau(\mathbf{k}_1)\tau(\mathbf{k}_2). \tag{2.36}$$

2.8.4 A short summary of the properties of density matrices and their connection with the von Neumann entropy

Density matrices have a wide range of interesting applications. This section aims to highlight some of their most important properties and to show their connection with the von Neumann entropy.

Properties

All density matrices ρ satisfy $Tr(\rho) = 1$ as well as $\rho^\dagger = \rho$ and additionally for pure states $Tr(\rho^2) = 1$ while for mixed states $Tr(\rho^2) < 1$ [148]. For all the two particle Hamiltonians in this thesis, the second-order density matrix ρ^{2nd} satisfies the idempotency property:

$$\rho^{2nd} \cdot \rho^{2nd} = \rho^{2nd}. \tag{2.37}$$

It follows immediately from equation (2.37) that in the two particle case

$$Tr\left(\rho^{2nd} \cdot \rho^{2nd}\right) = Tr\left(\rho^{2nd}\right) = 1. \tag{2.38}$$

Note that this is true in general for the N-th order density matrix of a N particle system that doesn't involve statistical mixtures of states.

Entanglement

If one wanted to study the entanglement of the system one would perform i.e. a partial trace and calculate the von Neumann entropy

$$\rho^{1st} = \mathrm{Tr}_2(\rho^{2nd}) \tag{2.39}$$

$$S_{vN} = -\mathrm{Tr}(\rho^{1st} \ln\left(\rho^{1st}\right)) \tag{2.40}$$

where Tr_2 denotes the partial trace over particle 2.

CHAPTER 3

SPIN MODELS

In this thesis we frequently employ comparisons with spin models to foster a more detailed understanding of our CI results. Especially for strongly interacting systems where particles are repulsively localized and for systems at half filling (i.e. the same number of sites and atoms) spin models can often be successful at describing the essential physics. Furthermore spin models are frequently employed by experimentalists to provide guidance for experimental observations. In the following sections we give a brief introduction to the different spin models used in this thesis.

Although the spin models in this chapter can be written for particles with any spin, in this thesis we are restricting ourselves to spin 1/2 fermions, since they are most relevant to current experimental efforts.

3.1 Hubbard Hamiltonian

The Hubbard Hamiltonian was introduced in a serious of foundational papers by John Hubbard starting in 1963 [149–155]. The Hubbard Hamiltonian in second quantization is given as [155–159]:

$$H = -t \sum_{<i,j>,\sigma} \left(\hat{c}^{\dagger}_{i,\sigma} \hat{c}_{j,\sigma} + \hat{c}^{\dagger}_{j,\sigma} \hat{c}_{i,\sigma} \right) + U \sum_{i=1}^{N} \hat{n}_{i\uparrow} \hat{n}_{i\downarrow}, \tag{3.1}$$

---

where:

$< i, j >$:	represents the sum over neighrest neighbors
σ:	represents the up ($\uparrow$) and down ($\downarrow$) spin
$\hat{c}^{\dagger}_{i,\sigma}$ $(\hat{c}_{i,\sigma})$:	creation (anhilation) operator for a particle with spin σ at site i
$\hat{n}_{i\sigma}$:	the number operator defined as $\hat{n}_{i\sigma} = \hat{c}^{\dagger}_{i,\sigma} \hat{c}_{i,\sigma}$
N:	denotes the total number of lattice sites
U :	the on-site interaction parameter
t :	the neighrest neighbor tunneling parameter

Despite over 50 years of intense research, general solutions of the Hubbard Hamiltonian have not yet been found and its surprising versatility makes it one of the most well known and well analyzed Hamiltonians in condensed matter physics. It has numerous applications most notably in the study of magnetism and high T_c superconductivity [160–163]. Even though the Hubbard Hamiltonian is an approximate model itself, due to its complexity, other approximative methods like mean field and monte carlo treatments have been a prominent avenue through which it has been explored [159]. However for small systems the Hubbard Hamiltonian can be exactly diagonalized which is the approach we are taking in this thesis.

3.1.1 Analytical and numerical solutions of the Hubbard Hamiltonian

To obtain analytic solutions to the Hubbard model we use the software package SNEG [164], which is a "Mathematica package for symbolic calculations with second-quantization-operator expressions". From the documentation:

> SNEG library is a Mathematica package that provides a framework for performing calculations using the operators of the second quantization with an emphasis on the anti-commuting fermionic operators in the context of solid-state and atomic physics. It consists of a collection of transformation rules that define the algebra of operators and a comprehensive library of utility functions.

SNEG is capable of providing solutions to a variety of different finite size spin models, i.e. for the Hubbard, Heisenberg and t-J models. Since SNEG is implemented in Mathematica, both analytic and numeric solutions are obtainable. The downside is that Mathematica code is not as performant as C++ or Fortran code, thereby limiting the system size that can be studied. However for the systems sizes relevant to this thesis SNEG and Mathematica are sufficient. If larger system sizes are to be studied, more performant software tools (that only give numeric solutions) like ALPS [165] are available. Furthermore analytic solutions derived by symmetry arguments are available for certain systems, see for instance [166].

3.1.2 Hubbard model example for two sites and two particles

Here we provide an example for the two-site Hubbard model with two spin $1/2$ fermions. We outline the analytic solution and provide the corresponding Mathematica SNEG code. The Hubbard Hamiltonian for a two-site, spin $1/2$ system in second quantization (see equation (3.1)) is given as:

$$H = U(\hat{n}_{1\uparrow}\hat{n}_{1\downarrow} + \hat{n}_{2\uparrow}\hat{n}_{2\downarrow}) - t\left(\hat{c}^\dagger_{1\uparrow}\hat{c}_{2\uparrow} + \hat{c}^\dagger_{2\uparrow}\hat{c}_{1\uparrow} + \hat{c}^\dagger_{1\downarrow}\hat{c}_{2\downarrow} + \hat{c}^\dagger_{2\downarrow}\hat{c}_{1\downarrow}\right), \tag{3.2}$$

$$\begin{aligned} H =& U\left(\hat{c}^\dagger_{1\downarrow}\hat{c}_{1\downarrow}\hat{c}^\dagger_{1\uparrow}\hat{c}_{1\uparrow} + \hat{c}^\dagger_{2\downarrow}\hat{c}_{2\downarrow}\hat{c}^\dagger_{2\uparrow}\hat{c}_{2\uparrow}\right) \\ & - t\left(\hat{c}^\dagger_{1\uparrow}\hat{c}_{2\uparrow} + \hat{c}^\dagger_{2\uparrow}\hat{c}_{1\uparrow} + \hat{c}^\dagger_{1\downarrow}\hat{c}_{2\downarrow} + \hat{c}^\dagger_{2\downarrow}\hat{c}_{1\downarrow}\right). \end{aligned} \tag{3.3}$$

The basis set that spans the Hilbert space of this Hamiltonian consists of four basis functions. There are many equivalent notations for these basis functions in literature and we have given three common ones in equations (3.4) to (3.7):

$$b_1 = \hat{c}^\dagger_{2\uparrow}\hat{c}^\dagger_{2\downarrow} = |RR\rangle = |\circ, \uparrow\downarrow\rangle\,, \tag{3.4}$$

$$b_2 = \hat{c}^\dagger_{1\downarrow}\hat{c}^\dagger_{2\uparrow} = |RL\rangle = |\downarrow, \uparrow\rangle\,, \tag{3.5}$$

$$b_3 = \hat{c}^\dagger_{1\uparrow}\hat{c}^\dagger_{2\downarrow} = |LR\rangle = |\uparrow, \downarrow\rangle\,, \tag{3.6}$$

$$b_4 = \hat{c}^\dagger_{1\uparrow}\hat{c}^\dagger_{1\downarrow} = |LL\rangle = |\uparrow\downarrow, \circ\rangle\,. \tag{3.7}$$

In the following we will use the L, R basis function notation, where L and R represent site 1 and 2 respectively. The resulting Hubbard Hamiltonian matrix is:

$$\mathscr{H} = \begin{bmatrix} U & t & -t & 0 \\ t & 0 & 0 & t \\ -t & 0 & 0 & -t \\ 0 & t & -t & U \end{bmatrix}. \tag{3.8}$$

Diagonalization of this Hamiltonian yields the eigenvalues:

$$E_1 = \frac{1}{2}\left(U - \sqrt{16t^2 + U^2}\right), \tag{3.9}$$

$$E_2 = 0, \tag{3.10}$$

$$E_3 = U, \tag{3.11}$$

$$E_4 = \frac{1}{2}\left(U + \sqrt{16t^2 + U^2}\right). \tag{3.12}$$

The eigenfunctions corresponding to these eigenvalues are:

$$\Phi_{H1} = \frac{1}{N_1}\left(|LL\rangle - \frac{\sqrt{16t^2+U^2}+U}{4t}|RL\rangle + \frac{\sqrt{16t^2+U^2}+U}{4t}|LR\rangle + |RR\rangle\right), \tag{3.13}$$

$$\Phi_{H2} = \frac{1}{N_2}\left(|RL\rangle + |LR\rangle\right), \tag{3.14}$$

$$\Phi_{H3} = \frac{1}{N_3}\left(|LL\rangle - |RR\rangle\right), \tag{3.15}$$

$$\Phi_{H4} = \frac{1}{N_4}\left(|LL\rangle + \frac{-U+\sqrt{16t^2+U^2}}{4t}|RL\rangle - \frac{\sqrt{16t^2+U^2}-U}{4t}|LR\rangle + |RR\rangle\right), \tag{3.16}$$

and the normalization factors dividing the eigenfunctions are given as:

$$N_1 = \sqrt{\frac{\left(\sqrt{16t^2+U^2}+U\right)^2}{16t^2} + \frac{\left(\sqrt{16t^2+U^2}+U\right)^2}{16t^2} + 2}, \tag{3.17}$$

$$N_2 = \sqrt{2}, \tag{3.18}$$

$$N_3 = \sqrt{2}, \tag{3.19}$$

$$N_4 = \sqrt{\frac{\left(U-\sqrt{16t^2+U^2}\right)^2}{16t^2} + \frac{\left(\sqrt{16t^2+U^2}-U\right)^2}{16t^2} + 2}. \tag{3.20}$$

These results can be easily checked using SNEG and the corresponding ready to run Mathematica code is given in Appendix section B.1.

While the two-particle Hubbard model solution is trivial, SNEG quickly becomes useful for larger systems that involve larger bases, different tunneling couplings between sites or additional extended Hubbard model terms.

3.2 Extended Hubbard model

The extended Hubbard model [167] is a generalization of the standard Hubbard model, that adds additional terms to the Hamiltonian. There are a lot of different varieties of extended

Hubbard models, depending on which terms are added. In the following we introduce some of the most common additional terms.

Off-site interaction

To include off-site interaction (corresponding to density-density interaction across sites), one adds the following term to the Hubbard Hamiltonian

$$H_{\text{off-site}} = V \sum_{<i,j>} \hat{n}_i \hat{n}_j, \tag{3.21}$$

---

where:

$< i, j >$: represents the sum over neighrest neighbors

$\hat{n}_i$: the spin independent number operator defined as $\hat{n}_i = \hat{n}_{i\uparrow} + \hat{n}_{i\downarrow}$

V: the off-site interaction parameter

Density dependent tunneling

Density dependent tunneling (which is a modification of the tunneling parameter due to possible occupation of the tunneling sites) can be written in many equivalent forms, here we follow the notation from [168]

$$H_{\text{density dependent tunneling}} = \sum_{<i,j>,\sigma} -\Delta t \left(\hat{c}^{\dagger}_{i,\sigma} (\hat{n}_{i,-\sigma} + \hat{n}_{j,-\sigma}) \hat{c}_{j,\sigma} \right), \tag{3.22}$$

---

where:

$< i, j >$: represents the sum over neighrest neighbors

σ: represents the up ($\uparrow$) and down ($\downarrow$) spin

$\hat{n}_{i\sigma}$: the number operator defined as $\hat{n}_{i\sigma} = \hat{c}^{\dagger}_{i,\sigma} \hat{c}_{i,\sigma}$

Δt: the parameter modifying the tunneling

Two particle tunneling

To take into account two particle tunneling (where either two particles switch places, or two particles tunnel together), one adds the terms

$$H_{\text{two particle tunneling}} = \sum_{<i,j>,\sigma,\sigma'} J\hat{c}^{\dagger}_{i,\sigma}\hat{c}^{\dagger}_{j,\sigma'}\hat{c}_{i,\sigma'}\hat{c}_{j,\sigma} + J'\hat{c}^{\dagger}_{i,\sigma}\hat{c}^{\dagger}_{i,\sigma'}\hat{c}_{j,\sigma'}\hat{c}_{j,\sigma}, \tag{3.23}$$

---

where:	
$< i, j >$:	represents the sum over neighrest neighbors
σ, σ':	represents the up ($\uparrow$) and down ($\downarrow$) spin
J, J':	are the two particle tunneling parameters

A very good introduction to these extended Hubbard model parameters can be found in [167]. Experimentally many systems have been considered and realized which go beyond the standard Hubbard model physics [93, 169–172]. In the course of this thesis we studied certain systems where the use of the extended Hubbard model is imperative (in particular excited states in multi-plaquette configurations) and are planning to present our results in a future paper.

3.3 t-J Hamiltonian

A $t - J$ Hamiltonian can be derived from the Hubbard model after elimination of states with double occupancy [173–176] and is given as:

$$\hat{H} = -t \sum_{<i,j>,\sigma} \left(\hat{a}^{\dagger}_{i\sigma} \hat{a}_{j\sigma} + \hat{a}^{\dagger}_{j\sigma} \hat{a}_{i\sigma} \right) + J \sum_{<ij>} \left(\overrightarrow{S_i} \cdot \overrightarrow{S_j} - \frac{n_i \, n_j}{4} \right), \tag{3.24}$$

---

where:

$< i, j >$:	represents the sum over neighrest neighbors
σ:	represents the up ($\uparrow$) and down ($\downarrow$) spins
J:	is the coupling constant ($J = 4t^2/U$ with U being the onsite repulsion)
n_i:	the particle number at site i ($n_i = \sum_{\sigma} \hat{a}^{\dagger}_{i\sigma} \hat{a}_{i\sigma}$)
$\overrightarrow{S_i}$:	is the spin operator for site i ($\overrightarrow{S_i} = (S_{xi}, S_{yi}, S_{zi})$)

For a spin $1/2$ system $\overrightarrow{S_i}$ is given as $\overrightarrow{S_i} = \frac{1}{2}(\sigma_{xi}, \sigma_{yi}, \sigma_{zi})$ where σ represents the Pauli matrices

$$\sigma_{xi} = \begin{pmatrix} 0 & 1 \\ 1 & 0 \end{pmatrix}, \tag{3.25}$$

$$\sigma_{yi} = \begin{pmatrix} 0 & -i \\ i & 0 \end{pmatrix}, \tag{3.26}$$

$$\sigma_{zi} = \begin{pmatrix} 1 & 0 \\ 0 & -1 \end{pmatrix}, \tag{3.27}$$

and the index i indicates that they act on site i. A mathematical derivation can be found in [177].

The $t-J$ Hamiltonian has been extensively studied in the context of strongly correlated materials, in particular in the context of cuprate high T_c superconductivity [178–180].

In chapter 5 section 5.2 we use a slightly different variant of the $t-J$ Hamiltonian where don't couple sites but geometric configurations between which the system can resonate (namely 2-1 and 1-2).

The software packages mentioned in section 3.1.1 also support Hamiltonians containing general spin operators $\overrightarrow{S}$. As such they can be used to solve finite size $t-J$ models. There

are also ample numerical studies of finite size $t-J$ models already present in the literature, i.e [181–184].

3.4 Heisenberg model

The Heisenberg model is given as:

$$\hat{H} = \frac{1}{2}\sum_{i}^{N}\left(J_x\sigma_i^x\sigma_{i+1}^x + J_y\sigma_i^y\sigma_{i+1}^y + J_z\sigma_i^z\sigma_{i+1}^z\right), \tag{3.28}$$

---

where:

N: is the number of sites

$\sigma_i^x, \sigma_i^y, \sigma_i^z$: are the pauli spin matrices acting on site i (defined in equations (3.25) to (3.27))

J_x, J_y, J_z: is the coupling constant in the x, y, z direction

This Hamiltonian gives rise to a wide variety of specialized Hamiltonians each with a large set of literature devoted to it. If $J_x = J_y = J_z$ the resulting Heisenberg model is referred to as the XXX model and if $J_x = J_y \neq J_z$ the model is known as the XXZ model (with the XX model as a special where $J_x = J_y$ and $J_z = 0$). In general all the tunneling coefficients can be different between individual sites.

In this thesis we are mostly concerned with the XXX case of the Heisenberg model. It emerges from the Hubbard model in a perturbative expansion in the $U >> t$ limit [177, 185, 186] for a spin $S = 1/2$ system at half filling (in this limit $J = 4t^2/U$). This allows us to simplify the Hubbard model calculations in the limit of strong interactions. The XXX Heisenberg model is often expressed in terms of spin operators in which case it takes on the following form:

$$H_{Heis} = \sum_{<ij>} J\overrightarrow{S_i} \cdot \overrightarrow{S_j}, \tag{3.29}$$

---

where:

$\overrightarrow{S_i}$: is defined as $\overrightarrow{S_i} := (S_i^x, S_i^y, S_i^z) = \frac{1}{2}(\sigma_i^x, \sigma_i^y, \sigma_i^y)$

$\sigma_i^x, \sigma_i^y, \sigma_i^z$: are the pauli spin matrices acting on site i

J: is the coupling constant in the x, y, z direction

It is often useful to write the Heisenberg model in its second quantized form. This can be achieved [177, 187] by using

$$S_i^x = \frac{1}{2}\sum_{\zeta\zeta'} a_{i\zeta}^\dagger \sigma_{\zeta\zeta'}^x a_{i\zeta'} \tag{3.30}$$

$$S_i^y = \frac{1}{2}\sum_{\zeta\zeta'} a_{i\zeta}^\dagger \sigma_{\zeta\zeta'}^y a_{i\zeta'} \tag{3.31}$$

$$S_i^z = \frac{1}{2}\sum_{\zeta\zeta'} a_{i\zeta}^\dagger \sigma_{\zeta\zeta'}^z a_{i\zeta'}, \tag{3.32}$$

---

where:

$\zeta\zeta'$: sum over the possible spins ($\uparrow$ and $\downarrow$ for spin 1/2 particles)

$\sigma^x, \sigma^y, \sigma^z$: are the pauli spin matrices

To solve the Heisenberg model the software packages mentioned in section 3.1.1 can be used.

CHAPTER 4

WAVE FUNCTION ANATOMY OF TWO FERMIONS IN A DOUBLE WELL

In our publication [133] we studied two ultracold fermions in a double-well. Understanding the double well system is essential since it forms a building block for the design and analysis of larger ultracold atom experiments and ultimately quantum simulators. Experimental realization of this system was first achieved in 2015 by a group around Selim Jochim in Heidelberg [99], who were able to build a controllable two particle double well system with tuneable interaction strength. This system was used to investigate tunneling rates as a function of the interaction strength and potential shape. The group was able to show that their results are in good agreement with predictions obtained through the Hubbard model.

However the drawback of the Hubbard model is that as a spin model it doesn't contain any information about the detailed microscopic structure of the states, to which both the spin and space part of the wavefunction contribute. Our calculations allowed us to unravel details of the spin and space wavefunction, its entanglement and the full spectra from very strong attraction to very strong repulsion. In addition we analyzed in detail the influence of a tilt in the double well potential. We also investigated the evolution of the energy spectrum from a single to a double well.

There are two possible realizations of a double well system, both of which are analyzed in the following. The first option is a one dimensional linear double well system (DWLI). In this case the external potential looks like the potential displayed in figure 2.1. The confining frequency in y is so large that it has no influence on the low energy spectrum and the system can be treated as being quasi one dimensional along x. This configuration we study in section 4.1.

The other double well system is formed by two parallel one-dimensional needles (DWPA) connected by a smooth neck as schematically shown in figure 4.1. This configuration is an-

alyzed in section 4.2.

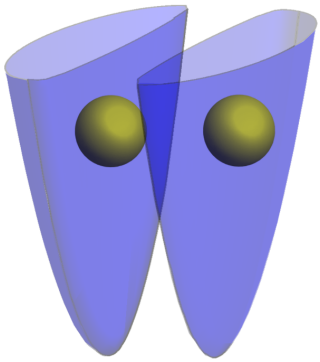

Figure 4.1: Schematic of a parallel double well potential (DWPA) with one particle in each well. The two wells are connected through a high inter-well barrier along the tightly confined x direction ($\hbar\omega_x \gg \hbar\omega_y$). As we show in our analysis of the DWPA system (see section 4.2 for more details) the low energy physics of this system is identical to the DWLI system.

Technical details:

The following paragraphs provide technical details about the calculation and are not needed to follow the arguments in the text. They can be skipped until the details become relevant to the reader.

As mentioned in section 2.1 our calculations are inherently two-dimensional. The interaction strength g should therefore have units of " energy $\cdot$ length^2 ". However in this chapter we are interested in quasi one dimensional systems, which is why we give the interaction strength g in units of $l_0\hbar\omega$ (the length scale of the tightly confined direction is absorbed into the value of g). This also allows a more direct comparison with the results in [99]. As an interaction potential we use a 1D delta function (see equation (2.3) in chapter 2) along the x and y direction (our Hamiltonian is separable in x and y).

Details regarding the comparison with experiments:

The calculations performed in this thesis were done in 2D, while any experimental realization is necessarily a system in 3D. Instead of the two open wells depicted in figure 4.1, experimentally the system looks like two parallel needles (sometimes also referred to as two parallel cigars), where the needle shape is formed by the equipotential surfaces in 3D. The reason why such a 3D system can be directly related to our DWPA and DWLI configurations is that the low energy physics (ground and first few excite states) are determined by the states along the weakest confinement direction and the lowest energy state (states in the case of degeneracy) of the other confining directions. I.e. our DWLI configuration has a degenerate ground state in x and a first excited state along x that is $\approx 1\hbar\omega$ above the degenerate ground state. Our DWPA system has a degenerate ground state in x and a first excited state along y that is $\approx 1\hbar\omega$ above the degenerate ground state (the excited states along x are significantly higher in energy). This is why the lowest energy results are the same. The same applies for two parallel needles in 3D, which have a degenerate ground state in x, low lying excited states along y and other high energy excited states along x and z. See section 4.2 for more details.

4.1 Linear double well (DWLI)

First we focus on the analysis of the linear double well (DWLI) system. We performed detailed studies of the evolution of the spectrum over the full range of interaction strengths. Moreover we studied the crossover from a single to a double well and the influence of a tilt. Furthermore we studied the wave function anatomy (through SPDs and SR-CPDs) for selected parameters and analyzed the entanglement of the wavefunction through the von Neumann entropy.

A DWLI system can for instance be realized through trap parameters like $\omega_x/(2\pi) = 1\,\mathrm{kHz},\ \omega_y/(2\pi) = 100\,\mathrm{kHz}, d = 1\,\mu\mathrm{m}, V_b/h = 5.4\,\mathrm{kHz}$.

4.1.1 Symmetric (no tilt) linear double well

Figure 4.2 analyzes the evolution of the two particle spectra without tilt ($\Delta = 0$) from a single well $d = 0, \;\; V_b/h = 0$ to a full double well $d = 2\,\mu\mathrm{m}, \;\; V_b/h = 5.4\,\mathrm{kHz}$. There are two different types of energy levels in figure 4.2, horizontal lines that are independent of the interaction strength g and energy curves that are dependent on g. The horizontal lines consist of triplet states and Heitler London (HL) type states. The triplet states are always independent of the interaction strength due to the exchange hole imposed by the Pauli principle. These states can be found in all the panels of figure 4.2. The HL type non-interacting states are only present in the fully separated double well case (figure 4.2 c). The HL type states are singlets where one atom is localized in each well: $|L\uparrow R\downarrow\rangle \pm |R\uparrow L\downarrow\rangle$ where L denotes left and R denotes right. They are present in panel b) and c) of figure 4.2, although they are only non-interacting in the fully separated double well case (figure 4.2 panel c). These states are reminiscent of the highly entangled bell states [188]. There is a second type of singlet states which are states where both particles are occupying the same well. In those cases the two atoms form a repulsively localized bound state with increasing repulsive interaction (a Wigner molecule, for more details on Wigner molecules formed by ultracold atoms see section 4.1.2 and [132, 133, 135, 189]). Those states show very strong g dependence, have strong entanglement and are remaniscent of NOON states [190], where NOON is a designation for a state having N particles in one site and 0 particles in the other $|N0\rangle \pm |0N\rangle$ (in our two particle case this corresponds to $|L\uparrow L\downarrow\rangle \pm |R\uparrow R\downarrow\rangle$). The pair of degenerate first excited states (blue and orange color) in the repulsive range $(-1/g < 0)$ of figure 4.2 c) are NOON states as well as the pairs of degenerate g dependent states in the attractive range $-1/g > 0$ (green and red as well as orange and gray).

As the interwell barrier is being decreased the former Heitler London type singlet states experience an increasing interaction across the barrier, which causes them to develop a dependence on the interaction strength as shown in figure 4.2 b). The previously present double degeneracy of the horizontal energy levels is gradually lifted until the single well

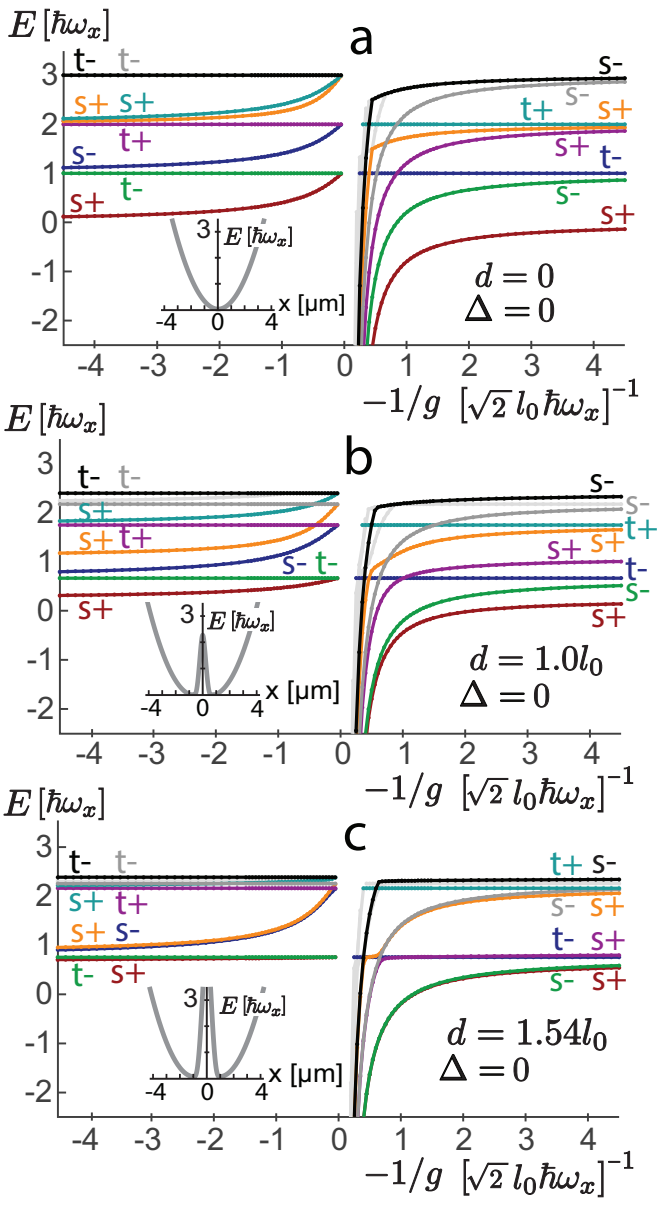

Figure 4.2: Evolution of the energy spectra of two fermions as a function of the interaction strength for three values of the well separation $d = 0$, $d = 1.297\,\mu\text{m}$, $d = 2\,\mu\text{m}$ with an interwell barrier of $V_b/h = 0$, $V_b/h = 2.273\,\text{kHz}$ ($\epsilon_b = 18.18$), $V_b/h = 5.4\,\text{kHz}$ ($\epsilon_b = 18.18$) respectively (no tilt ($\Delta = 0$)). The trapping frequencies are $\omega_x/(2\pi) = 1\,\text{kHz}$, $\omega_y/(2\pi) = 100\,\text{kHz}$. The parameters for subfigure c) were chosen to reflect the experimental conditions in [99]. The Labels s and t next to the energy levels denote singlet ($S = 0$) and triplet ($S = 1$) respectively. A "+" next to the energy level symbolizes positive overall parity, a "−" negative overall parity. As a length scale reference, the harmonic oscillator length is $l_{0x} = (\hbar/(Mw_x))^{1/2} = 1.297\,\mu\text{m}$ where $M = 9.99 \times 10^{-27}\text{kg}$ is the mass of the ^{6}Li atom. The colors of the energy curves in all three panels are consistent to allow for direct comparison of the states. The insets in panels a-c show a cut of the potential along the x direction.

spectrum of figure 4.2 a) is fully developed.

4.1.2 Two particles in a tilted linear double well

Figure 4.3 shows our results for a tilted linear double well ($\Delta/h = 0.5\,\mathrm{kHz}$) at a separation of $d = 2\,\mu\mathrm{m}$ and an interwell barrier of $V_b/h = 5.4\,\mathrm{kHz}$. In addition to the energy spectrum, we present a detailed analysis showing SPDs (green surfaces) and SR-CPDs (red surfaces) for both ground and excited states. For details on the calculation of SPDs and SR-CPDs see section 2.7. Our calculations reveal intriguing aspects of the resulting wavefunctions.

Space aspects: As with the non tilted DWLI system, discussed in section 4.1, the spectrum of the tilted DWLI system consist of states with two particles in one well and states with one particle in either well (HL type). However due to the tilt and the resulting broken parity symmetry along x, there are no NOON states formed. Instead particles are either localized in the left ($|L\uparrow L\downarrow\rangle$) or right well ($|R\uparrow R\downarrow\rangle$). HL type states are shown in panels b,h,f and doubly occupied well states are shown in panels a,c,d,e,g.

Spin aspects: HL type and doubly occupied states can be singlet ($S = 0$) or triplets ($S = 1$). HL type singlets are shown in b,f and a HL type triplet is shown in h. Doubly occupied singlets are present in a,c,d,e and a doubly occupied triplet is shown in g.

Development of the states: The ground state (gs, red curve) in the noninteracting limit, consists of the two atoms occupying the lowest energy orbital in the left well $|L\uparrow L\downarrow\rangle$ and is therefore a single determinant wavefunction. With increasing repulsion (towards $-1/g = -0$ in figure 4.3) an anticrossing develops between the gs and first excited singlet (blue curve, HL type state, $|L\uparrow R\downarrow\rangle \pm |L\downarrow R\uparrow\rangle$) and for very strong repulsion (near $-1/g = -0$) the gs is a HL type state.

Formation of ultracold wigner molecules: Of particular interest are the states depicted in panel d and e. The SPD in e clearly shows a double humped density, indicating that the two fermions, which are occupying the left well, are localizing due to the strong repulsive interaction. This is in perfect analogy to the formation of Wigner molecules, as they

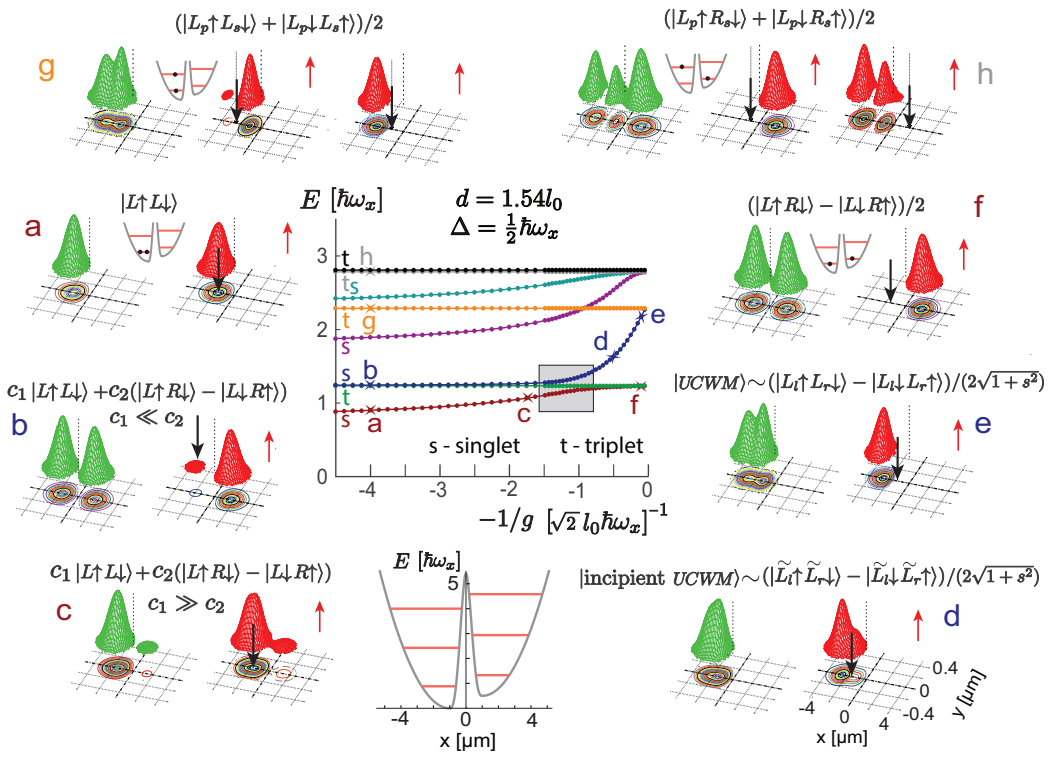

Figure 4.3: Tilted double well with two fermionic atoms. The SPDs (green surfaces) and SR-CPDs (red surfaces) in panels a,b,g,h are calculated with an interaction strength of $-1/g = -4/(\sqrt{2}l_0\hbar\omega_x)$, in panel c with $-1/g = -1.70/(\sqrt{2}l_0\hbar\omega_x)$, in panel d with $-1/g = -0.5/(\sqrt{2}l_0\hbar\omega_x)$ and in panel e and f with $-1/g = -0.1/(\sqrt{2}l_0\hbar\omega_x)$. The states displayed in these panels are marked with a star in the energy spectrum. s and t next to the energy levels denote singlet and triplet respectively. The upper case labels L and R correspond to space orbitals localized on the left and right wells. The lower case subscripts l and r (present in panels e and d) denote space orbitals localized on the left and right side *within* in a single well. The lower case subscripts s and p (as seen in panels g and h) indicate the single particle ground state (no-nodes $\Rightarrow$ s) or the first excited state (one node $\Rightarrow$ p). A tilde above the labels L and R (see incipient UCWM, panel d) indicates that the localization is not as pronounced as for a fully developed UCWM. The symbol s in $2(1+s^2)^{1/2}$ represents the overlap of left and right space orbitals. The black arrow in the SR-CPDs represents the location of the spin-down fermion and the red arrow indicates that the red surfaces represent the density for the spin-up atom. The parameters of this calculation are $\omega_x/(2\pi) = 1\,\text{kHz},\ \omega_y/(2\pi) = 100\,\text{kHz},\ V_b/h = 5.4\,\text{kHz}$. Panels a,g,f,h and the inset below the spectrum show a cut of the external confining potential along the x direction. As a length scale reference, the harmonic oscillator length $l_{0x} = (\hbar/(Mw_x))^{1/2}$ is $l_{0x} = 1.297\,\mu\text{m}$ where $M = 9.99 \times 10^{-27}\text{kg}$ is the mass of the ^{6}Li atom.

have been predicted [135][134][191][142] and experimentally found [135][192][193][194] in electron quantum dots. In order to emphasize the emergence of this universal behavior we call the strongly localized one-well states ultracold wigner molecules (UCWM). The two-atom UCWM in panel e) can be approximated by an *interwell* HL configuration $|L_l \uparrow L_r \downarrow\rangle \pm |L_l \downarrow L_r \uparrow\rangle$ where L_l denotes the left hump in the left well and L_r denotes the right hump in the left well as seen in the SPD. The panel in d shows an incipient UCWM. The consequences of the formation of UCWMs in systems of ultracold atoms are far reaching and allow for instance the mapping of the system to spin chains [132][195].

Connection to fermionization: For very strong repulsion the UCWM may reach the regime of fermionization, a regime that has been experimentally observed in [98]. In this limit the gs (red curve) becomes degenerate with the one-well triplet state (orange curve). Fermionization predicts that at this point the square modulus of the wavefunction of the singlet and triplet become identical [98]. This behavior is observed in our calculations in both the SPD and SR-CPD, as can be seen by comparing panels g and e.

Further analysis: We furthermore analyzed the resonance region (grey rectangle in figure 4.3) and the connection of the observed wavefunctions to the Bell states. Both aspects are described and explained in detail in [133] and for the sake of avoiding undue repetition not reproduced here.

4.1.3 Entanglement analysis of two particles in a tilted linear double well

In figure 4.4 we study the entanglement characteristics of two particles in a tilted double well. The spectrum (top of figure 4.4) is the same as in figure 4.3 and reproduced for the convenience of the reader. The curves in the bottom of figure 4.4 show the corrsponding von Neuman entanglement entropy. The von Neumann entropy is defined as $S_{vN} = \mathrm{Tr}(\rho \log_2(\rho)) - \log_2(N)$, where ρ is the single particle density matrix and N is the number of particles. For details see section 2.7.6. Both attractive ($-1/g > 0$) and repulsive ($-1/g < 0$) interparticle interactions are considered. The colors of the energy levels in

the spectrum match the colors of the entanglement curves. In the left half of the figure we present a detailed analysis of the UCWM, in the right half of the figure we show the SPDs and SR-CPDs for six selected states. The states for which we show the SPDs and SR-CPDs are marked with stars on the levels in the energy spectrum and in the entanglement plot. The bar charts next to a,b and g show the occupation numbers of the natural orbitals.

In the case of a triplet (fully polarized state) the von Neumann entropy is $S_{vN} = 1$ independently of the interaction strength g (the spatial wave function needs to satisfy the Pauli principle and the resulting Pauli hole ensures that the contact interaction doesn't act on the triplet states). Therefore all the triplet states in the von Neumann entropy plot collapse to a single horizontal line (see the horizontal lines in both the attractive and repulsive parts of the entanglement entropy plot in figure 4.4). Furthermore the von Neumann entropy for the dark brown and purple curves approaches 0 in the non interacting limit (both on the repulsive side of the spectrum ($-\frac{1}{g} \to -\infty$) and on the attractive side of the spectrum ($\frac{1}{g} \to \infty$)). The reason for this behavior is that in the weakly interacting regions ($g \to 0$) the states approach single-determinant wavefunctions: $|L\uparrow L\downarrow\rangle$ in the case of the dark-brown state and $|R\uparrow R\downarrow\rangle$ for the purple state in figure 4.4. This wavefunction structure also becomes apparent in the SPD plots in panel e and f.

The non-interacting limit in the attractive region ($-1/g \to \infty$) behaves correspondingly, with the ground (brown curve) and 2nd excited state (purple curve) approaching the single-determinant wavefunctions (see panel e and f for the SPDs which correspond to $|L\uparrow L\downarrow\rangle$ and $|R\uparrow R\downarrow\rangle$ respectively). In panels a,b,c and d of figure 4.4 we analyze the first excited state in the attractive region (green curve) at different interaction strengths. Interestingly it develops a minimum in the entanglement entropy (see point b in the entanglement entropy plot), where the state is close to a single-determinant state (see bar plot in panel b). For strong interactions however the number of involved Slater determinants grows significantly as can be seen from the bar plot in panel a.

Panel g shows a detailed analysis of the UCWM (its position in the energy spectrum is

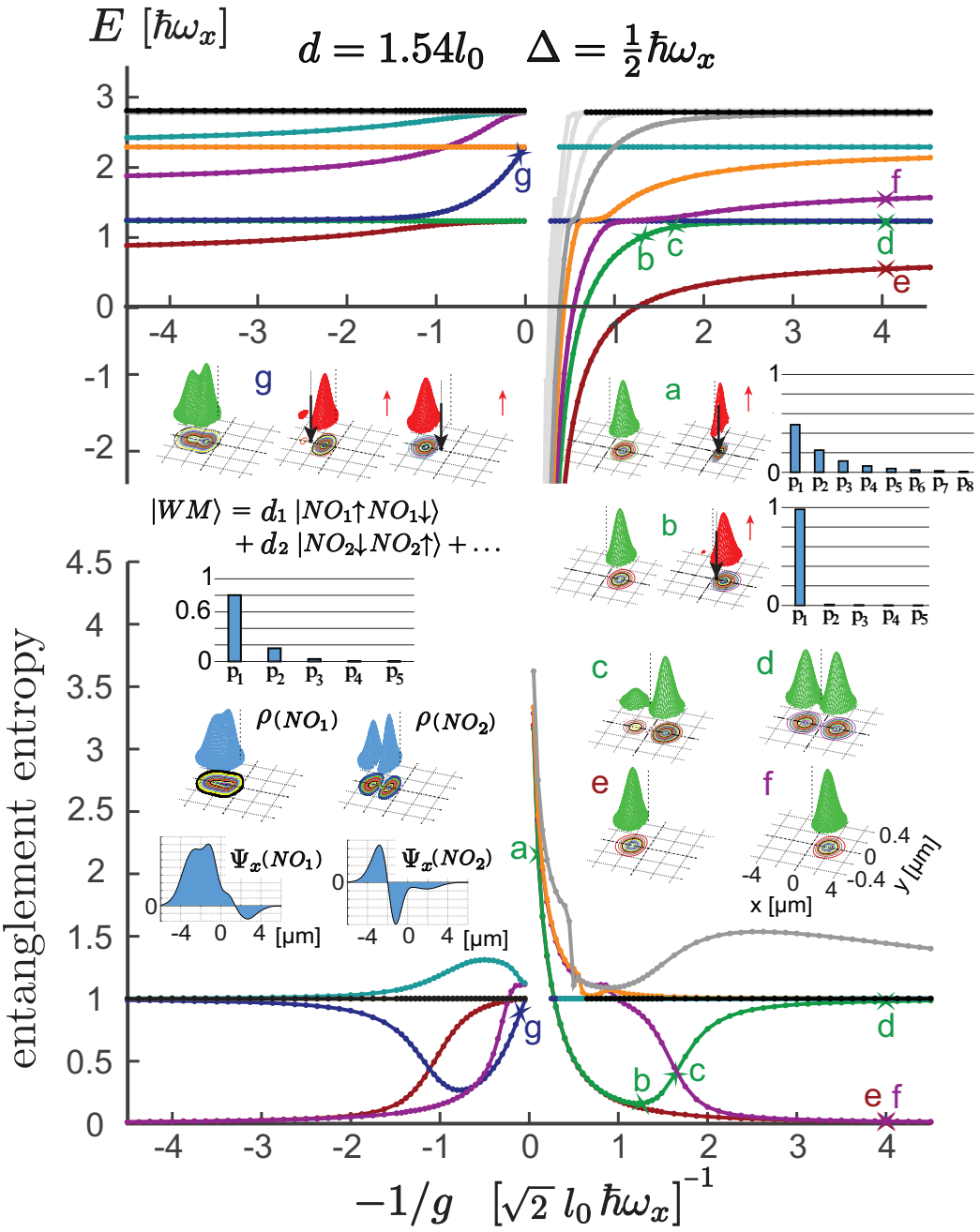

Figure 4.4: Entanglement characteristics of a tilted double well with two particles. For a detailed description and discussion of this plot see section 4.1.3. The tilt is $\Delta/h = 0.5\,\mathrm{kHz}$. The distance between the minima in the double well is $1.54 l_0 = 2\,\mu\mathrm{m}$ where $l_0 = 1.297\,\mu\mathrm{m}$ is the harmonic oscillator length for the mass of 6Li atoms and a trapping frequency of $1\,\mathrm{kHz}$. For both the right and the left well $\omega_x/(2\pi) = 1\,\mathrm{kHz}, \omega_y/(2\pi) = 100\,\mathrm{kHz}$. Furthermore $V_b = 18.18 V_0$ with $V_0/h = 0.297\,\mathrm{kHz}$. For a detailed description of these parameters see section 2.2.

marked wit a star and the label g). In the top part of panel g we show the SPD (green) and two SR-CPDs (red). Below the densities, we show an equation illustrating the expansion of the UCWM wavefunction in terms of natural orbitals (NO), below which we show a bar plot of the eigenvalues of the single particle density matrix (also referred to in literature as the occupation numbers). The orbital density ρ and the orbital wave function cuts Ψ_x for the first two natural orbitals are also given. It is apparent from both the orbital density and the wave function cut along x that the first NO of the UCWM is two-peaked in contrast to the non-interacting case which is single-peaked (not shown).

It is remarkable that in the repulsive case the maximum of the entanglement entropy stays below 1.3. In contrast the value of the entanglement entropy grows without bounds in the strongly attractive region $-\frac{1}{g} \to +0$ (a tightly bound dimer). Due to the connection between the von Neuman entropy and the natural orbitals (see section 2.7.5) this implies that a large number of Slater determinants is needed to describe the strongly attractive state (it is highly correlated). This can also be seen from the occupation number bar plot in figure 4.4, panel (a).

4.2 Parallel double well (DWPA) and comparison with experiment

A double well potential for ultracold atoms is experimentally realized using optical tweezers [99][106]. Therefore the full 3D potential looks like two parallel needles, with a confined (high trapping frequency) radial direction and a free (low trapping frequency) axial direction. The needles are placed in close proximity, effectively creating a double well. A double well parallel configuration (DWPA) in our calculations can for instance be realized through trap parameters like $\omega_x/(2\pi) = 6.6\,\mathrm{kHz},\ \omega_y/(2\pi) = 1\,\mathrm{kHz}, d = 2.5\,\mu\mathrm{m}, V_b/h = 10.0\,\mathrm{kHz}$ and is illustrated in figure 4.1. This configuration is different from the DWLI configuration that we analyzed so far in the sense that the unconfined direction is along y, instead of along x. This of course raises the question on whether our results from the DWLI system are applicable to the DWPA system. This is discussed in the following section.

4.2.1 CI results for the DWPA configuration

To study the effects of the DWPA orientation, we calculated the energy spectrum for a symmetric double well (no-tilt) in analogy to figure 4.2 c. The result is shown in figure 4.5 a and exhibits the same degeneracy patterns and the same dependence of the energy on g as figure 4.2 c. Furthermore we calculated the SPDs (green) and SR-CPDs (red) for the points labeled A and B in figure 4.5. This revealed the formation of HL type and NOON states in perfect analogy to the analysis of section 4.1. More importantly the formation of the UCWM (see figure 4.5 c) is in perfect agreement with what had previously been found for the case of the tilted DWLI system (compare figure 4.3 e). The only difference is that the UCWM now develops along the y axis instead of along x and that it appears symmetric in both wells due to the parity conserving external potential (the external potential used for the calculations in figure 4.5 is not tilted), thereby forming a NOON state. This leads us to conclude that the system behavior is independent of the DWLI and DWPA orientation as long as one restricts oneself to the lower energy branches of the spectrum. Naturally higher excited states along the confined directions will exhibit differences.

Mapping of the CI results to Hubbard model parameters

Figure 3 in [99] shows the occupation statistics as a function of the Hubbard model parameter U/t and allows us to compare our results against the experimental measurements. *Note that the parameter t in this thesis corresponds to J in [99].* In order to perform this comparison we first need to map our calculation results to Hubbard model parameters, which is described in the following.

To extract the Hubbard model parameters from our results we perform calculations in the DWLI and DWPA case with the following parameters. DWLI: $w_x/(2\pi) = 1\,\mathrm{kHz}, w_y/(2\pi) = 100\,\mathrm{kHz}$, $V_b/h = 5.407\,\mathrm{kHz}$, $d = 2\,\mu\mathrm{m}$. The parameters for the DWPA case are: $d = 2.5\,\mu\mathrm{m}$, $\omega_x/(2\pi) = 6.6\,\mathrm{kHz}$, $\omega_y/(2\pi) = 1\,\mathrm{kHz}$, $V_b/h = 10\,\mathrm{kHz}$. Both sets of parameters represent well separated double wells.

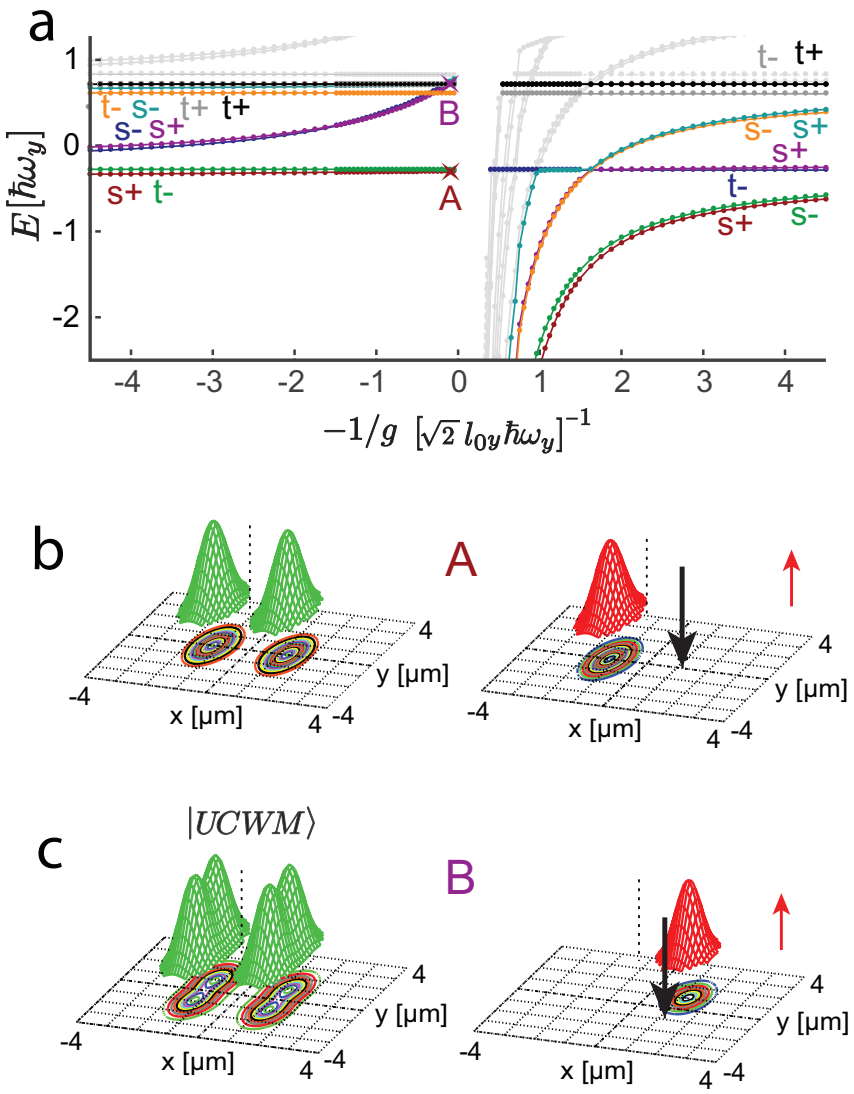

Figure 4.5: Energy spectrum (a) and SPDs and SR-CPDs (b, c) for two particles in a non tilted DWPA trap with large interwell barrier. The parameters of the external potential are: $d = 2.5\,\mu\text{m}, \omega_x/(2\pi) = 6.6\,\text{kHz}, \omega_y/(2\pi) = 1\,\text{kHz}, V_b/h = 10\,\text{kHz}, \Delta/h = 0$. As a length scale reference, the harmonic oscillator length $l_{0x} = (\hbar/(Mw_x))^{1/2} = 0.505\,\mu\text{m}$ where $M = 9.99 \times 10^{-27}\text{kg}$ which is the mass of the ^{6}Li atom. The parameters are in the range of those used in experiments [99]. The black arrow near the SR-CPDs (red surface) shows the location of the spin-down fermion and the red arrow indicates that the red surfaces represents the density for the spin-up atom.

The Hubbard hopping parameter t is obtained from the *non-interacting* energy spectrum of the symmetric double well ($\Delta = 0$) through the energy difference between the singlet ground state and the first excited triplet state, which equals $2t$. For the DWLI configuration this yielded a value of $t/h = 48.73\,\mathrm{Hz}$ and for the DWPA configuration a value of $t/h = 55.33\,\mathrm{Hz}$. This is small compared to the lowest trap frequency of $1\,\mathrm{kHz}$ in the DWLI and DWPA configuration and corresponds to the weak tunneling regime.

The Hubbard onsite interaction strength U is a function of g and determined as the energy difference $E(-1/g) - E(\infty)$ in a *single well*. $E(-1/g)$ is the energy of the interacting ground state and $E(\infty)$ is the ground state energy in the non-interacting limit. In order to obtain this difference we introduced a strong tilt of $\Delta/h = 4.84\,\mathrm{kHz}$ (DWLI) and $\Delta/h = 9.67\,\mathrm{kHz}$ (DWPA) to the external potential while keeping the other trap parameters unchanged. This localizes both particles in one well (even for very strong repulsion) and allows us to calculate the onsite interaction parameter U.

4.2.2 Determination of occupation probabilities and comparison with experiment

Having established the $U(g)$ dependence we calculate SR-CPDs for different values of g in the non-tilted double well. The fixed point of the SR-CPD is placed in the left well ($x < 0$). We then integrate the volume of the SR-CPD separately for $x < 0$ and $x > 0$, which yields the probability for double and single occupancy respectively.

The results of these calculations are displayed in figure 4.6 and overlayed on top of Figure 3 reprinted from [99]. The blue circles and squares represent the experimental data, the red dots correspond to our calculated results for the DWLI configuration, the red triangles correspond to our results for the DWPA configuration. As one can see the results for both configurations of the double well agree well with the experimental results and the limit of the Hubbard model (which is represented by the solid lines).

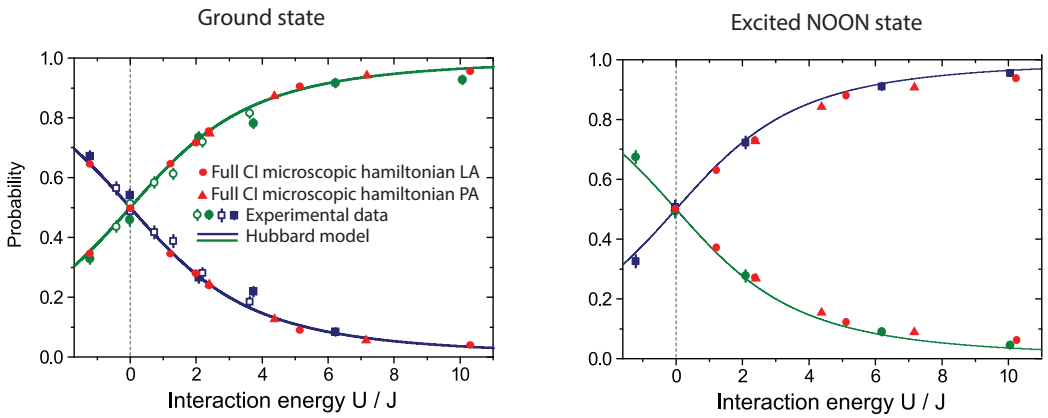

Figure 4.6: Occupation probabilities from [99] compared with our calculated values for the DWLI and DWPA case. The solid lines represent the Hubbard model prediction. Blue squares and green circles represent experimental data, red dots and red triangles represent our CI calculation results for the DWLI and DWPA configuration. For details on how the data was obtained see section 4.2.1. Note the interchange of the blue and green probability curves between the two panels, which is found in both theory and experiment. The parameter t in this thesis corresponds to J in [99]

More information and additional results can be found in our Nano Letters paper [133]:

Benedikt B. Brandt, Constantine Yannouleas, and Uzi Landman. "Double-Well Ultracold-Fermions Computational Microscopy: Wave-Function Anatomy of Attractive-Pairing and Wigner-Molecule Entanglement and Natural Orbitals". In: *Nano Letters* (Sept. 9, 2015)

CHAPTER 5

SPIN CHAINS AND RESONATING SPIN CLUSTERS FROM MICROSCOPIC HAMILTONIANS FOR THREE AND FOUR PARTICLES IN LINEAR AND PARALLEL DOUBLE WELLS

After our studies of the two-particle double well system we were interested in expanding our analysis to higher number of particles, which allows us to study the formation of quantum magnetism (ferromagnetic or anti-ferromagnetic ordering). The models that are needed to describe these systems at strong repulsion turn out to be the Heisenberg model and a variant of the $t - J$ model that is akin to the one used in the study of high T_c superconductivity.

In section 5.1 we first analyze four particles in a double well, after which we study three particles in a double well in section 5.2. The reason for studying four particles first is that four particles arrange themselves symmetrically between the two wells and are therefore easier to analyze. Three particles in a double well have a doubly degenerate ground state, equivalent to a resonance between the right and left well which introduces additional complexity.

> *Technical details:*
>
> *The following paragraphs provide technical details about the calculation and are not needed to follow the arguments in the text. They can be skipped until the details become relevant to the reader.*
>
> As mentioned in section 2.1 the numerical code that runs the calculations is inherently two-dimensional. The interaction strength g should therefore have units of energy $\cdot$ length^2. However in this chapter we are interested in quasi one dimensional systems,

which is why we give g in units $l_0\hbar\omega$. This can be done even in the DWPA cases, where the double well is formed along the x-direction since, we only need to take the lowest two almost degenerate energy levels along the x-direction into account. The important energy and length scales in the DWPA case are along the y direction. As an interaction potential we use a 1D delta function (see equation (2.3) in chapter 2) along the x and y direction (our Hamiltonian is separable in x and y).

5.1 Four particles in a double well

We first analyze four particles in a linear double well (DWLI, see section 5.1.1), before we analyze four particles in a parallel double well (DWPA, see section 5.1.2). We also give some results for four particles in a single well (see figure 5.2) to show the similarities and differences to a double well.

5.1.1 Four particles in a linear double well

Figure 5.1 shows spectra as well as a SPD and a SR-CPD for four particles in a linear double well. The spin projection S_z was chose to be $S_z = 0$ (two spin up atoms and two spin down atoms). The spectra in panel (a) were calculated for an intermediate inter-well barrier, while the spectra in panel (b) were calculated for a high interwell barrier. For both barriers the lowest energy band in the spectrum at very strong repulsion (close to $-1/g = 0$) consists of six states. In panel (a) one can already see the onset of a characteristic 1-2-3 degeneracy pattern in the lowest energy band (close to $-1/g = 0$), which is fully developed for the high interwell barrier (= well separated wells) in panel (b).

Amongst these six states are two with total spin $S = 0$, three with $S = 1$ and one with $S = 2$. This spin pattern can be understood in context of the branching diagram (see figure A.1), which predicts those multiplicities.

The SPD (to the right of panel (a)) and SR-CPD (to the right of panel (b)) in figure 5.1 are plotted for the ground state of the double well system with *high interwell barrier*. The

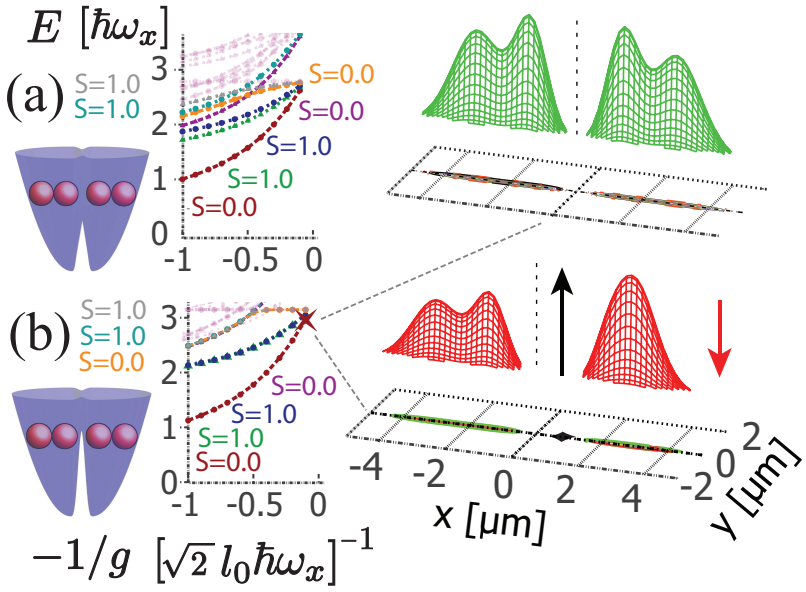

Figure 5.1: This figure shows the spectra for four particles in a double well for two different interwell barriers, together with schematics of the potentials and an SPD and SR-CPD for the ground state of the *high interwell barrier* in the strongly interacting limit (see star in the spectrum in panel (b)). The S_z quantum number in the calculations is $S_z = 0$. The value of zero in the energy spectrum corresponds to the ground state energy for the non interacting system. Alongside each level in the spectrum we annotate the total spin quantum number S (the $S = 2$ state is not explicitly annotated, but can be identified as the lowest horizontal energy level in the spectrum). The distance between the wells is $d = 2.5\,\mu\mathrm{m}$ and the barrier height is $V_b/h = 2.3\,\mathrm{kHz}$ in panel (a) and $V_b/h = 8.5\,\mathrm{kHz}$ in panel (b). In both panels the frequencies for the external confining potential are $\omega_x/(2\pi) = 1\,\mathrm{kHz},\ \omega_y/(2\pi) = 100\,\mathrm{kHz}$.

double hump for the SPD in each well, clearly indicates the presence of a Wigner molecule in each well, a conclusion which is further corroborated by the SR-CPD, where we plot the spin down density given a spin up particle fixed at $x = 0.8\,\mu\mathrm{m}$. As we expect for a Wigner molecule, there is no double occupancy at the fixed point of the SR-CPD and individual humps are clearly visible at the neighboring sites.

5.1.2 Four particles in a parallel double well

Due to the experimental orientation of the optical tweezers, the system that is experimentally realized is going to be in a double well parallel DWPA configuration and in this section we report the corresponding results for four particles. Figure 5.2 shows spectra, SPDs and SR-CPDs for four particles in a single well (panel (a-c)), a double well with intermediate barrier (panel (d)) and a double well with high barrier (panel (e-i)).

A common feature in all three spectra is the formation of a sixfold lowest energy band at strong repulsion with the only difference being the spacing between the energy levels. The single well shown in figure 5.2 (a) has six clearly separated energy levels, converging to a common point at $-1/g = 0$ whereas figure 5.2 (e) has three converging branches with a characteristic 3,2,1 degeneracy. The onset of this grouping of states into a 3,2,1 pattern is visible for the intermediate barrier height displayed in figure 5.2 (d).

The SPDs in figure 5.2 also clearly reveal the formation of an ultracold Wigner molecule (UCWM) in both the single (panel (b)) and double well configuration (panel (f) and (h)) at very strong repulsion. The repulsively created extemporaneous sites in the UCWM are clearly visible in the density (see red numbers denoting the sites above the SPDs and SR-CPDs in figure 5.2). Panels (h) and (i) show the SPD and SR-CPD for the third exited state for the well separated double well. We included this figure to illustrate that the SPD of the UCWM looks identical for the ground state (panel(f)) and third excited state (panel (h)), but the spin configuration is different as is evident by the different SR-CPDs in panel (g) and (i). *This shows that combining SPDs and SR-CPDs is essential in an analysis*

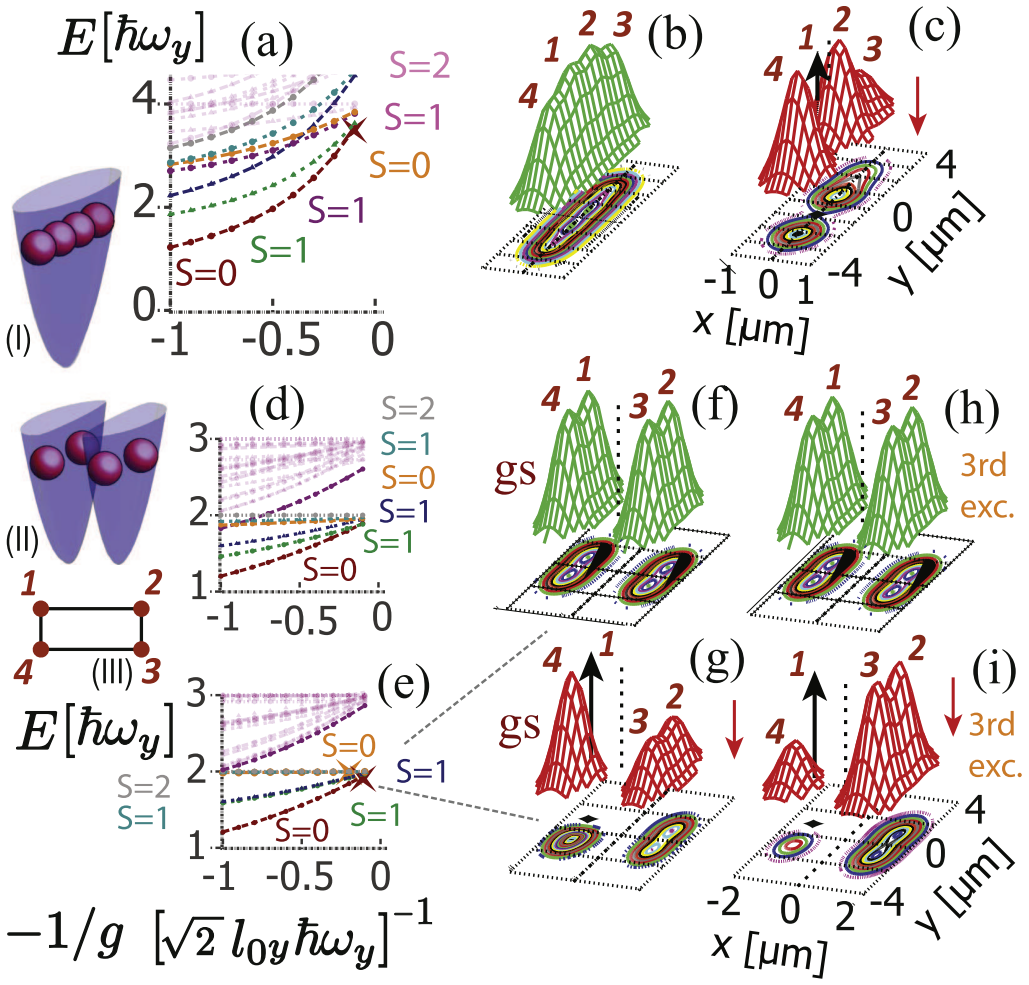

Figure 5.2: Evolution of four particle spectra, SPDs and SR-CPDs from a single well to a fully separated double well. The SPDs and SR-CPDs in (b),(c),(f),(g) correspond to the $S_z = 0, S = 0$ ground state at $-1/g = -0.1(\sqrt{2}l_{0y}\hbar\omega_y)^{-1}$ (red curve in the respective spectra). The SPDs and SR-CPDs in (h),(i) correspond to the $S_z = 0, S = 0$ excited state at $-1/g = -0.2(\sqrt{2}l_{0y}\hbar\omega_y)^{-1}$ (orange curve). g is the 1D contact interaction strength. Panels (I) and (II) are schematics representing the potential and the spatial configuration of the particles. Panel (III) is a schematic showing the labeling of the sites for the Heisenberg model (the site labeling is also annotated above the peaks in the SPDs and SR-CPDs). The parameters of the external trap are $w_x/(2\pi) = 6.6\,\mathrm{kHz}$, $w_y/(2\pi) = 1\,\mathrm{kHz}$, $d = 0$ in panel (a) and $d = 2.5\,\mu\mathrm{m}$ in panel (d) and (e). The interwell barrier is $V_b/h = 0$ in panel (a), $V_b/h = 6.08\,\mathrm{kHz}$ in (d) and $V_b/h = 11.14\,\mathrm{kHz}$ in (e). For additional details on the calculation see the technical details section in the introduction to this chapter.

of the wavefunction, since each individually will only yield an incomplete picture of the wavefunction anatomy.

5.1.3 Similarities between the DWPA and DWLI results and underlying physics

In the previous two sections we saw that the DWPA and DWLI case share many of the same features. Namely

- The appearance of extemporaneously created sites
- The lowest energy band shows a 1-2-3 degeneracy pattern for high inter-well barrier
- For strong repulsion the energy levels of the lowest energy band come together at the horizontal $S = 2$ energy level

This indicates that there is fundamental underlying physical process that yields the same results independent of trap arrangement. This underlying physics is the formation of ultra-cold wigner molecules (UCWM) in each well.

The formation of a UCWM allows us to map the highly repulsive regime of the spectrum to an effective spin model. Each hump in the SPD indicates the position of a localized particle (a site in the spin model). The Hamiltonian reproducing the energy spectrum in figure 5.2 is a 4-site Heisenberg Hamiltonian:

$$H_{Heis} = \sum_{<ij>} J_{ij} \boldsymbol{S_i} \cdot \boldsymbol{S_j} - \sum_{<ij>} J_{ij}/4 \tag{5.1}$$

where the symbol $\langle ij \rangle$ denotes a summation over nearest-neighbor sites. For details on the Heisenberg Hamiltonian and how to solve it, see section section 3.4. The second term in equation (5.1) is a scalar, leading to an overall energy shift.

The parallel double well (DWPA) case in figure 5.2 (d-i) is well described by a 2D Heisenberg ring (as shown schematically in figure 5.2 panel (III) and figure 5.3 panel (a)).

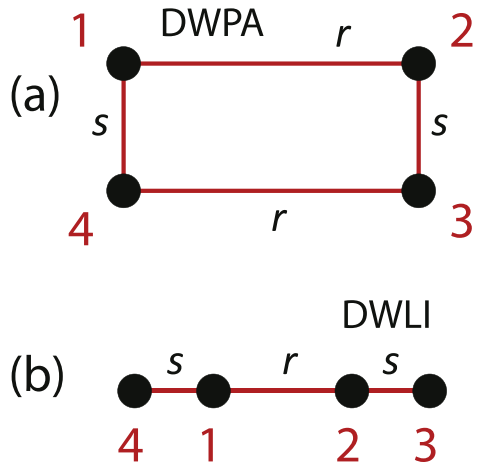

Figure 5.3: Four particle site numbering for a double well parallel (DWPA) and double well linear (DWLI) configuration. r, s represent the different couplings between the localized sites. The interaction between site 1 and 4 and the interaction between site 2 and 3 is between self localized sites and denoted s. The interaction between site 1 and 2 and between site 4 and 3 is through the interwell barrier and denoted r. The arrangement in panel (b) can be obtained from the arrangement in panel (a) by setting the coupling between site 3 and 4 (J_{34}) to zero. This allows one to easily transform the Hamiltonian from a DWPA configuration to a DWLI configuration.

Since the Heisenberg ring in the DWPA case is symmetric under reflection in x and y there are only two exchange constants $J_{12} = J_{34} = r$ and $J_{23} = J_{14} = s$.

The linear double well (DWLI) in figure 5.1 represents an open linear spin chain, with $J_{12} = r$ and $J_{23} = J_{41} = s$ (reflection symmetry along y). The interaction terms and the site numbers are illustrated in figure 5.3 panel (b). The slightly unconventional 4123 numbering of the sites was chosen, because the Heisenberg Hamiltonian for the DWLI case can be easily obtained from the Hamiltonian of the DWPA case by setting $J_{34} = 0$.

The single well case in figure 5.2 (a) is mathematically equivalent to the linear double well case. Only the central (inter-well) coupling J_{12} is different.

As we show in [121] these effective Hamiltonians reproduce the six fold band in the energy spectrum as well as the total spin multiplicities and the spin eigenfunctions of our CI calculation.

5.2 Three ultracold atoms in a double well

Compared to the two particle case, three particles in a double well system exhibit an even richer behavior, that leads amongst other things to the notable formation of a resonating UCWM and the appearance of a $t - J$ like model to describe the energy spectrum. This is remarkable since it has been conjectured [80] [92] that systems of ultracold atoms can be used to simulate complex many body phenomena like high T_c superconductivity.

5.2.1 Three particles in a parallel double well (DWPA)

Figure 5.4 shows spectra, SPDs and SR-CPDs for three particles in a DWPA system for different tilts and interwell barriers. The calculations were performed for three particles with a spin projection $S_z = 0.5$ (two particles with up spin, one particle with down spin). The panels (a)-(i) in figure 5.4 show the results for symmetric (non-tilted) double wells with different interwell barrier heights. Panels (j)-(q) show the results for double wells at two different tilts.

The case of tilted double wells can be interpreted using a Heisenberg model. First let's analyze the case of moderate tilt (figure 5.4 (j)-(m),$\Delta = 0.5\hbar\omega_y$). The formation of the UCWM results in a system that is well described by a 3-site Heisenberg triangle Hamiltonian

$$H_{Heis}^{trg} = J_{12}\boldsymbol{S_1}\cdot\boldsymbol{S_2} + J_{13}(\boldsymbol{S_1}\cdot\boldsymbol{S_3} + \boldsymbol{S_2}\cdot\boldsymbol{S_3}) - J_{12}/4 - J_{13}/2, \tag{5.2}$$

In analogy to section 5.1 we label $s = J_{12}$ (tunneling between repulsively created sites within a single well) and $r = J_{13} = J_{23}$ (tunneling across the barrier). For the site numbering see figure 5.4 (V), for details on the Heisenberg model and how to solve it, see chapter 2 section 3.4.

The CI energy spectrum in figure 5.4 (j) shows a characteristic 1-2 degeneracy pattern at strong repulsion ($-1/g \to 0$) and the multiplicities $\mathcal{G}$ of the total spin S are $\mathcal{G}(N = 3, S =$

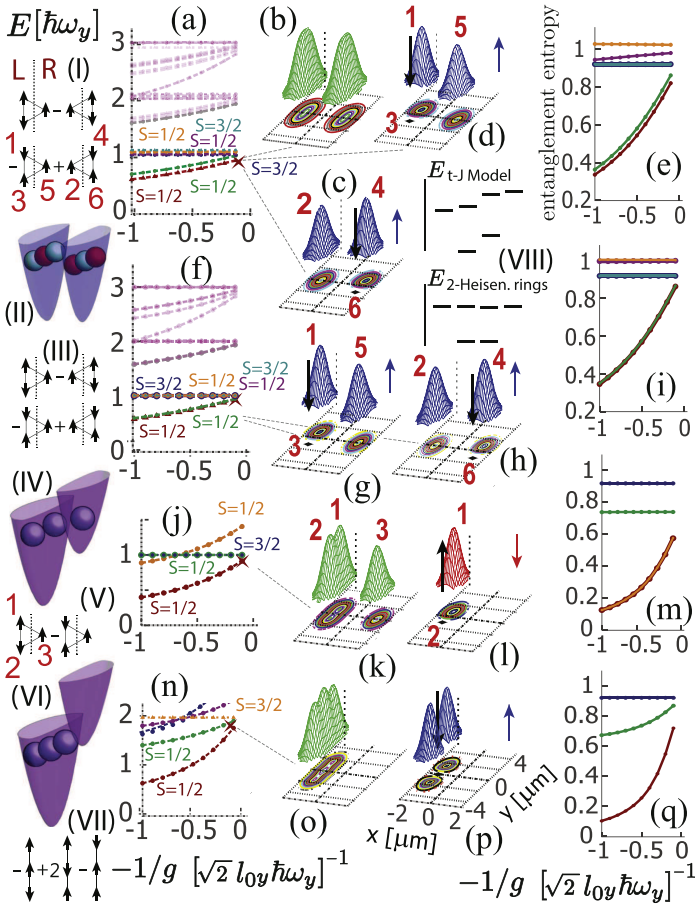

Figure 5.4: Spectra, entanglement, SPDs and SR-CPDs for three particles in a parallel double well. The trapping frequencies are $\omega_x/(2\pi) = 6.6\,\text{kHz}, \omega_y/(2\pi) = 1\,\text{kHz}$, the well separation is $d = 2.5\,\mu\text{m}$. Panels (a),(b),(c),(d),(e) were calculated using $\Delta/h = 0, V_b/h = 11.14\,\text{kHz}$, panels (f),(g),(h),(i) were calculated using $\Delta/h = 0, V_b/h = 24.30\,\text{kHz}$, panels (j),(k),(l),(m) were calculated using $\Delta/h = 0.5\,\text{kHz}, V_b/h = 24.30\,\text{kHz}$, panels (n),(o),(p),(q) were calculated using $\Delta/h = 2.5\,\text{kHz}, V_b/h = 24.30\,\text{kHz}$. The left column of panels (a),(f),(j),(n) show the spectra as a function of $-1/g$, the right column of panels (e),(i),(m),(q) show the von Neumann entanglement entropy as a function of $-1/g$. The middle column of panels (b),(c),(d),(g),(h),(k),(l),(o),(p) shows SPDs and SR-CPDs for the ground state at $-1/g = -0.1(\sqrt{2}l_{0y}\hbar\omega_y)^{-1}$. Dashed lines are used to indicate which densities belong to which spectrum and a star indicates the state for which the densities were calculated. Green surfaces indicate SPDs, blue surfaces show spin up SR-CPDs, red surfaces show spin down SR-CPDs. The panels with roman numerals are schematics, panels (II),(IV),(VI) show the external potential and the distribution of particles in the ground state (not to scale). Panels (I),(III),(V),(VII) show the spin function of the ground state and panel (VIII) shows the difference in energy levels between the t-J and Heisenberg model.

$1/2) = 2$ and $\mathcal{G}(N = 3, S = 3/2) = 1$ in agreement with the results from the three site Heisenberg model and the branching diagram (for a description of the branching diagram see section A.2). In addition to the spectrum we can also compare our CI wavefunction with the eigenfunctions of the Heisenberg model using our SR-CPDs. The results of the CI calculation and the Heisenberg model are again in very good agreement. A detailed compariosn can be found in our published paper [121].

The case of the strong tilt ($\Delta = 2.5\hbar\omega_y$, figure 5.4 (VI)) can be well described by a 3-site linear (open) Heisenberg Hamiltonian, which can be obtained from the Hamiltonian in equation (5.2) by setting $J_{12} = s = 0$. The energy spectrum at strong repulsion of this Hamiltonian consists of three distinct energy levels $E_1 = -3r/2, E_2 = -r/2, E_3 = 0$, whose energy spacing is in agreement with our CI energy levels (see figure 5.4 (n)). In addition we can again compare the eigenfunctions of the Heisenberg model with our CI solutions and the agreement is excellent. For details and more information see our published paper [121].

A qualitatively different behavior is exhibited in the non-tilted ($\Delta = 0$) DWPA case shown in (figure 5.4 (a)-(i), (I)-(III)). Contrary to the three state lowest energy band present in the tilted DWPA at strong repulsion, the non-tilted system shows a six state lowest energy band with four $S = 1/2$ and two $S = 3/2$ states. This doubling of energy levels is due to parity conservation, which requires consideration of a second triangle (246) in addition to the (135) triangle, see schematic figure 5.4 (I). As can be seen by the SR-CPDs in panel (b),(c),(d),(g),(h) of figure 5.4 the two triangles consist of well localized atoms. One may view this situation as having six available sites (three in each well), with three particles and three holes. However not all holes can be independently occupied, the particles are in a superposition of the aforementioned triangles. Such a behavior can be modeled by a t-J like Hamiltonian.

$$H_{tJ} = H^{trg}_{Heis}(135)(J) + H^{trg}_{Heis}(246)(J) + H_c(t), \tag{5.3}$$

where H^{trg}_{Heis} are the Heisenberg ring Hamiltonians for the individual triangles and H_c is the coupling between the two. Using $|1\rangle = |\alpha,0,\alpha,0,\beta,0\rangle$, $|2\rangle = |\alpha,0,\beta,0,\alpha,0\rangle$, $|3\rangle = |\beta,0,\alpha,0,\alpha,0\rangle$, $|4\rangle = |0,\beta,0,\alpha,0,\alpha\rangle$, $|5\rangle = |0,\alpha,0,\alpha,0,\beta\rangle$, $|6\rangle = |0,\alpha,0,\beta,0,\alpha\rangle$ as a basis this Hamiltonian can be written as a six by six matrix

$$H_{tJ} = \left(\begin{array}{ccc|ccc} -J_{15}-\frac{\Delta}{2} & \frac{J_{15}}{2} & \frac{J_{15}}{2} & t_2 & t & t \\ \frac{J_{15}}{2} & -\frac{J_{13}}{2}-\frac{J_{15}}{2}-\frac{\Delta}{2} & \frac{J_{13}}{2} & t & t & t_2 \\ \frac{J_{15}}{2} & \frac{J_{13}}{2} & -\frac{J_{13}}{2}-\frac{J_{15}}{2}-\frac{\Delta}{2} & t & t_2 & t \\ \hline t_2 & t & t & -J_{24}+\frac{\Delta}{2} & \frac{J_{24}}{2} & \frac{J_{24}}{2} \\ t & t & t_2 & \frac{J_{24}}{2} & -\frac{J_{46}}{2}-\frac{J_{24}}{2}+\frac{\Delta}{2} & \frac{J_{46}}{2} \\ t & t_2 & t & \frac{J_{24}}{2} & \frac{J_{46}}{2} & -\frac{J_{46}}{2}-\frac{J_{24}}{2}+\frac{\Delta}{2} \end{array}\right), \tag{5.4}$$

where $t = \langle\alpha,0,\alpha,0,\beta,0|H_c|0,\alpha,0,\alpha,0,\beta\rangle = \langle\alpha,0,\alpha,0,\beta,0|H_c|0,\alpha,0,\beta,0,\alpha\rangle$ and $t_2 = \langle\alpha,0,\alpha,0,\beta,0|H_c|0,\beta,0,\alpha,0,\alpha\rangle$.

The numbering of the sites and the coupling parameters are in detail illustrated in figure 5.5 and the site numbers are also indicated in several panels in figure 5.4. The numbers 1-3-5 denote one triangle while 2-3-6 denote the other. For $r = 0$ and $t_2 = t = 0$ (the case of high interwell barrier, see figure 5.4(f)) the Hamiltonian H_{tJ} reproduces the the 4-2 degeneracy pattern. It is remarkable that the complicated non-degenerate spectrum of figure 5.4(a) can be reproduced by setting $t_2 \approx -4t/10 > -1/2$ with $t < 0$ and $s > |t|$. The energy gap between the two lowest states is then $\Delta\mathcal{E}_{12} = \mathcal{E}_1 - \mathcal{E}_2 = 14t/5$, centered around $-s$. The remaining energies group together in a fourfold band centered around 0. The energy gap between the outer members of the fourfold band (both $S = 3/2$) is

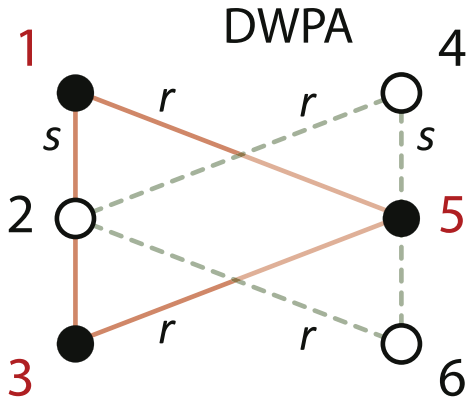

Figure 5.5: Three particle site numbering for a double well parallel (DWPA) configuration. **Important:** The six sites are a result of having two three-site interlocking triangles. The eigenstates of this system are in a superposition of these triangles. This implies that interaction is only present for sites within a triangle. **There is no interaction between sites with different colored dot**. Parameters r, s represent the different couplings between the localized sites. The interaction between site 1 and 3 is between self localized sites and denoted s. The interaction between site 1 and 5 and between site 3 and 5 is through the interwell barrier and denoted r. The same notation convention is applied to triangle 2,4,6.

$\Delta\mathcal{E}_{56} = \mathcal{E}_5 - \mathcal{E}_6 = 16t/5$ similar to the $\Delta\mathcal{E}_{12}$ gap in agreement with the spectrum in figure 5.4(a). Furthermore the energy gap between the two higher and lower energies of this band $\Delta\mathcal{E}_{35} = \Delta\mathcal{E}_{46} = \mathcal{E}_4 - \mathcal{E}_6 = t/5$ which is much smaller than $\Delta\mathcal{E}_{56}$ again in agreement with figure 5.4(a). Note however that for $t_2 = -t/2$ it follows that $\Delta\mathcal{E}_{35} = \Delta\mathcal{E}_{46} = 0$ and a degeneracy pattern 1-1-2-2 develops in disagreement with the CI spectrum, highlighting the importance of the right choice of parameters.

5.2.2 Three particles in a linear double well (DWLI)

Figure 5.6 shows spectra, SPD and SR-CPDs for the ground state of three particles in linear double well (DWLI). The results are very similar to the results of the DWPA system studied in section 5.2.1. The spectra show the same degeneracy pattern and the SPD and SR-CPDs indicate the formation of Wigner molecules and resonating triangles. Analogous to the DWPA system this can be modeled using a $t - J$ model, similar to the one shown in equation (5.4). The difference compared to equation (5.4) is that tunneling across the middle well only takes place between site 3 and 5 (in the 1,3,5 triangle) and 2 and 4 (in the

2,4,6 triangle). The site numbering is shown in figure 5.7.

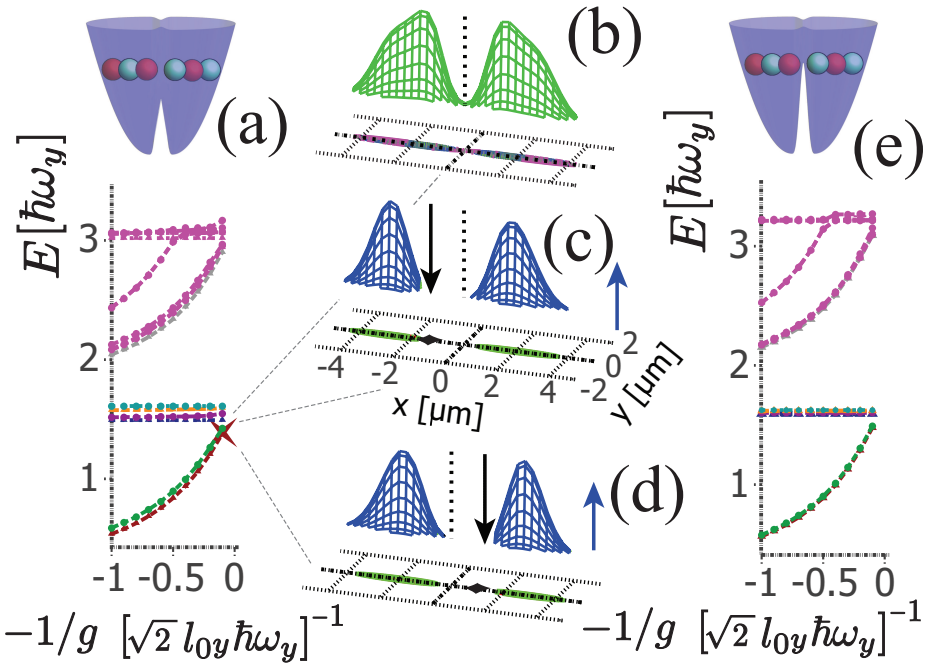

Figure 5.6: Spectra, SPD and two SR-CPDs for three particles in a linear double well. The schematics in panel (a) and (e) contain different colored balls to symbolize the two resonating three particle configurations, namely $|2,1\rangle \pm |1,2\rangle$. The spectrum in panel (a), the corresponding ground state SPD (panel (b)) and the two ground state SR-CPDs (panels (c) and (d)) were calculated using $\omega_x/(2\pi) = 1\,\mathrm{kHz}, \omega_y/(2\pi) = 100\,\mathrm{kHz}, d = 2.5\,\mu\mathrm{m}, V_b = 6.08\,\mathrm{kHz}$. The high-interwell spectrum in panel (e) was calculated with the parameters $\omega_x/(2\pi) = 1\,\mathrm{kHz}, \omega_y/(2\pi) = 100\,\mathrm{kHz}, d = 2.5\,\mu\mathrm{m}, V_b = 11.14\,\mathrm{kHz}$. The calculation was run using two spin up and one spin down particle ($S_z = 1/2$). The ground state (brown curve) in the spectrum has a total spin quantum number $S = 1/2$. A star in the spectrum indicates the interaction strength for which the SPDs and SR-CPDs were calculated. The position of the fixed point for the SR-CPDs in panel (c) and (d) is at $r_0 = (-1.3\,\mu\mathrm{m}, 0)$ and $r_0 = (1.3\,\mu\mathrm{m}, 0)$ respectively. The spectrum in panel (a) shows the onset of the characteristic 4-2 degeneracy pattern, in panel (e) the degeneracies are fully developed. The spectra were plotted such that the non-interacting energy is at 0.

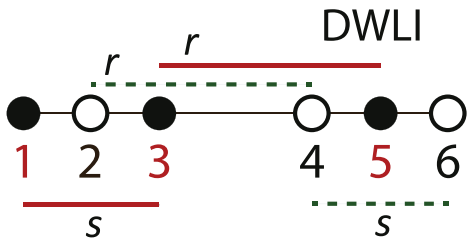

Figure 5.7: Three particle site numbering for a double well linear (DWLI) configuration. **Important:** The six sites are a result of having two three-site interlocking chains. The eigenstates of this system are in a superposition of these chains. This implies that interaction is only present for sites within a chain. **There is no interaction between sites with different colored dots.** In the figure r, s represent the different couplings between the localized sites. The interaction between site 1 and 3 is between self localized sites and denoted s. The interaction between site site 3 and 5 is through the interwell barrier and denoated r. The same notational convention is applied to chain 2,4,6 respectively.

More information on the t-J model, a detailed discussion of the spin states and a more detailed description of the tilted three particle systems can be found in our paper [121]:

Constantine Yannouleas, Benedikt B Brandt, and Uzi Landman. "Ultracold few fermionic atoms in needle-shaped double wells: spin chains and resonating spin clusters from microscopic Hamiltonians emulated via antiferromagnetic Heisenberg and t-J models". In: *New Journal of Physics* 18.7 (July 8, 2016)

CHAPTER 6

STUDY OF ULTRACOLD ATOMS IN OPTICAL PLAQUETTES - BUILDING BLOCKS OF UNCONVENTIONAL SUPERCONDUCTIVITY

A single plaquette is believed to be a building block in the study of high T_c superconductivity. It has been extensively analyzed using spin models and it is known that those spin models exhibit a pairing energy gap [160] for different hole dopings and that the ground state in these models is the celebrated resonating valence bond (RVB) [180] state. However experimentally important microscopic calculations, analyzing different microscopic barriers and symmetry braking deformations have so far been lacking.

In this chapter, which is based on our publication [122], we investigate the applicability of the $t - J$ model and the Hubbard model using our full CI methodology. We reproduce the predicted formation of a pairing gap for a single plaquette and study the influence of the inter-well barrier on the pairing gap formation. We then proceed to study the double plaquette system, which allows for the direct observation of the predicted pairing gap. We furthermore analyze the impact of symmetry braking (through tuning and deformations) on the pairing gap.

In section 6.1 we introduce the single plaquette system and show results for four particles in a single plaquette. In section 6.2 we are introducing the resonating valence bond states, in section 6.3 we outline our methodology of how to derive spin function solutions from our CI solutions. In section 6.4 we study the pairing gap phase diagram of a single plaquette. In section 6.5 we present an analysis of the double plaquette system and how the result for a double plaquette connects with the results of a single plaquette.

> *Technical details:*

The following paragraphs provide technical details about the calculation and are not needed to follow the arguments in the text. They can be skipped until the details become relevant to the reader.

Since we are studying a truly two dimensional system in this chapter, we are using a short range Gaussian interaction (see equation (2.4) in chapter 2). We use λ to denote the interaction strength in order to clearly distinguish it from the one dimensional contact interaction g used in chapter 4 and chapter 5.

6.1 Four particles in a single plaquette - introductory analysis

In this section we want to analyze and compare our CI solutions for four particles in a single plaquette with well separated sites to the results from the Heisenberg and Hubbard model. For very strong repulsion double occupancy is suppressed and the CI results should agree with the Heisenberg model. For intermediate repulsion strengths double occupancy is not completely suppressed and we need to compare our CI results to the Hubbard model. The results from our CI calculation are displayed in figure 6.1. For large repulsion ($\lambda > 0.5\ l_0^2\hbar\omega$) the spectrum shows a clear separation into a lowest band consisting of six states and levels that are rising above it. The rising levels represent states with a contribution due to double occupancy which makes them strongly sensitive to the repulsion strength. The lowest six states in contrast are states where the double occupancy is suppressed. The number of states and their total spin corresponds to what one would expect based of the branching diagram (see appendix section A.2) which is a further indication that the Heisenberg model might be applicable.

6.1.1 Heisenberg model

For well separated sites (i.e. at large intra-plaquette distances or high barriers) and at very strong repulsion double occupancy within each site is suppressed. The microscopic single

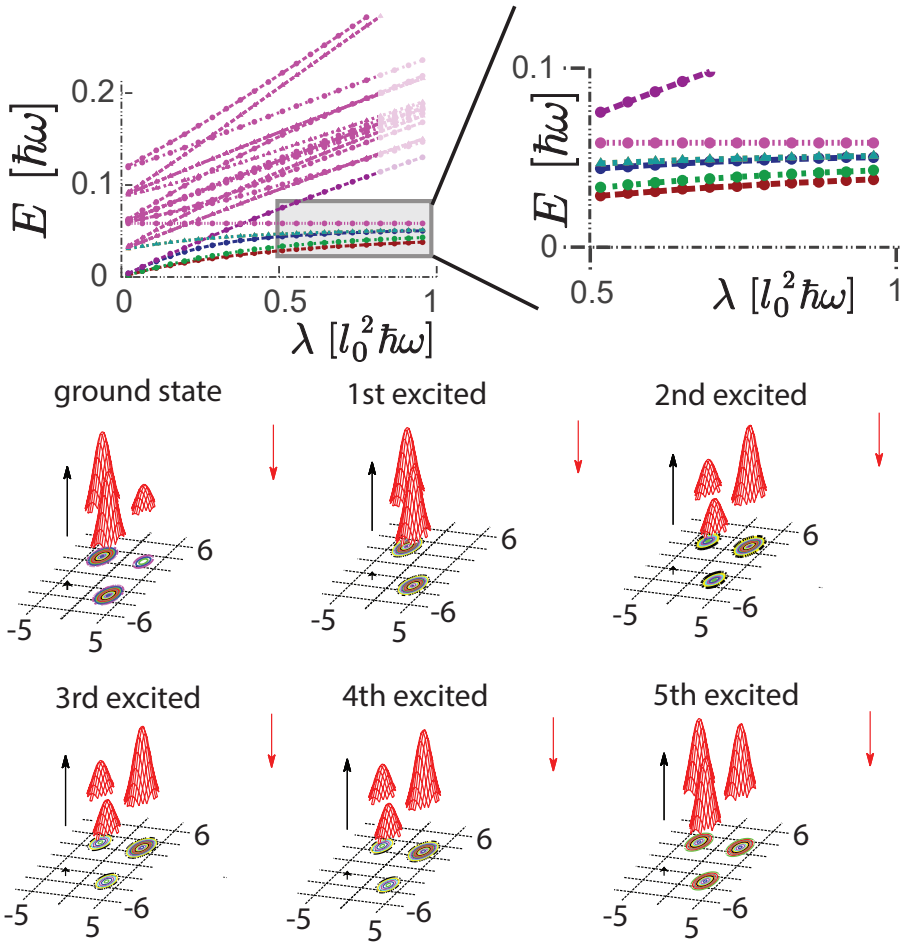

Figure 6.1: Spectra and SR-CPDs for four particles in a single plaquette. The top row shows the spectrum from our CI calculation in a range from $\lambda = 0$ to $\lambda = 1$ $l_0^2\hbar\omega$ and a zoomed in region from $\lambda = 0.5$ $l_0^2\hbar\omega$ to $\lambda = 1$ $l_0^2\hbar\omega$, where the lowest energy band is clearly distinct from the higher lying states. This band consists of 6 states, the ground state with parity $P_{xy} = 1$ and total spin $S = 0$, the 1st excited state with $P_{xy} = 1$ and $S = 1$, the second excited state with $P_{xy} = 1$ and $S = 0$, the third and fourth excited state which are degenerate and share the same quantum numbers $P_{xy} = -1$ and $S = 1$ and the fifth excited state with quantum numbers $P_{xy} = -1$ and $S = 2$. The next two rows show the SR-CPDs for those six states, where we fix a spin up particle at $x = -3\,\mu\text{m}, y = -3\,\mu\text{m}$ and look for a spin down particle on the remaining sites. The parameters for our plaquette are $d = 3\,\mu\text{m}$, $\epsilon_b = 0.5$, $\omega_x/(2\pi) = 1\,\text{kHz}$, $\omega_y/(2\pi) = 1\,\text{kHz}$. The SR-CPDs were calculated at a value of $\lambda = 1.1$ $l_0^2\hbar\omega$ corresponding to a value of $U/t = 9.1$. For details on how we map the CI parameters to Hubbard model parameters see appendix section A.1.

plaquette Hamiltonian with four particles should therefore map onto a four site square Heisenberg model. The solutions for this model are given in [132] and reproduced here for the reader's convenience

$$E_1 = -2J, \tag{6.1}$$

$$E_2 = -J, \tag{6.2}$$

$$E_3 = 0, \tag{6.3}$$

$$E_4 = 0, \tag{6.4}$$

$$E_5 = 0, \tag{6.5}$$

$$E_6 = 2J, \tag{6.6}$$

with corresponding (unnormalized) eigenvectors

$$V_1 = |\uparrow\uparrow\downarrow\downarrow\rangle - 2\,|\uparrow\downarrow\uparrow\downarrow\rangle + |\uparrow\downarrow\downarrow\uparrow\rangle + |\downarrow\uparrow\uparrow\downarrow\rangle - 2\,|\downarrow\uparrow\downarrow\uparrow\rangle + |\downarrow\downarrow\uparrow\uparrow\rangle \quad S = 0, \tag{6.7}$$

$$V_2 = -\,|\uparrow\downarrow\uparrow\downarrow\rangle + |\downarrow\uparrow\downarrow\uparrow\rangle \quad S = 1, \tag{6.8}$$

$$V_3 = |\uparrow\uparrow\downarrow\downarrow\rangle - |\uparrow\downarrow\downarrow\uparrow\rangle - |\downarrow\uparrow\uparrow\downarrow\rangle + |\downarrow\downarrow\uparrow\uparrow\rangle \quad S = 0, \tag{6.9}$$

$$V_4 = |\uparrow\uparrow\downarrow\downarrow\rangle - |\downarrow\downarrow\uparrow\uparrow\rangle - i\,|\uparrow\downarrow\downarrow\uparrow\rangle + i\,|\downarrow\uparrow\uparrow\downarrow\rangle \quad S = 1, \tag{6.10}$$

$$V_5 = |\uparrow\uparrow\downarrow\downarrow\rangle - |\downarrow\downarrow\uparrow\uparrow\rangle + i\,|\uparrow\downarrow\downarrow\uparrow\rangle - i\,|\downarrow\uparrow\uparrow\downarrow\rangle \quad S = 1, \tag{6.11}$$

$$V_6 = |\uparrow\uparrow\downarrow\downarrow\rangle + |\uparrow\downarrow\uparrow\downarrow\rangle + |\uparrow\downarrow\downarrow\uparrow\rangle + |\downarrow\uparrow\uparrow\downarrow\rangle + |\downarrow\uparrow\downarrow\uparrow\rangle + |\downarrow\downarrow\uparrow\uparrow\rangle \quad S = 2, \tag{6.12}$$

where we give the value of the total spin S after the spin function. Since our plaquette exhibits C-4 symmetry one must be careful to ensure that all eigenvectors are C-4 symmetric. This is automatically guaranteed for non-degenerate states, but needs to be enforced in the degenerate space for eigenvalues 4 and 5. The eigenvectors in equation (6.7) to equation (6.12) were chosen to exhibit the proper C-4 symmetry.

The SR-CPDs can be employed to compare the CI-wavefunctions with the spin eigenfunctions. This procedure has been extensively described in [132]. Fixing a spin up atom

on position 1 of eigenvector 1 for instance leads to an expected ratio of $5/2$ between the volume of the hump on site 2 vs the volume of the hump on site 3 for the ground state (see equation (6.7)). The predictions for the volume ratio between site 2 and site 3 from the Heisenberg model and the actual CI volumes are listed in table 6.1.

Table 6.1: Volume ratios of the humps at site 2 and site 3 in the CI calculation and the predictions from the Heisenberg model. The SR-CPDs are displayed in figure 6.1 and the Heisenberg eigenvectors are listed in equation (6.7) to equation (6.12).

	gs	1st ex.	2nd ex.	3rd ex.	4th ex.	5th ex.
CI ratio site 2 / site 3	2.26	18.27	0.52	0.51	0.51	0.997
Heisenberg ratio site 2 / site 3	2.5	Inf	0.5	0.5	0.5	1

The overall agreement, especially for the excited states is very good. The ground state volume ratio is within 10% of the Heisenberg volume ratio and could be further improved by even stronger interactions.

6.1.2 Hubbard model

Instead of comparing with the Heisenberg model, which is only valid for very strong repulsion, a more accurate comparison can be made when comparing with the Hubbard model. The Hubbard model allows for double occupancy and is therefore valid even for small U (as long as the inter-plaquette distance (barrier) is large so that the plaquette sites are well separated). For details on how we determine the Hubbard model parameters from our CI calculation see section A.1 in the appendix.

Solutions for the Hubbard model in a plaquette can be found in the literature in a paper by Schumann [166, 196]. The lowest band of six states in the CI calculation (in order of ascending energy) corresponds to the Schumann eigenstates $\Psi_{111}, \Psi_{128}, \Psi_{119}, \Psi_{123}, \Psi_{125}, \Psi_{130}$. Alternatively the Hubbard model solutions can also be calculated using SNEG (see chapter 3 section 3.1.1). The expressions for the Hubbard model eigenfunctions are very long and therefore not reproduced here, but they can be readily found i.e. in [196]. The volume ratios obtained from those eigenfunctions at a value of $U/t = 9.1$ (corresponding to a value

of $\lambda = 1.1\ l_0^2\hbar\omega$) are listed in table 6.2.

Table 6.2: Volume ratios of the humps at site 2 and site 3 in the CI calculation and the predictions from the Hubbard model at $U/t = 9.1$ (corresponding to a value of $\lambda = 1.1\ l_0^2\hbar\omega$). The SR-CPDs are displayed in figure 6.1.

	gs	1st ex.	2nd ex.	3rd ex.	4th ex.	5th ex.
CI ratio site 2 / site 3	2.26	18.27	0.52	0.51	0.51	0.997
Hubbard ratio site 2 / site 3	2.28	20.46	0.51	0.51	0.51	1

They agree very well with the observed CI volume ratios and the ratios for the ground state and the 1st excited state are significantly improved compared to the Heisenberg calculations shown in table 6.1.

Furthermore one can compare the Hubbard model spectrum to the spectrum obtained through the CI calculations. The two spectra are shown in figure 6.2 and are in good agreement.

6.1.3 Convergence of the CI calculations

For the calculations in chapter 4 and chapter 5 convergence of the full CI method was easily achieved since those calculations were quasi one dimensional and a large number of single particle basis functions (> 100) can be chosen to represent the states along the 1D axis. Plaquette calculations however are more difficult due to their 2D nature. E.g. 10 basis functions in x and y combine to form 100 possible basis functions in x, y space and convergence of the calculation therefore needs to be carefully checked.

Figure 6.3 shows the convergence of the CI calculation as a function of two dimensional (x, y space) single particle basis functions. This calculation was done for three particles in a single plaquette and we have checked that the convergence for two and four particles in a single plaquette is similar. The energy scale in figure 6.3 is given in units of $t = 0.0145\hbar\omega$. It is remarkable that the convergence is rapid and very good (up to the third decimal point in units of $\hbar\omega$) already for a small number of basis functions. The reason for this turns out to be in the similarity between the single particle basis functions and the natural orbitals. As

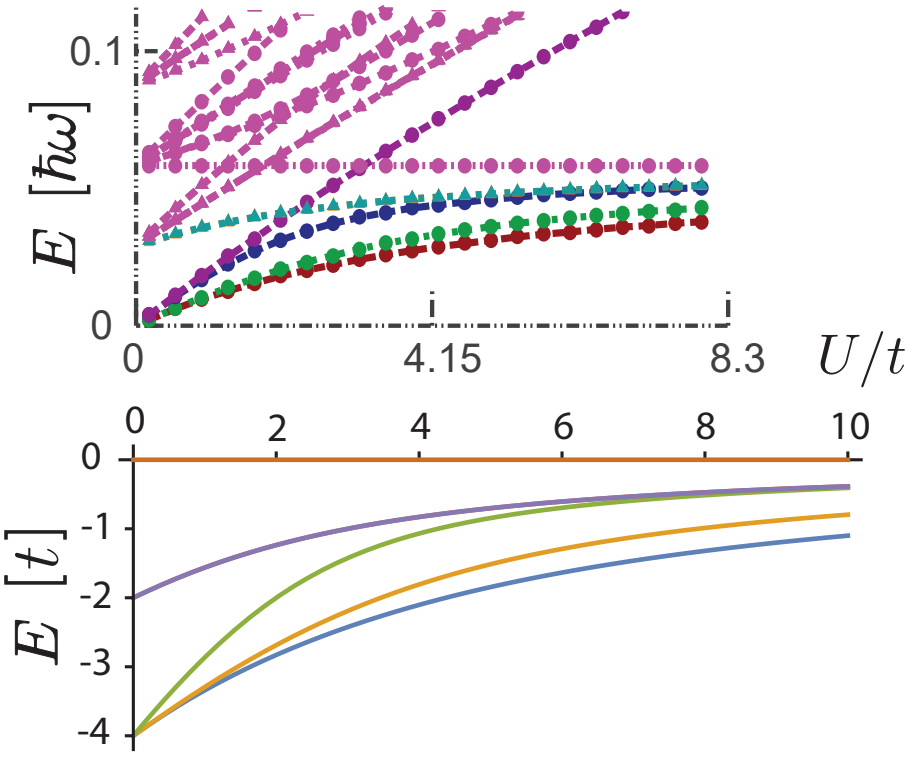

Figure 6.2: Spectrum obtained through the CI calculation and Hubbard model spectrum for four particles in a single plaquette. The spectrum on top is obtained from the CI calculations, the spectrum on the bottom is obtained through the Hubbard model. The CI spectrum for small U contains several excited states that have double occupancy components (they depend strongly on the inter-particle repulsion U). For large U the CI spectrum shows a clear separation into a lowest energy band of six states separated from the higher excited states (only five states are distinctly visible since the third excited state is doubly degenerate). Those six states correspond to the six states plotted in the spectrum below which was obtained from the eigenenergies of the Hubbard model (again the third excited state is two-fold degenerate). The behavior of the states and their energy level pattern is in good agreement with that from the CI calculation. Note: The colors in the spectrum are only a visual aid and there is no correspondence between states and color in the two spectra.

discussed in section 2.7.5 the natural orbitals are the set of single particle basis functions for which the most rapid convergence of the CI calculation can be achieved. Figure 6.4 compares the first 3 natural orbitals and the single particle basis functions for the ground state at an interaction of $U/t = 2.77$. Both the single particle basis functions and the the natural orbitals are very similar, which indicates that the single particle basis functions are already well adapted to the calculation. This is true for all the energy levels in the lowest energy band in the single plaquette.

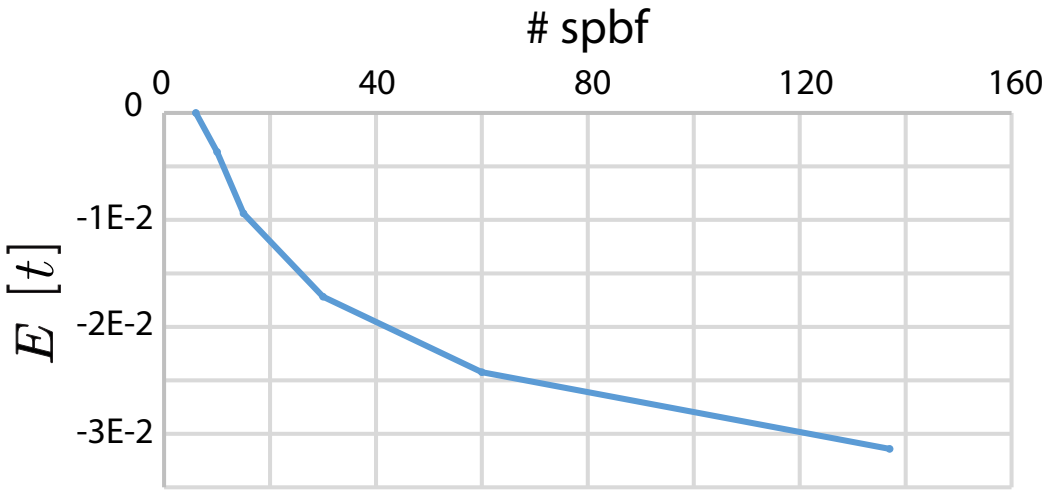

Figure 6.3: Convergence of the ground state energy for three particles in a single plaquette vs the number of two dimensional (x, y space) single particle basis functions (spbf) at $U/t = 2.77$. The energy for 6 spbf (first data point) is set to be 0 and the energy axis is plotted in units of t. The tunneling parameter t in our plaquette equals $0.0145\hbar\omega$. One can see that the convergence is very rapid with respect to the energy scales in our plaquette. Given that the plotted energy E is in units of t the change in energy between 6 spbf and 120 spbf is $0.03t = 0.0004\hbar\omega$. In other words even for 6 spbf the energy is already precise up to the 3rd decimal point in units of $\hbar\omega$. The reason for this remarkable accuracy is in the similarity of the spbf and natural orbitals, which is shown in figure 6.4. The parameters for our plaquette are $d = 3\,\mu\text{m}$, $\epsilon_b = 0.5$, $\omega_x/(2\pi) = 1\,\text{kHz}$, $\omega_y/(2\pi) = 1\,\text{kHz}$.

6.2 Resonating valence bond states (RVB)

As mentioned in the introduction to this chapter, the key to understanding a plaquette system is the understanding of the resonating valence bond (RVB) states. The RVB states ap-

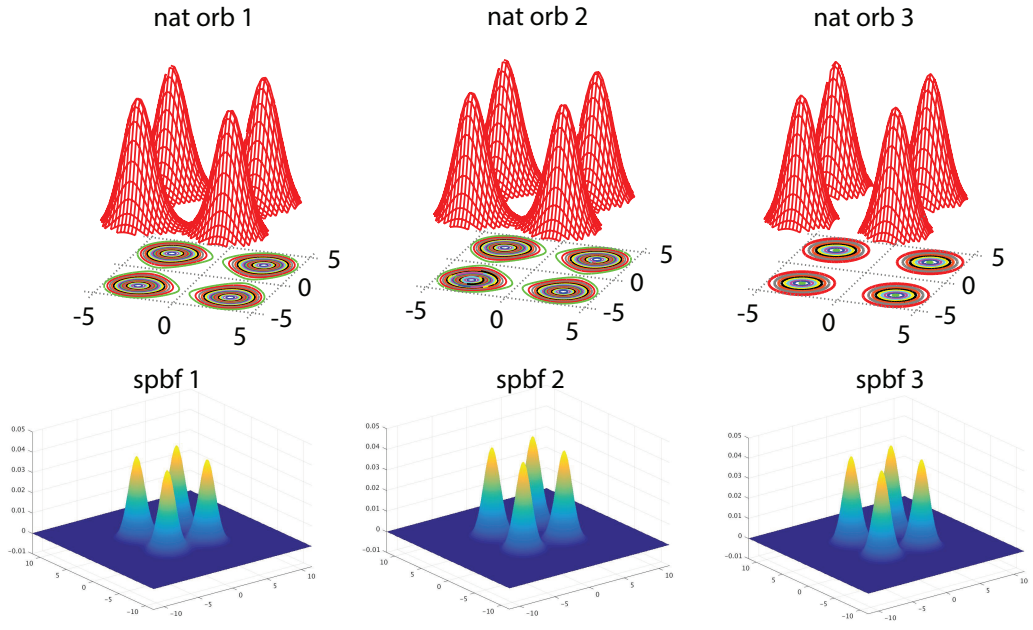

Figure 6.4: Density of the first three natural orbitals (first row, labeled as "nat orb") for the ground state and density of first three single particle basis functions (second row, labeled as "spbf") for a single plaquette. The natural orbitals are very similar to the single particle basis functions. This shows that the single particle basis is well adapted to the calculation and that only few single particle basis functions will be needed to achieve convergence with respect to the relevant energy scales in our plaquette. The parameters for our plaquette are $d = 3\,\mu\text{m}$, $\epsilon_b = 0.5$, $\omega_x/(2\pi) = 1\,\text{kHz}$, $\omega_y/(2\pi) = 1\,\text{kHz}$.

pear as the ground state of a square (four site) Heisenberg lattice with identical couplings J,

$$H = J(\boldsymbol{S}_1 \cdot \boldsymbol{S}_2 + \boldsymbol{S_3} \cdot \boldsymbol{S_4} + \boldsymbol{S_4} \cdot \boldsymbol{S_1} + \boldsymbol{S_2} \cdot \boldsymbol{S_3}), \tag{6.13}$$

where $\boldsymbol{S}_i$ is the spin operator for site i. For more details on the Heisenberg Hamiltonian and how to calculate its eigenstates see section 3.4. The ground state solution for repulsive interaction is given by

$$\begin{aligned}\chi_{gs} = \frac{1}{2\sqrt{3}}\left|\uparrow\uparrow\downarrow\downarrow\right\rangle - \frac{1}{\sqrt{3}}\left|\uparrow\downarrow\uparrow\downarrow\right\rangle + \frac{1}{2\sqrt{3}}\left|\uparrow\downarrow\downarrow\uparrow\right\rangle + \frac{1}{2\sqrt{3}}\left|\downarrow\uparrow\uparrow\downarrow\right\rangle \\ - \frac{1}{\sqrt{3}}\left|\downarrow\uparrow\downarrow\uparrow\right\rangle + \frac{1}{2\sqrt{3}}\left|\downarrow\downarrow\uparrow\uparrow\right\rangle,\end{aligned} \tag{6.14}$$

which is a well known RVB state [197, 198]. Its quantum numbers are $S = 0, S_z = 0$. The reason it is called a resonating valence bond (RVB) state is that it can be written as a superposition of degenerate valence bond singlets. This can be seen as follows (using a clockwise enumeration of the lattice sites in the plaquette):

$$\chi_{12\&34\text{ singlet}} = \frac{1}{\sqrt{2}}(|\uparrow\downarrow 00\rangle - |\downarrow\uparrow 00\rangle) \otimes \frac{1}{\sqrt{2}}(|00\uparrow\downarrow\rangle - |00\downarrow\uparrow\rangle) \tag{6.15}$$

$$= \frac{1}{2}(|\uparrow\downarrow\uparrow\downarrow\rangle - |\downarrow\uparrow\uparrow\downarrow\rangle - |\uparrow\downarrow\downarrow\uparrow\rangle + |\downarrow\uparrow\downarrow\uparrow\rangle), \tag{6.16}$$

$$\chi_{23\&41\text{ singlet}} = \frac{1}{\sqrt{2}}(|0\uparrow\downarrow 0\rangle - |0\downarrow\uparrow 0\rangle) \otimes \frac{1}{\sqrt{2}}(|\uparrow 00\downarrow\rangle - |\downarrow 00\uparrow\rangle) \tag{6.17}$$

$$= \frac{1}{2}(|\uparrow\uparrow\downarrow\downarrow\rangle - |\uparrow\downarrow\uparrow\downarrow\rangle - |\downarrow\uparrow\downarrow\uparrow\rangle + |\downarrow\downarrow\uparrow\uparrow\rangle), \tag{6.18}$$

$$\chi_{gs} = \frac{1}{\sqrt{3}}(\chi_{12\&34\text{ singlet}} - \chi_{23\&41\text{ singlet}}). \tag{6.19}$$

In this thesis and our publication [122] we follow the nomenclature from [199] and call the ground state d-wave symmetric. Up to today there is some ambiguity in literature over the correct terminology for this state, which arises due to the small system size. In [199] the authors refer to the four particle ground state as d-wave symmetric, while in [96] the

authors refer to the ground state as an s-wave RVB state (Note: When comparing with [96] it is important to take into account that negative values for J in [96] correspond to repulsive interactions). Another RVB state can be formed by

$$\chi_{ex} = \chi_{12\&34 \text{ singlet}} + \chi_{23\&41 \text{ singlet}}, \tag{6.20}$$

$$= \frac{1}{2}\left(|\uparrow\uparrow\downarrow\downarrow\rangle + |\downarrow\downarrow\uparrow\uparrow\rangle - |\downarrow\uparrow\uparrow\downarrow\rangle - |\uparrow\downarrow\downarrow\uparrow\rangle\right). \tag{6.21}$$

This superposition exhibits s-wave symmetry [199] and is the first excited $S = 0, S_z = 0$ state. It is worth noting that the state χ_{ex} can also be written as a tensor product using singlets along the diagonal:

$$\chi_{ex} = \frac{1}{\sqrt{2}}(|\uparrow 0 \downarrow 0\rangle - |\downarrow 0 \uparrow 0\rangle) \otimes \frac{1}{\sqrt{2}}(|0 \uparrow 0 \downarrow\rangle - |0 \downarrow 0 \uparrow\rangle). \tag{6.22}$$

For more details on d-wave and s-wave RVB states in plaquettes see [96, 199–201].

6.3 Determination of spin functions - RVB state in a plaquette

In order to study this system with our CI methodology and to connect our studies to the already existing literature, it is essential to develop a technique that allows us to identify the RVB state in our microscopic solution. In this section we are going to provide a description of the procedure used to identify the d-wave RVB state using our spin resolved CPDs.

As first described in [132] one can map SR-CPDs to spin functions by analyzing the volumes underneath the SR-CPDs and the versatility of this method has been demonstrated several times [121, 132]. The starting point is the general spin function for four spin $1/2$

fermions with quantum numbers $S = 0, S_z = 0$, which is given as [132]:

$$\begin{aligned}\chi_{00} =&\sqrt{\frac{1}{3}}\sin\theta\,|\uparrow\uparrow\downarrow\downarrow\rangle + \left(\frac{1}{2}\cos\theta - \sqrt{\frac{1}{12}}\sin\theta\right)|\uparrow\downarrow\uparrow\downarrow\rangle \\ &+ \left(\frac{1}{2}\cos\theta + \sqrt{\frac{1}{12}}\sin\theta\right)|\uparrow\downarrow\downarrow\uparrow\rangle - \left(\frac{1}{2}\cos\theta + \sqrt{\frac{1}{12}}\sin\theta\right)|\downarrow\uparrow\uparrow\downarrow\rangle \\ &+ \left(\frac{1}{2}\cos\theta - \sqrt{\frac{1}{12}\sin\theta}\right)|\downarrow\uparrow\downarrow\uparrow\rangle + \sqrt{\frac{1}{3}}\sin\theta\,|\downarrow\downarrow\uparrow\uparrow\rangle\,,\end{aligned} \tag{6.23}$$

From the general spin function one can read off the spin components contributing to a specific SR-CPD. For instance the spin components contributing to the conditional probability density for a SR-CPD where one fixes a spin-up fermion on position 1 and looks for a spin-down fermion are:

$$\sqrt{\frac{1}{3}}\sin\theta\,|\uparrow\uparrow\downarrow\downarrow\rangle \tag{6.24}$$

$$\left(\frac{1}{2}\cos\theta - \sqrt{\frac{1}{12}}\sin\theta\right)|\uparrow\downarrow\uparrow\downarrow\rangle \tag{6.25}$$

$$\left(\frac{1}{2}\cos\theta + \sqrt{\frac{1}{12}}\sin\theta\right)|\uparrow\downarrow\downarrow\uparrow\rangle\,. \tag{6.26}$$

The volume under the hump in position 2 of a such a SR-CPD is therefore proportional to

$$\Pi_{\uparrow\downarrow}(1,2) = \left(\frac{1}{2}\cos\theta - \sqrt{\frac{1}{12}}\sin\theta\right)^2 + \left(\frac{1}{2}\cos\theta + \sqrt{\frac{1}{12}}\sin\theta\right)^2. \tag{6.27}$$

This is referred to as the partial conditional probability $\Pi_{\uparrow\downarrow}(1,2)$ (partial because we are only considering part of the full SR-CPD, i.e. one peak). Using a normalized SR-CPD one can directly equate the volume underneath the hump in position 2 of our CI results to $\Pi_{\uparrow\downarrow}(1,2)$ and determine the angle θ_{CI}. Due to the involved squares this procedure is not necessarily unique. The unique solution can be found by comparing another hump (i.e. at position 3) to the corresponding partial conditional probability $\Pi_{\uparrow\downarrow}(1,3)$.

However it is important to note that this procedure is only exact as long as

- The overlap between sites is small

- The amount of double occupancy is small

From figure 6.5 it is clear that the first condition is fulfilled, however the second condition will introduce an error in the calculation. To keep this error small we minimized

$$\delta = (\Pi_{\uparrow\downarrow}(1,2) - \text{Vol}(2))^2 + (\Pi_{\uparrow\downarrow}(1,3) - \text{Vol}(3))^2 + (\Pi_{\uparrow\downarrow}(1,4) - \text{Vol}(4))^2, \tag{6.28}$$

where Vol(i) represents the volume under the SR-CPD hump at position i.

6.3.1 d-wave RVB determination

For the ground state SR-CPD shown in figure 6.5 this procedure yielded an angle $\theta_{CI} = 2.6186\pi$. From literature it is known that the spin function for the d-wave RVB is given as [96, 199]:

$$\begin{aligned}\chi = &\frac{1}{2\sqrt{3}}\left|\uparrow\uparrow\downarrow\downarrow\right\rangle - \frac{1}{\sqrt{3}}\left|\uparrow\downarrow\uparrow\downarrow\right\rangle + \frac{1}{2\sqrt{3}}\left|\uparrow\downarrow\downarrow\uparrow\right\rangle + \frac{1}{2\sqrt{3}}\left|\downarrow\uparrow\uparrow\downarrow\right\rangle \\ &- \frac{1}{\sqrt{3}}\left|\downarrow\uparrow\downarrow\uparrow\right\rangle + \frac{1}{2\sqrt{3}}\left|\downarrow\downarrow\uparrow\uparrow\right\rangle,\end{aligned} \tag{6.29}$$

which corresponds to an angle of $\theta_{d-RVB} = \frac{5\pi}{6}$. We can therefore conclude that our CI results show the presence of a d-wave RVB state with

$$1 - \left|\frac{\theta_{CI} - \theta_{d-RVB}}{\theta_{d-RVB}}\right| = 99.98\%, \tag{6.30}$$

fidelity. However while the CI result shows the presence of an RVB with high fidelity the SR-CPD also undoubtedly shows the presence of double occupancy. The volume of the hump at position 1 in figure 6.5 panel c) amounts to 10.39%. This might seem at first contradictory but is in fact the correct solution for an interaction strength of $U/t = 2.461$.

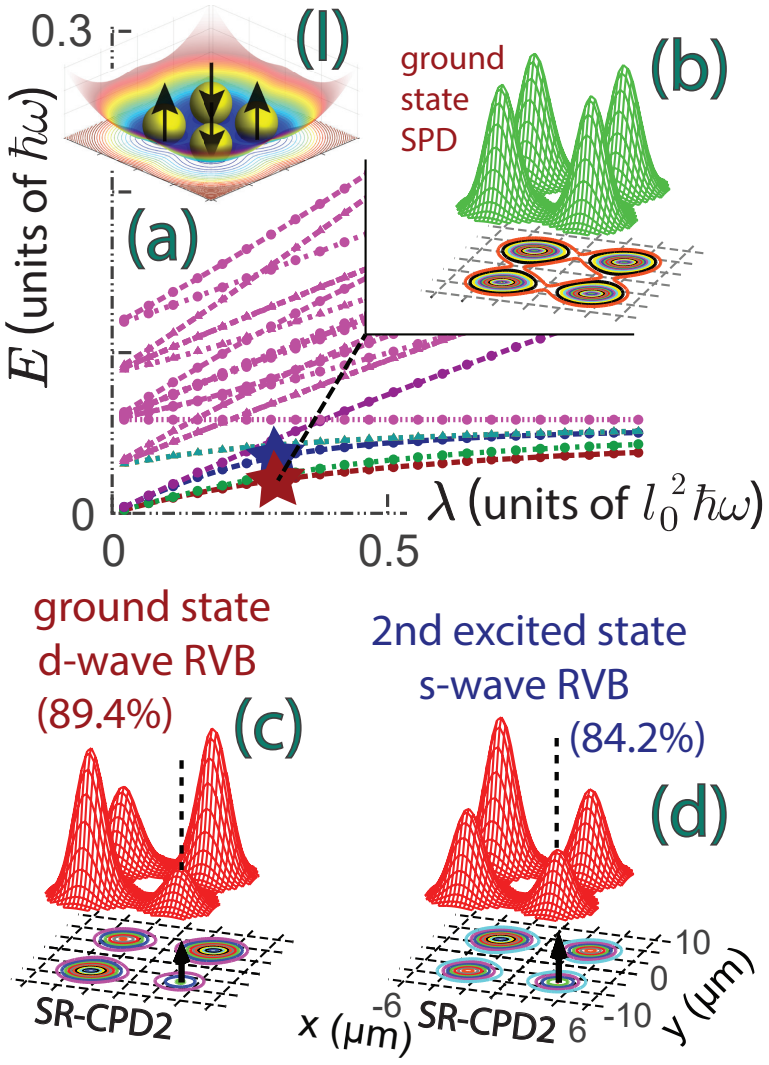

Figure 6.5: Spectrum, SPDs and SR-CPDs of the d- and s-wave RVB states in a single plaquette. Inset (I) shows a shematic representation of an exemplary spin component of the RVB state (see second term in equation (6.14)). It also shows a shematic of the external potential and the positioning of the particles within. Panel (a) shows the spectrum for four particles in a single plaquette, panel (b) shows the SPD for the interaction strength marked with a red star on the spectrum. Panel (c) and (d) show SR-CPDs, with panel (c) corresponding to the red star in the spectrum and panel (d) corresponding to the blue star in the spectrum. The trap parameters are $d = 6\,\mu\text{m}$, $\epsilon_b = V_b/V_0 = 0.5, \omega_x/(2\pi) = 1\,\text{kHz}, \omega_y/(2\pi) = 1\,\text{kHz}$ and the interaction potential is a Gaussian with $\sigma = 0.183\,\mu\text{m}$. The ground state in the weakly interacting region is a d-wave RVB and an s-wave RVB state is present as the second excited state in the system. The SPDs and SR-CPDs were calculated for a value of $U/t = 2.46$ and the corresponding points in the spectrum are marked by stars. The value of $U/t = 2.46$ was chosen to be close to the maximum of the pairing gap [199].

To show this we calculated the ground state solution of the Hubbard model

$$H = -t \sum_{<i,j>,\sigma} (c^{\dagger}_{i,\sigma} c_{j,\sigma} + c^{\dagger}_{j,\sigma} c_{i,\sigma}) + U \sum_{i=1}^{N} n_{i\uparrow} n_{i\downarrow}, \tag{6.31}$$

which is given as

$$\begin{aligned}
\psi_{gs} = {} & 0.455\big(|\uparrow,\downarrow,\uparrow,\downarrow\rangle + |\uparrow,\downarrow,\uparrow,\downarrow\rangle \big) \\
& + 0.228\big(-|\uparrow,\uparrow,\downarrow,\downarrow\rangle - |\uparrow,\downarrow,\downarrow,\uparrow\rangle - |\downarrow,\uparrow,\uparrow,\downarrow\rangle - |\downarrow,\downarrow,\uparrow,\uparrow\rangle \big) \\
& + 0.149\big(|\circ,\downarrow,\uparrow,\uparrow\downarrow\rangle - |\circ,\uparrow,\downarrow,\uparrow\downarrow\rangle \big) + 0.149\big(|\uparrow,\downarrow,\circ,\uparrow\downarrow\rangle - |\downarrow,\uparrow,\circ,\downarrow\uparrow\rangle \big) \\
& + 0.149\big(|\downarrow,\circ,\uparrow\downarrow,\uparrow\rangle - |\uparrow,\circ,\uparrow\downarrow,\downarrow\rangle \big) + 0.149\big(|\uparrow,\downarrow,\uparrow\downarrow,\circ\rangle - |\downarrow,\uparrow,\uparrow\downarrow,\circ\rangle \big) \\
& + 0.149\big(|\downarrow,\uparrow\downarrow,\circ,\uparrow\rangle - |\uparrow,\uparrow\downarrow,\circ,\downarrow\rangle \big) + 0.149\big(|\circ,\uparrow\downarrow,\uparrow,\downarrow\rangle - |\circ,\uparrow\downarrow,\downarrow,\uparrow\rangle \big) \\
& + 0.149\big(|\uparrow\downarrow,\circ,\downarrow,\uparrow\rangle - |\uparrow\downarrow,\circ,\uparrow,\downarrow\rangle \big) + 0.149\big(|\uparrow\downarrow,\uparrow,\downarrow,\circ\rangle - |\uparrow\downarrow,\downarrow,\uparrow,\circ\rangle \big) \\
& + 0.078\big(-|\circ,\circ,\uparrow\downarrow,\uparrow\downarrow\rangle + |\circ,\uparrow\downarrow,\uparrow\downarrow,\circ\rangle + |\uparrow\downarrow,\circ,\circ,\uparrow\downarrow\rangle - |\uparrow\downarrow,\uparrow\downarrow,\circ,\circ\rangle \big) \\
& = 0.79\chi_{d-RVB} + 0.38\chi_{do-d-RVB}.
\end{aligned} \tag{6.32, 6.33}$$

The first two lines of equation (6.33) are the d-wave RVB component and appear with dominant coefficients, however the wavefunction clearly contains contributions from doubly occupied states. Summing the squared coefficients of the spin basis functions that contain doubly occupied sites in equation (6.33) yields a double occupancy of 10.17% in excellent agreement with the CI result (the volume of the hump on position 1 indicating double occupancy in figure 6.5 panel (c) amounts to 10.6%).

6.3.2 s-wave RVB determination

The same analysis can be performed for the s-wave RVB state. The spin function for an s-wave RVB state is given in literature as [96, 199]:

$$\chi = \frac{1}{2} \left(|\uparrow\uparrow\downarrow\downarrow\rangle + |\downarrow\downarrow\uparrow\uparrow\rangle - |\downarrow\uparrow\uparrow\downarrow\rangle - |\uparrow\downarrow\downarrow\uparrow\rangle \right). \tag{6.34}$$

This corresponds to an angle of $\theta_{s-RVB} = -\frac{2\pi}{3}$. The angle determined from our CI calculation is $\theta_{CI} = -0.66632\pi$ corresponding to a fidelity of

$$1 - \left| \frac{\theta_{CI} - \theta_{s-RVB}}{\theta_{s-RVB}} \right| = 99.95\%. \tag{6.35}$$

However just like the ground state SR-CPD, the SR-CPD for the second excited state shows a non zero doubly occupancy. Therefore we computed the Hubbard model solution for the 2nd excited state at $U/t = 2.46$ which yielded:

$$\begin{aligned}
\psi_{2nd\ exc.} = 0.361\big(&- |\uparrow,\uparrow,\downarrow,\downarrow\rangle + |\uparrow,\downarrow,\downarrow,\uparrow\rangle + |\downarrow,\uparrow,\uparrow,\downarrow\rangle - |\downarrow,\downarrow,\uparrow,\uparrow\rangle \big) \\
&+ 0.185\big(- |\uparrow\downarrow,\circ,\uparrow\downarrow,\circ\rangle - |\circ,\uparrow\downarrow,\circ,\uparrow\downarrow\rangle \big) \\
&+ 0.153\big(|\circ,\downarrow,\uparrow,\uparrow\downarrow\rangle - |\circ,\uparrow,\downarrow,\uparrow\downarrow\rangle \big) + 0.153\big(- |\uparrow,\downarrow,\circ,\uparrow\downarrow\rangle + |\downarrow,\uparrow,\circ,\downarrow\uparrow\rangle \big) \\
&+ 0.153\big(|\downarrow,\circ,\uparrow\downarrow,\uparrow\rangle - |\uparrow,\circ,\uparrow\downarrow,\downarrow\rangle \big) + 0.153\big(- |\uparrow,\downarrow,\uparrow\downarrow,\circ\rangle + |\downarrow,\uparrow,\uparrow\downarrow,\circ\rangle \big) \\
&+ 0.153\big(|\downarrow,\uparrow\downarrow,\circ,\uparrow\rangle - |\uparrow,\uparrow\downarrow,\circ,\downarrow\rangle \big) + 0.153\big(- |\circ,\uparrow\downarrow,\uparrow,\downarrow\rangle + |\circ,\uparrow\downarrow,\downarrow,\uparrow\rangle \big) \\
&+ 0.153\big(|\uparrow\downarrow,\circ,\downarrow,\uparrow\rangle - |\uparrow\downarrow,\circ,\uparrow,\downarrow\rangle \big) + 0.153\big(- |\uparrow\downarrow,\uparrow,\downarrow,\circ\rangle + |\uparrow\downarrow,\downarrow,\uparrow,\circ\rangle \big) \\
&+ 0.093\big(- |\circ,\circ,\uparrow\downarrow,\uparrow\downarrow\rangle - |\circ,\uparrow\downarrow,\uparrow\downarrow,\circ\rangle - |\uparrow\downarrow,\circ,\circ,\uparrow\downarrow\rangle - |\uparrow\downarrow,\uparrow\downarrow,\circ,\circ\rangle \big)
\end{aligned} \tag{6.36}$$

$$= 0.722\chi_{s-RVB} + 0.48\chi_{do-s-RVB}. \tag{6.37}$$

This eigenfunction predicts a 14.52% double occupancy on site 1. The volume of the hump on position 1 indicating double occupancy in our CI result (see figure 6.5 panel (d)) amounts to 15.78% in good agreement with the Hubbard result.

6.3.3 Comparison with the t-J and Hubbard model

In the previous sections we compared the CI results to the predictions from the Hubbard model. Another widely used model, in particular for the analysis of high T_c superconductivity is the $t - J$ model and its variants [202–205]. The $t - J$ model is a spin model

that excludes double occupancy (see chapter 3 section 3.3 for more details). However the exclusion of double occupancy is a rather strong condition, particularly since the pairing gap appears for finite U (namely $U \leqslant 4.6$) and our CI calculations in section 6.3.1 and section 6.3.2 showed the presence of double occupancy. To investigate the feasibility of the $t-J$ model we compare its energy levels with the energy levels from the Hubbard model and our CI calculations. The results are displayed in figure 6.6. The left panel shows the ground state energy for 4 particles in a single plaquette, the right panel shows the ground state energy for 2 particles. One can clearly see that the $t-J$ model disagrees with the Hubbard and CI calculations for small U/t. Furthermore figure 6.6 also shows the amount of double occupancy as determined by our CI calculations further illustrating that the appearance of double occupancy correlates with the breakdown of the $t-J$ model for small systems.

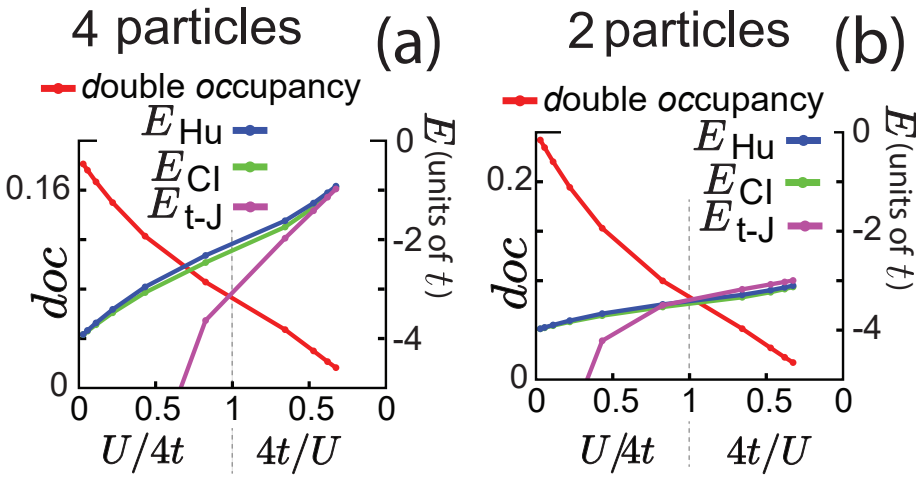

Figure 6.6: Energy and double occupancy of four (panel (a)) and two (panel (b)) particles in a single plaquette. Both panels show the ground state energy for the CI calculation, the Hubbard model and the t-J model as well as the amount of double occupancy (doc). The parameters used in the calculations are: $d = 6\,\mu\text{m}$, $\epsilon_b = V_b/V_0 = 0.5, \omega_x/(2\pi) = 1\,\text{kHz}, \omega_y/(2\pi) = 1\,\text{kHz}$

6.4 Pairing gap phase diagrams for a single plaquette

A useful quantity in the analysis of plaquette systems and the study of high T_c superconductivity in general is the pairing gap. The pairing gap phase diagram for our single plaquette CI calculation is obtained by calculating the energy difference

$$E_{pg} = 2E_{gs}(N=3) - E_{gs}(N=4) - E_{gs}(N=2), \tag{6.38}$$

where $E_{gs}(N=3)$ is the ground state energy for three particles in a single plaquette, $E_{gs}(N=4)$ is the ground state energy of four particles in a single plaquette and $E_{gs}(N=2)$ is the ground state energy of two particles in a single plaquette. This difference is calculated for a wide range of interaction strengths and for several different barrier heights. The resulting phase diagram is depicted in figure 6.7 panel (a) and (c). Such a phase diagram can also be plotted as a function of U/t after mapping λ to U and extracting the tunneling parameter t from the single particle spectrum, for details see section A.1 in the appendix. The such obtained phase diagrams are shown in figure 6.7 panels (b) and (d).
The phase diagrams in panel (a) and (c) of figure 6.7 (plotted as a function of the 2D interaction strength λ) show a narrowing of the pairing gap region for increasing ϵ_b. This is the expected behavior since increasing ϵ_b causes the tunneling parameter t to decrease (while the on site repulsion U is changing only marginally with increasing barrier). This has the intriguing consequence that there is maximum ($\approx 0.72\,\mathrm{Hz}$) in the pairing gap in panels a) and c). It occurs at $\lambda \approx 0.30 l_0^2 \hbar\omega, \epsilon_b \approx 0.43$.

The phase diagrams in panel b) and d) are plotted as a function of U/t and show a vanishing of the pairing gap past an interaction strength of $U/t \approx 4.6$ and a maximum of the pairing gap ($\Delta_p \approx 0.045t$) at $U/t \approx 2.6$ for all values of $\epsilon_b > 0.7$ (the case of high inter-site barrier). For smaller values of ϵ_b the hole pairing region in units of U/t decreases until hole pairing vanishes completely for an inter-well barrier of $\epsilon_b < 0.3$. We want to stress that this behavior can not be predicted by the standard Hubbard model.

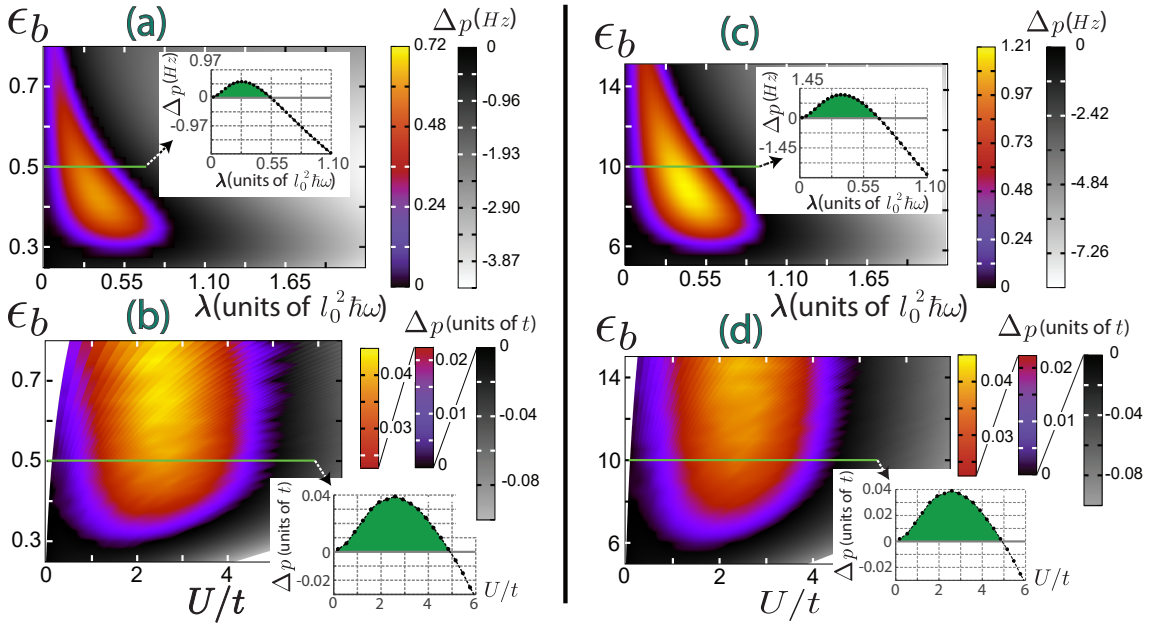

Figure 6.7: Phase diagram of the pairing gap in a single plaquette. Panels (a) and (b) show the pairing gap phase diagram for an inter-well distance of $d = 6\,\mu\text{m}$ and a barrier ranging from $0.67\,\text{kHz}(\epsilon_b = 0.25)$ to $2.14\,\text{kHz}(\epsilon_b = 0.8)$. The inter-well distance in panels (c) and (d) is $d = 2.5\,\mu\text{m}$ with the barrier height ranging from $2.32\,\text{kHz}(\epsilon_b = 5)$ to $6.98\,\text{kHz}(\epsilon_b = 15)$. The insets show cuts for an inter-site barrier of $\epsilon_b = 0.5$ (in panel (a) and (b)) and for an inter-site barrier of $\epsilon_b = 10$ (in panel (c) and (d)). Despite the markedly different barrier height ranges the physics of the two systems is nontheles comparable due to the difference in inter-well distances. Panels (a) and (c) show the pairing gap as a function of the 2-D interaction strength λ, panels (b) and (d) show the pairing gap as a function of U/t. The range of interaction for which a pairing gap can be observed becomes increasingly smaller for increasing barrier in panels (a) and (c) which is explained by the decrease in t with the increasing barrier. The pairing gap range in panels (b) and (d) converges to a maximum value of $\approx 4.6U/t$ for increasing barrier height which is in agreement with Hubbard model theory [184, 199, 206]. The parameters used in the calculations are: $\omega/(2\pi) = 1\,\text{kHz}$, $l_0 = 1.296\,\mu\text{m}$, $\sigma = 0.184\,\mu\text{m}$, $S = 0$, $S_z = 0$ (for 2 and 4 particles), $S_z = 0.5$ (for 3 particles).

This disappearance of the pairing gap below a certain barrier height (expressed in terms of ϵ_b) is present in all phase diagrams in figure 6.7. This is because for small barriers the overlap of the wavefunctions in neighboring wells becomes significant and explains why we need much larger values for ϵ_b in the small inter-site distance $d_w = 2.5\,\mu\mathrm{m}$ case of panel c) and d) ($\epsilon_b > 6$) in order to reach the pairing gap region.

While this overlap of neighboring wavefunctions cannot be captured within the standard Hubbard model, one can see this behavior in the evolution of the extended Hubbard parameter V (see chapter 2 section 3.2 for details on the extended Hubbard model). A plot of the Hubbard parameters U,V and t is depicted in figure 6.8. It shows the increasing importance of the inter-site density density interaction V with decreasing barrier.

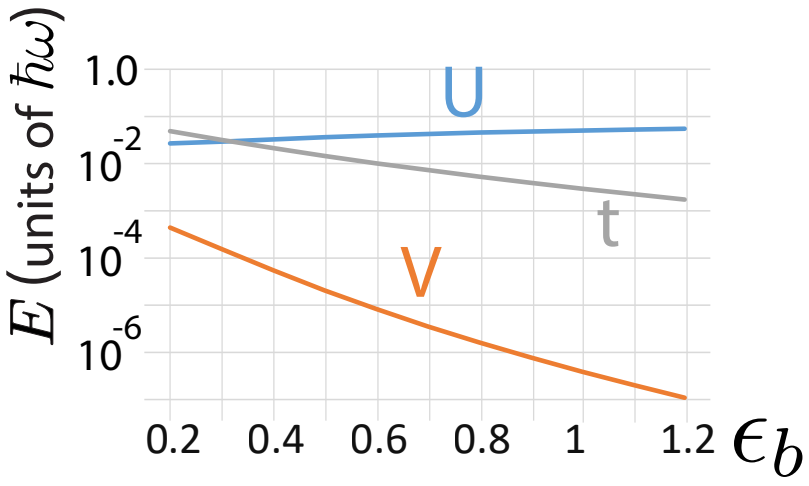

Figure 6.8: Extended Hubbard model parameters as a function of the inter-well barrier. For a definition of the Hubbard model parameters U, V and t see section 3.2. The value of the on-site interaction U increases slightly with increasing barrier, while the tunneling parameter t and the density density interaction V decrease with increasing interaction. It is notable that V is several orders below t for all values of the inter-well barrier, yet it seems to have a strong effect on the pairing gap.

6.5 Double plaquette systems

A canonical next step in a bottom up approach of ultracold optical lattices is the formation of a double plaquette. Instead of having to subtract energies of single plaquette systems

with different number of particles ($E_{pg} = 2E_{gs}(N = 3) - E_{gs}(N = 4) - E_{gs}(N = 2)$) the pairing gap in a double plaquette should be directly visible.

6.5.1 Pairing gap in a double plaquette

In this section we are going to study double plaquettes with weak inter-plaquette coupling. Figure 6.9 shows the spectrum (panel (a) and (b)), the quantum numbers for the lowest four states (panel (b)) and a schematic of the external double well potential (panel (I)). Since the energy levels are very close together we subtracted the energy of the lowest $S = 1$ state from all energy levels to better reveal the appearance of the pairing gap (from Hubbard model theory we know that the lowest $S = 1$ state is supposed to be the ground state at strong repulsion). The resulting spectrum is shown in figure 6.10. Indeed the spectrum shows an energy gap in the expected region of $0 < U/t < 4.6$ between the ground state 2-fold degenerate level (Ψ_{A1} and Ψ_{A2}) and the first excited 2-fold degenerate level (Ψ_{B1} and Ψ_{B2}). However to prove that the region of this energy gap corresponds to hole pairing we need to analyze the wave function anatomy. We could perform this analysis by calculating several SR-CPDs and studying the distribution of the density across the sites. However due to the number of sites, several SR-CPDs would be needed to arrive at definite result and interpreting the SR-CPDs in terms of hole pairing would not be intuitive. Ideally we want to be able to observe the pairing in a more direct way.

To achieve this we can use SR-CPDNs instead of SR-CPDs. To calculate an SR-CPDN we fix the position and spin of $N-1$ particles and look for the remaining particle, see chapter 2 section 2.7.3. Such an SR-CPDN is plotted in panel (c) of figure 6.10 and it is indeed able to reveal that the underlying wave function is a (4,2) state, which is a direct observation of hole pairing.

Alternatively the wave function structure can also be revealed through the process of symmetry braking. This method can be employed for degenerate states and works by adding or substracting the degenerate states. If for instance two degenerate states Ψ_1 and

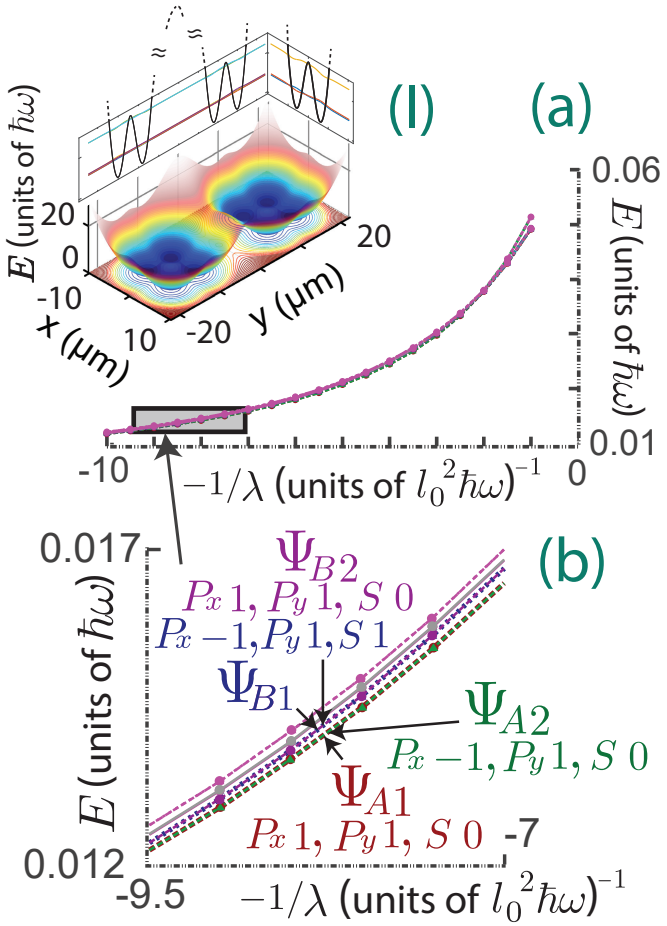

Figure 6.9: Spectrum for six particles in a double plaquette. The spectra in this figure correspond to the spectra in figure 6.10, however in contrast to figure 6.10 the energy of the triplet state has not been substracted. Panel (a) shows the spectrum as a function of $-1/\lambda$ from -10 to 0, while panel b enlarges the section of the spectrum from -9.5 to -7. Inset (I) shows a schematic of the external double well potential. Panel (b) has the parities along x and y and the total value of the spin S annotated for the lowest four states. The blue and red annotations correspond to the blue and red stars in figure 6.10.

Ψ_2 can be written as $\Psi_1 = |4,2\rangle + |2,4\rangle$ and $\Psi_2 = |4,2\rangle - |2,4\rangle$, we can create symmetry broken states $\Psi_- = \Psi_1 - \Psi_2 = 2\,|2,4\rangle$ and $\Psi_+ = \Psi_1 + \Psi_2 = 2\,|4,2\rangle$ which show the underlying structure of the wavefunction. This is precisely the case for the states Ψ_{A1} and Ψ_{A2} and shown in panel (d) and (e) of figure 6.10. The hole pairing creates a imbalance between the number of particles (charge) in the wells, which can be thought of as a charge-density wave (CDW). Just like the SR-CPDN this is evidence for the formation of hole pairs. The states Ψ_{B1} and Ψ_{B2} in contrast don't show a charge imbalance between the left and right well, but instead exhibit a spin polarization in the SPOLs (for the SPOL definition see chapter 2 section 2.7.4). This is indicative of an underlying $(3,3)$ state (3 particles in each well).

Note that the appearance of a pairing gap and the formation of hole pairs as described in this chapter is contingent on having well separated plaquettes. The situation becomes more complex for smaller inter-plaquette distances.

6.5.2 Double plaquette system with one plaquette distorted/tilted

Instead of symmetry braking by superposition we can also break the symmetry by tilting one of the plaquettes relative to the other or by distorting one of the plaquettes. Both of these methods yield insights into the many body wavefunctions and will be investigated in the following. Figure 6.11 shows spectra and SPDs for a tilted double plaquette in the first row (above the black line) and for a distorted double plaquette in the second row (below the black line). In both cases a transition from a $(4,2) \pm (2,4)$ to a $(3,3)$ state can be induced by increasing the tilt (first row) or the distortion (second row), which should be detectable in experiments.

6.5.3 Double plaquette system with small inter-plaquette distance

In the following we are analyzing a double plaquette with a small inter-plaquette distance $(D = 8\,\mu\mathrm{m})$. This leads to a more intricate spectrum which is depicted together with

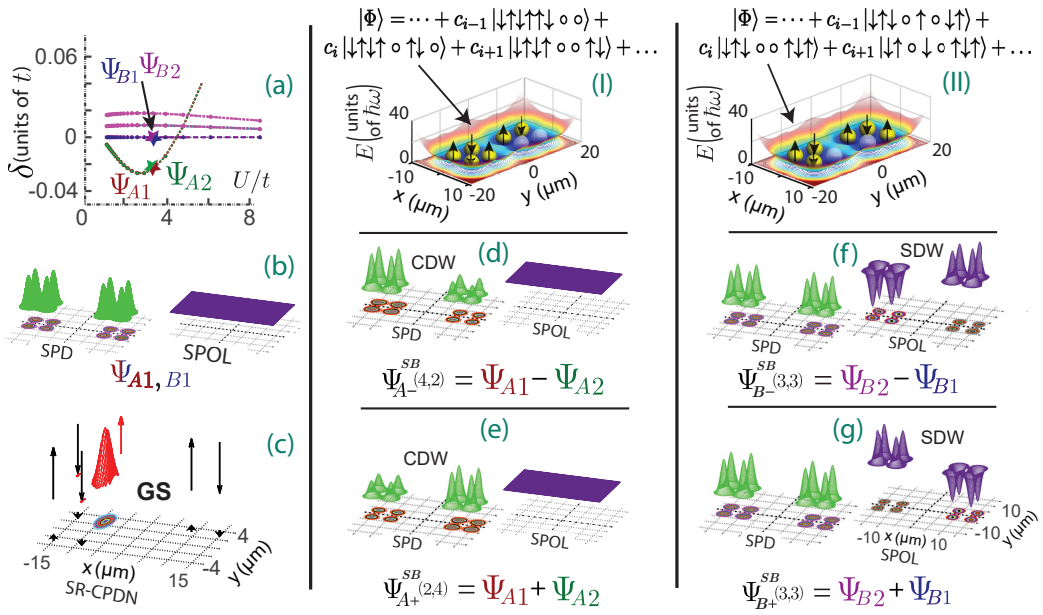

Figure 6.10: Wave function anatomy for six particles in a double plaquette. Panel (a) shows the spectrum from which the lowest energy state with a total spin of $S = 1$ has been substracted (as a result E_{Ψ_B} appears horizontal in the spectrum). A pairing gap is clearly visible up to a value of $U/t = 4.6$. Panel (b) shows the SPD and SPOL for the states Ψ_{A1} and Ψ_{B1} (they are identical). Of course it follows that the states Ψ_{A2} and Ψ_{B2} also have the same SPD and SPOL since they are degenerate with Ψ_{A1} and Ψ_{B1}. Panel (c) shows the n-body SR-CPD for the ground state (Ψ_{A1}). It shows a clear 4-2 signature with 4 particles in the left and 2 particles in the right. Had three fixed points be chosen on the right and two fixed points on the left one would observe a 2-4 configuration. The gs is a superposition of the two configurations, in the following abbreviated as (4,2)+(2,4). The middle column analyses the (4,2)+(2,4) states (Ψ_{A1}, Ψ_{A2}) via symmetry braking. Panel (d) and (e) show the symmetry broken states $\Psi^{SB}_{A-}(1,2)$ and $\Psi^{SB}_{A+}(2,1)$. The symmetry broken states clearly show the presence of the 4-2 and 2-4 component in the wavefunction. This can be thought of as a charge density wave. The top panel in the middle column shows a snipped of the general Hubbard wavefunction and illustrates one of the spin basis functions schematically in our external potential. The right column analyses the 3-3 states Ψ_{B1}, Ψ_{B2}. Panel (II) shows part of the general Hubbard model wavefunction and illustrates a 3-3 spin basis function in our external potential. Panel (f) and (g) show the symmetry broken 3-3 states. For the 3-3 states the process of symmetry braking reveals a spin density wave as is visible in the plots for the spin polarization (SPOL).

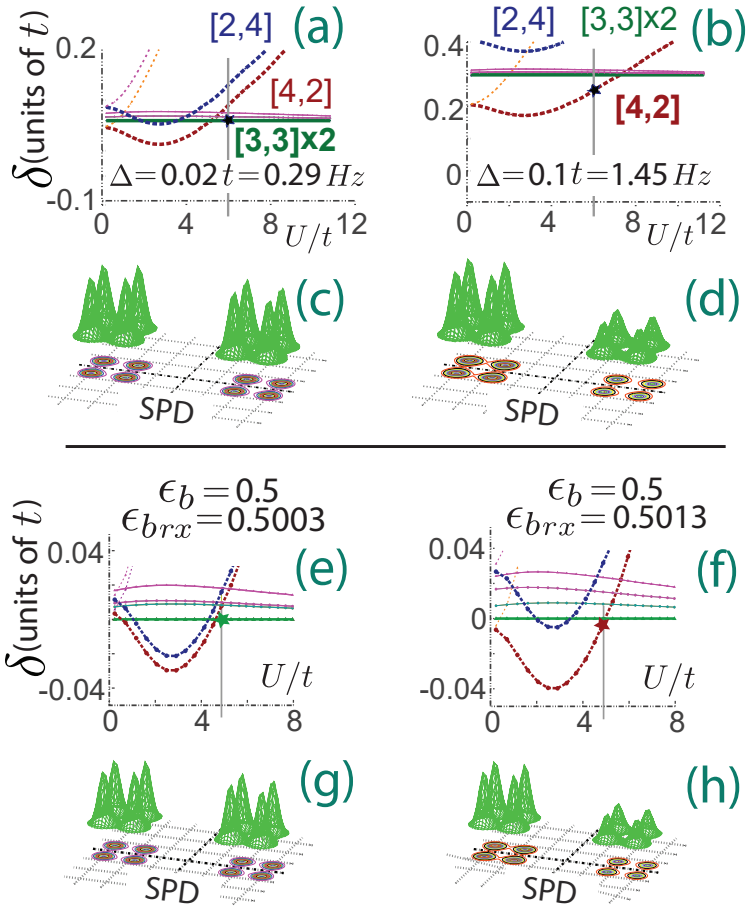

Figure 6.11: The top row shows the spectra and SPDs for a tilted double well at two different tilts. The spectra have the lowest $S = 1$ state substracted and have the structure of the underlying wavefunctions indicated for the (4,2) and (3,3) states. For the interaction strength marked by a gray line the ground state transitions from a (3,3) state to a (4,2) state with increasing tilt. The lower half of the figure (separated by a black line) shows symmetry braking by distorting the inter-plaquette barrier along the x direction in one of the plaquettes ($\epsilon_{bx} =$ varies, $\epsilon_{by} = 0.5$). Spectra for two different distortions $\epsilon_{bx} = 0.5003$ and $\epsilon_{bx} = 0.5013$ are shown in (e) and (f) and their corresponding SPDs are shown in (g) and (h). For the interaction strength marked with a solid line increasing the distortion to $\epsilon_b = 0.5013$ leads to a transition of the ground state from (3,3) in panel (g) to (4,2) in panel (h).

two SR-CPDNs in figure 6.12. The small inter-plaquette distance introduces an energy splitting between the ground state and 1st excited energy level, lifting the previously present degeneracy (compare with figure 6.10). The SR-CPDNs reveal that the ground state has a $(4,2)+(2,4)$ structure with a small admixture of a $(3,3)$ state, see the large red peak in the left plaquette and a smaller peak in the right plaquette in panel (b). The first excited state however is a pure $(4,2)+(2,4)$ configuration (see panel (c), only one large red peak).

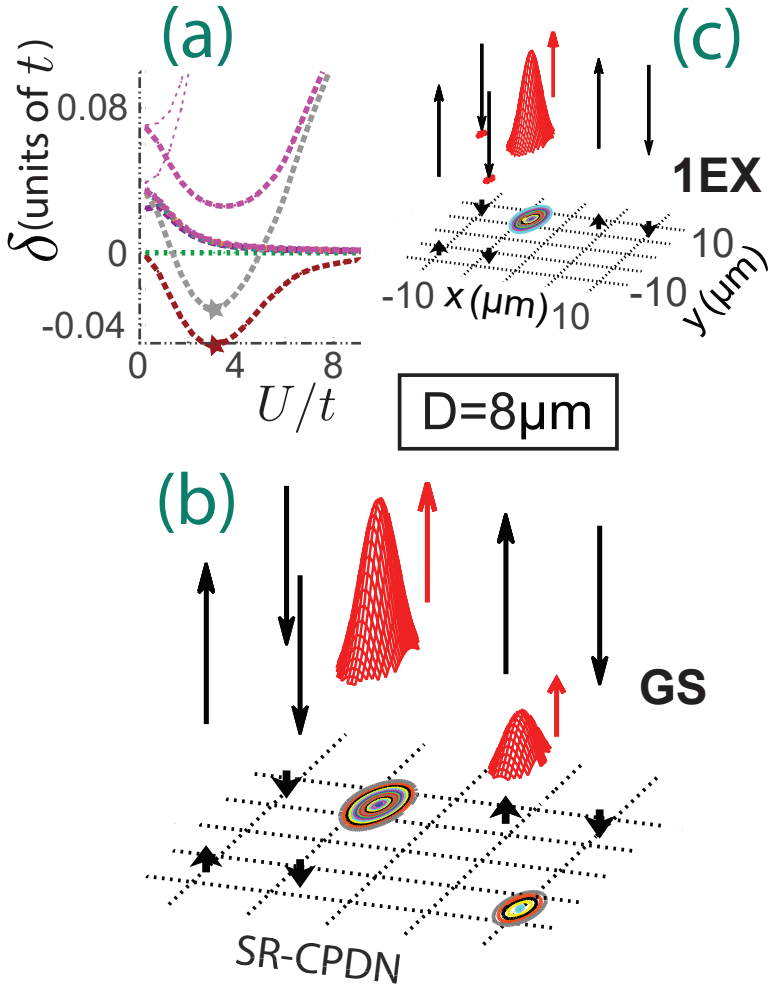

Figure 6.12: Panel (a) shows the CI energy spectrum for six particles ($S_z = 0$) in a double plaquette with an inter-plaquette distance of D=8 μm and and intra-plaquette distance of $d_w = 6\,\mu\mathrm{m}$. The inter-plaquette distance is small enough to exhibit a splitting of the ground state degeneracy (compare with figure 6.10). The red and grey stars indicate the interaction strengths ($U/t = 3.5$) and energy levels of the SR-CPDNs in panel (c) and (d) respectively. The SR-CPDN observation points are marked by black arrows which indicate spin directions.

More information and additional results can be found in our PRA paper [122]:

Benedikt B. Brandt, Constantine Yannouleas, and Uzi Landman. “Bottom-up configuration-interaction emulations of ultracold fermions in entangled optical plaquettes: building blocks of unconventional superconductivity”. In: *Physical Review A* 95.4 (2017), p. 043617

CHAPTER 7

SECOND-ORDER POSITION AND MOMENTUM SPACE CORRELATIONS OF FEW ULTRACOLD QUASI-ONE-DIMENSIONAL TRAPPED FERMIONS

Another aspect of ultracold systems that has recently gotten a lot of attention are position and momentum space correlation functions [106, 137, 207–211]. The foundations for this field were laid in 1955 with a great article by Löwdin [143] in which he outlines how an N-body operator can be calculated using the N-th order (also called N-point) density matrix. The diagonal part of the N-th order density matrix is nowadays known as the N-th order (or N-point) correlation function and has at the time of this writing become accessible experimentally up to second-order. The pristine environment of the ultracold atom systems and the tunability of the interaction strength promise to provide insights into quantum information processing [212], entanglement [213] and exotic many body states (e.g., Tonks-Girardeau states [81]).

While there are several theoretical results available for two-point spatial correlation functions for semiconductor quantum dots (for a small sample of the available literature see i.e.: [132, 195, 214]), studies of correlation functions for ultracold trapped atoms are less abundant. Furthermore the limited literature that is available focuses mostly on the two-point position space correlation functions [128, 215–217]. So far theoretical studies of the momentum correlation functions in optical lattices have been lacking.

In section 7.1 we analyze the correlation maps of two fermions in a single well, which is followed by an analysis of the correlation maps of two fermions in a double well in section 7.2. In section 7.3 we describe how to model the correlation map results analytically. Section 7.4 discusses two particle noise maps and section 7.5 analyzes the correlation maps for three and four particles in triple and quadruple wells.

Technical details:

The following paragraphs provide technical details about the calculation and are not needed to follow the arguments in the text. They can be skipped until the details become relevant to the reader.

There are two possible ways of analyzing two-point correlation functions, spin-resolved and spin unresolved. In the spin-resolved calculations each coordinate (x_1 and x_2 in position space or k_1 and k_2 in momentum space) is associated with a certain spin (either up or down in the case of two spin 1/2 particles), while in the spin unresolved calculation all possible spin-configurations are taken into account.

Furthermore all calculations in this chapter are quasi one dimensional, meaning that the confinement frequency along the y direction is much larger than the confinement frequency along the x direction. All the states considered in this chapter therefore have the same orbital along y (note that due to the symmetries of the Hamiltonian the wavefunction is a product in x and y). The calculations in this chapter utilize a short range Gaussian interaction potential (see equation (2.4) in chapter 2). Since the calculations in this chapter are quasi one-dimensional we could have also used a delta function potential without having to worry about the numerical intricacies mentioned in chapter 2 section 2.1. However the results are the same and we decided to use a Gaussian interaction in case we want to generalize our correlation map calculations to truly two-dimensional systems.

As mentioned in chapter 2 section 2.1 the numerical code that runs the calculations is inherently two-dimensional. The interaction strength g therefore has units of "energy·length^2" and is given in this chapter in units of $\hbar\omega l_0^2$. Note that this is in contrast to chapter 4 and chapter 5 where we gave the interaction strength in units of $\hbar\omega l_0$ to facilitate comparison with experiments that used these units. As of the time of this writ-

ing there are no published experimental results measuring the position and momentum space correlation functions. However some promising preliminary results are already shown in [137, 138].

Since the calculations in this chapter are quasi one dimensional we can plot the correlation maps using $y = 0.0, k_y = 0.0$ without loss of generality. This reduces the number of variables in the second-order correlation function from four ($\mathcal{P}(x_1, y_1, x_2, y_2)$ and $\mathcal{G}(k_1^x, k_1^y, k_2^x, k_2^y)$) to two ($\mathcal{P}(x_1, x_2) = \mathcal{P}(x_1, 0.0, x_2, 0.0)$ and $\mathcal{G}(k_1^x, k_2^x) = \mathcal{G}(k_1^x, 0.0, k_2^x, 0.0)$) and therefore allows us to plot them using contour plots. Note that for convenience we drop the superscript x in momentum space throughout this chapter.

7.1 Correlation maps for two fermions in a single well

We first analyzed two fermions in a qausi 1D single well. We already have ample experience for the behavior of this system from our earlier publication [133] and were able to connect the correlation maps with phenomena like the Wigner molecule formation and fermionization. The correlation maps for two particles in a single well in both position and momentum space at various interaction strengths are plotted in figure 7.1.

In the limit of **non-interacting particles** ($g = 0.0$) the second-order correlation map for the ground state is a product of the 1D single particle densities. This can easily be seen from the fact that the 2 particle wavefunction is a product of the single particle wavefunctions (which have a Gaussian shape).

In the limit of **strong repulsion** we know from our analysis in [133] that a Wigner molecule forms and that the position space SPD and CPDs approach the SPD and CPDs for the non-interacting triplet. We therefore expect this behavior to be reflected in the correlation maps as well. Indeed for strong repulsion the position space correlation maps for the ground state ($g = 5.486\hbar\omega l_0^2$ and $g = 54.86\hbar\omega l_0^2$, see panel g and i) approach the position space correlation map for the lowest energy triplet state (see panel k). The

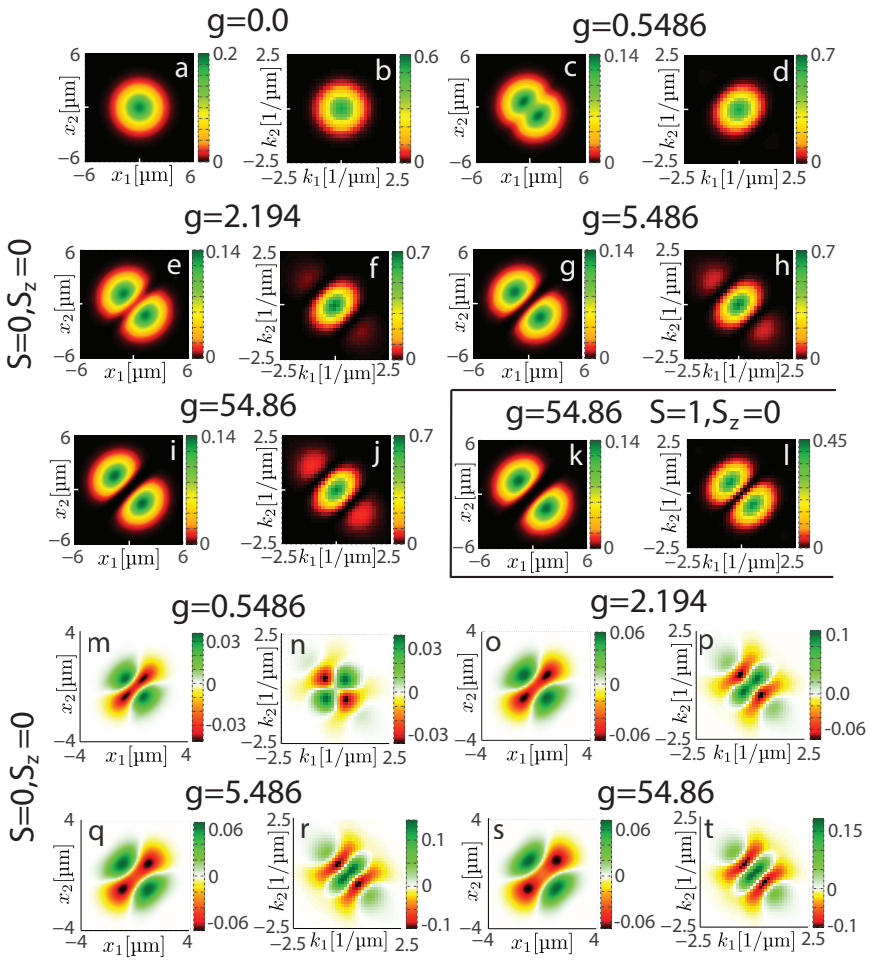

Figure 7.1: Evolution of position and momentum space correlations and noise maps for two particles in a single well at various interaction strengths. Panels a,c,e,g,i show the ground state position space correlation maps, panels b,d,f,h,j show the ground state momentum space correlation maps for various inter-particle interaction strengths. The appearance of a node along the diagonal in the position space correlation maps at strong repulsion ($g = 5.486$ and $g = 54.86$, panel g and i) indicates the formation of a Wigner molecule and thereby the localization of particles. Panels k and l show the position and momentum space correlation maps of the first excited state (a triplet). They were plotted at strong repulsion however they look the same for any interaction strength (the triplet wavefunction is independent of the interaction strength). Panels m to t show the position and momentum space noise maps for selected values of the interaction strength (see chapter 2 section 2.8.3 for the definition of the noise maps). The interaction strength g is given in units of $\hbar\omega l_0^2$. The parameters for our confining single well potential are $\epsilon_b = 0.5$, $\hbar\omega = \hbar\omega_x = 1\,\mathrm{kHz}$, $\hbar\omega_y = 100\,\mathrm{kHz}$ and the width of our short range (Gaussian type) two particle interaction in the CI calculation is $\sigma = 0.1833\,\mu\mathrm{m}$ (see the technical details section in the introduction to this chapter for additional calculation details).

strongly interacting ground state and the lowest energy triplet state however are clearly distinguishable in momentum space. This is a great example on why it is essential to study both the position and momentum space correlation functions.

The Wigner molecule ground state shows a characteristic interference pattern that arises from the localization of particles (the Wigner molecule formation). In the next section (section 7.2) we will see that this interference pattern also appears for two particles in a double well confirming our understanding of the particle localization.

The triplet state shows a clear node along the diagonal in momentum space. This is a consequence of the symmetry in the spin part and the resulting anti-symmetry in the space part of the wavefunction (which is present in both position and momentum space).

In panels m-t of figure 7.1 we analyze the frequently used [211, 218, 219] noise distributions for increasing interaction strength (see chapter 2 section 2.8.3 for an introduction and the definition of the noise distribution). The noise distribution for two non-interacting particles is zero as expected and therefore not shown. For increasing repulsion the increasingly prominent peaks in the position space noise distributions in panels m,o,q,s of figure 7.1 reflect the formation of an ultracold Wigner molecule (UCWM). For weak interactions it is remarkable that our momentum noise distribution in panel n closely resembles the square-like pattern that was recently measured in a system with a large number of 1D bosons [211]. For stronger repulsion (which corresponds to the Tonks-Giradeau regime mentioned in [211]) our momentum noise distributions show a striped like pattern that is a consequence of the interference pattern that develops in the second-order momentum correlation map.

7.2 Correlation maps for two fermions in a double well

The momentum correlation maps that were obtained from the two-particle in a single well calculation showed an increasingly prominent interference pattern for increasing particle localization. A natural continuation is to study two particles in a double well at various

separation distances and to analyze the impact of the well separation (which corresponds to the distance of the particles). Figure 7.2 shows the results for four different inter-well separations.

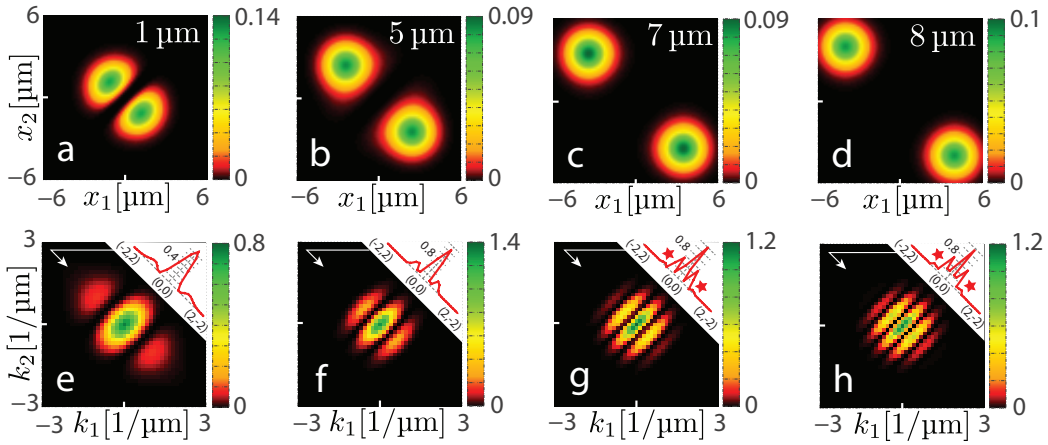

Figure 7.2: Evolution of ground state position and momentum space correlation maps for two particles in a double well at various double well distances. The ground state has quantum numbers $S = 0, S_z = 0$. Panels a-d show the position space correlation maps, panels e-h show the corresponding momentum space correlation maps. The insets in panels e-h show a cut along the off diagonal (from top left at $(k_1, k_2) = (-2, 2)$ to bottom right at $(k_1, k_2) = (2, -2)$). Stars in the insets are visual aides to bring attention to the smaller side peaks. Note that since we are studying the $S_z = 0$ states of two spin 1/2 particles, the spin resolved and spin unresolved correlation maps look the same. The interaction strength is $g = 54.86\hbar\omega l_0^2$. The parameters for our confining potential are $\epsilon_b = 0.5$, $\hbar\omega = \hbar\omega_x = 1\,\mathrm{kHz}$, $\hbar\omega_y = 100\,\mathrm{kHz}$ and the width of our short range (Gaussian type) two particle interaction is $\sigma = 0.1833\,\mu\mathrm{m}$ (see the technical details section in the introduction to this chapter for additional calculation details).

Panel a and e in figure 7.2 were calculated at a distance of $d = 1\,\mu\mathrm{m}$ which corresponds to a small inter-well barrier and the correlation maps in position and momentum space are very similar to the correlation maps for two particles in a single well (compare with figure 7.1 panel i and j). As we increase the inter-well distance the interference fringes in figure 7.2 become narrower and more numerous, indicating that the number of interference fringes depends on the distance between the particles.

7.3 Analytical modelling (based on the Heisenberg model)

The results in the previous two sections, in particular the dependence of the interference pattern on the inter-particle distance, suggests that one might be able to obtain simple analytical formulas that describe the position and momentum space correlation maps. Since the interference fringes and their pattern emerge for strong repulsion we decided to use the Heisenberg model to try to reproduce the correlation maps. The Heisenberg model (see chapter 2 section 3.4 for details) however only contains spins at particular sites, it does not contain a continuous position or momentum space coordinate like the one we plot in figure 7.1 or figure 7.2. It is therefore important to associate spatial wavefunctions with the spin-eigenfunctions that the Heisenberg model solution consists of. In the following we give a detailed description of this procedure for two particles in a double well, but it straigtforwardly generalizes to a higher number of wells and particles. The Heisenberg model for two particles in a double well (with eigenvalues centered around 0) is given as:

$$H = J\,\overrightarrow{S_1}\cdot\overrightarrow{S_2} - \frac{J}{4}, \tag{7.1}$$

where $\overrightarrow{S_1}$ and $\overrightarrow{S_2}$ are Spin operators and J is the coupling constant. Using $|\uparrow\downarrow\rangle$ and $|\downarrow\uparrow\rangle$ as basis this Hamiltonian can be expressed in matrix form as

$$H = J\begin{pmatrix} 0 & \frac{1}{2} \\ \frac{1}{2} & 0 \end{pmatrix}, \tag{7.2}$$

with eigenvalues e_1, e_2 and eigenvectors v_1, v_2

$$e_1 = -J/2, \tag{7.3}$$

$$e_2 = J/2, \tag{7.4}$$

$$v_1 = \frac{1}{\sqrt{2}}(|\uparrow\downarrow\rangle - |\downarrow\uparrow\rangle), \tag{7.5}$$

$$v_2 = \frac{1}{\sqrt{2}}(|\uparrow\downarrow\rangle + |\downarrow\uparrow\rangle). \tag{7.6}$$

These solutions however so far only reflect the spin part of the wavefunction. In order to include the space part we need to associate each spin-basis function with a determinant of spin-orbitals $\Psi_{n\sigma}$ (where n represents the n-th space orbital, σ represents the spin). The corresponding determinants are

$$|\uparrow\downarrow\rangle \longrightarrow \mathcal{D}_{\uparrow\downarrow}(\mathbf{x_1}, \mathbf{x_2}) = \frac{1}{\sqrt{2!}} \begin{vmatrix} \Psi_{1\uparrow}(\mathbf{x_1}) & \Psi_{2\downarrow}(\mathbf{x_1}) \\ \Psi_{1\uparrow}(\mathbf{x_2}) & \Psi_{2\downarrow}(\mathbf{x_2}) \end{vmatrix} \tag{7.7}$$

$$= \frac{1}{\sqrt{2!}}(\Psi_{1\uparrow}(\mathbf{x_1})\Psi_{2\downarrow}(\mathbf{x_2}) - \Psi_{1\uparrow}(\mathbf{x_2})\Psi_{2\downarrow}(\mathbf{x_1})) \tag{7.8}$$

$$|\downarrow\uparrow\rangle \longrightarrow \mathcal{D}_{\downarrow\uparrow}(\mathbf{x_1}, \mathbf{x_2}) = \frac{1}{\sqrt{2!}} \begin{vmatrix} \Psi_{1\downarrow}(\mathbf{x_1}) & \Psi_{2\uparrow}(\mathbf{x_1}) \\ \Psi_{1\downarrow}(\mathbf{x_2}) & \Psi_{2\uparrow}(\mathbf{x_2}) \end{vmatrix} \tag{7.9}$$

$$= \frac{1}{\sqrt{2!}}(\Psi_{1\downarrow}(\mathbf{x_1})\Psi_{2\uparrow}(\mathbf{x_2}) - \Psi_{1\downarrow}(\mathbf{x_2})\Psi_{2\uparrow}(\mathbf{x_1})), \tag{7.10}$$

where the factor $\frac{1}{\sqrt{2!}}$ normalizes the determinants. It generalizes to $\frac{1}{\sqrt{n!}}$ for n particles. We can use these two determinants together with the eigenvector v_1 to form our ground state wavefunction Φ_{gs} and the 2nd order density matrix $\mathcal{P}$

$$\Phi_{gs}(\mathbf{x_1}, \mathbf{x_2}) = \frac{1}{\mathcal{A}}\frac{1}{\sqrt{2}}(\mathcal{D}_{\uparrow\downarrow}(\mathbf{x_1}, \mathbf{x_2}) - \mathcal{D}_{\downarrow\uparrow}(\mathbf{x_1}, \mathbf{x_2})) \tag{7.11}$$

$$\mathcal{P}(\mathbf{x_1}, \mathbf{x_1}', \mathbf{x_2}, \mathbf{x_2}') = \Phi^{\dagger}_{gs}(\mathbf{x_1}', \mathbf{x_2}')\Phi_{gs}(\mathbf{x_1}, \mathbf{x_2}). \tag{7.12}$$

Here $\mathcal{A}$ is a normalization factor that ensures that the wave function is normalized to 1

(without the normalization factor this is not guaranteed due to a possible non-orthonormality of the spin-orbitals). Also it is important to mention that for the case of more than two particles the additional dimensions need to be integrated out to arrive at the second-order density matrix, i.e. for three particles:

$$\mathcal{P}(\mathbf{x_1}, \mathbf{x_1}', \mathbf{x_2}, \mathbf{x_2}') = \int_{-\infty}^{\infty} \Phi_{gs}^{\dagger}(\mathbf{x_1}', \mathbf{x_2}', \mathbf{x_3}) \Phi_{gs}(\mathbf{x_1}, \mathbf{x_2}, \mathbf{x_3}) d\mathbf{x_3}, \tag{7.13}$$

see [143] and chapter 2 section 2.8 for details. It is important to mention that for the integration in equation (7.13) we need to take into account the overlap (non-orthonormality) between the spin-orbitals.

So far we haven't made any assumptions about the single particle spin orbitals $\Psi_{n\sigma}$. In the following we use spin orbitals with a Gaussian function spatial part,

$$\Psi_{n\sigma}(\mathbf{x}) = \frac{1}{s\sqrt{2\pi}} \exp\left(-\frac{1}{2}\left(\frac{x - d_n}{s}\right)^2\right) \sigma, \tag{7.14}$$

---

where:

s:	is the width of the Gaussian
d_n:	is the center of the Gaussian (for particle n)
σ :	is the spin of particle n

For most practical cases (well separated particles) the normalization $\mathcal{A}$ in equation (7.11) is close to 1 and can be neglected, however for small values of d_n neighboring Gaussians will overlap and $\mathcal{A}$ becomes important.

We are now ready to compute the diagonal part of the second-order density matrix, which is in the following referred to as the two-point correlation function, in both position and momentum space. We are interested in the diagonal parts since they have a probabilistic interpretation [143] and can be used to obtain insights into the behavior of the full

wavefunction. The expressions for the two-point correlation functions are [220]

$$\mathcal{P}(\mathbf{x_1}, \mathbf{x_2}) = \mathcal{P}(\mathbf{x_1}, \mathbf{x_1}, \mathbf{x_2}, \mathbf{x_2}) \tag{7.15}$$

$$\mathcal{G}(\mathbf{k_1}, \mathbf{k_2}) = \frac{1}{4\pi^2} \int_{-\infty}^{\infty} e^{-i\mathbf{k_1}\mathbf{x_1}} \int_{-\infty}^{\infty} e^{i\mathbf{k_1}\mathbf{x_1}'} \int_{-\infty}^{\infty} e^{-i\mathbf{k_2}\mathbf{x_2}} \int_{-\infty}^{\infty} e^{i\mathbf{k_2}\mathbf{x_2}'} \mathcal{P}(\mathbf{x_1}, \mathbf{x_1}', \mathbf{x_2}, \mathbf{x_2}') d\mathbf{x_1} d\mathbf{x_1}' d\mathbf{x_2} d\mathbf{x_2}'. \tag{7.16}$$

It is pivotal in this step to take into account that integration over spin-orbitals with different spins yields 0. Also note that the fourier transforms corresponding to the primed coordinates have a different sign compared to the unprimed coordinates. The origin for the difference in sign is that the momentum space density matrix is defined by the momentum space wavefunctions

$$\mathcal{G}(\mathbf{k_1}, \mathbf{k_1}', \mathbf{k_2}, \mathbf{k_2}') = \Phi_{gs}^{\dagger}(\mathbf{k_1}', \mathbf{k_2}') \Phi_{gs}(\mathbf{k_1}, \mathbf{k_2}), \tag{7.17}$$

where the complex conjugation (in the $\Phi_{gs}^{\dagger}(\mathbf{k_1}', \mathbf{k_2}')$ term) causes the positive sign in the fourier transform associated with the primed coordinates.

In order to calculate the spin resolved correlation map we pick the terms involving the correct spin orbitals. For instance to calculate the correlation map with down spin for one particle and up spin for another particle we pick the terms involving $\uparrow^2\downarrow^2$ and $\downarrow^2\uparrow^2$. For a non spin resolved correlation map we take all terms into account. For 2 particles with the Gaussians centered at $d_1 = -d$ and $d_2 = d$ we obtain in this way for the spin resolved correlation map the following expression:

$$\mathcal{N}_{\mathcal{G}\downarrow\uparrow}(k_1, k_2) = \frac{4s^2 e^{-2s^2(k_1^2+k_2^2)} \cos^2(d(k_1 - k_2))}{\pi \mathcal{A}^2} \tag{7.18}$$

$$= \frac{2s^2 e^{-2s^2(k_1^2+k_2^2)} (\cos(2d(k_1 - k_2)) + 1)}{\pi \mathcal{A}^2}, \tag{7.19}$$

which is plotted in figure 7.3 (compare to panel f in figure 7.2).

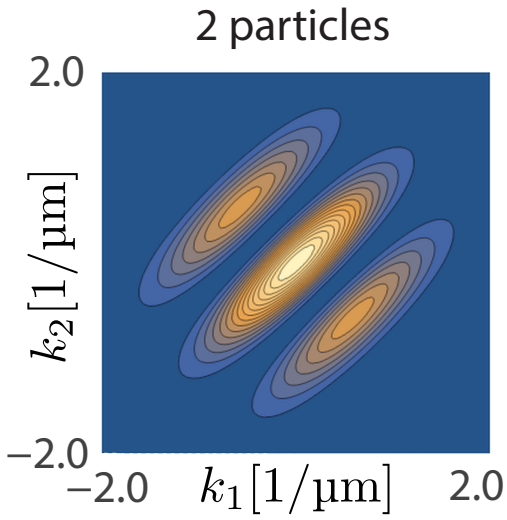

Figure 7.3: Momentum correlation map for two particles separated by a distance of $2d = 5.0\,\mu\mathrm{m}$ with a Gaussian width of $s = 0.71\,\mu\mathrm{m}$. This plot was obtained by plotting equation (7.19) with k_1 on the x-axis and k_2 on the y-axis. Compare to panel f in figure 7.2.

From equation (7.19) it is now apparent how the interference pattern emerges. The diagonal stripes are formed by the $\cos(2d(k_1 - k_2))$ term, which is multiplied by an exponential damping factor that depends on the width of the Gaussian.

Equation (7.19) also agrees with results found in the literature [221]. Here we wish to emphasize that the interference pattern created by the $\cos(2d(k_1 - k_2))$ term should be an experimentally detectable signature and is also observed in our CI calculations.

Furthermore it is important to mention that in the two particle case the analytic formulas for the spin unresolved and the spin resolved correlation map are the same. This is due to the two opposite spins in the two particle $S_z = 0.0$ system. For systems with more particles the spin-resolved and spin-unresolved analytic formulas are in general different.

7.3.1 Detailed comparison of analytical predictions with CI results

The success of the analytical modelling can be seen by comparing the analytical predictions with the microscopic CI results. In figure 7.4 we show a detailed comparison of the CI correlation maps with the correlation maps obtained from equation (7.19) for two particles

in a double well. The agreement of our analytical modelling with our microscopic CI calculations is excellent in both position and momentum space.

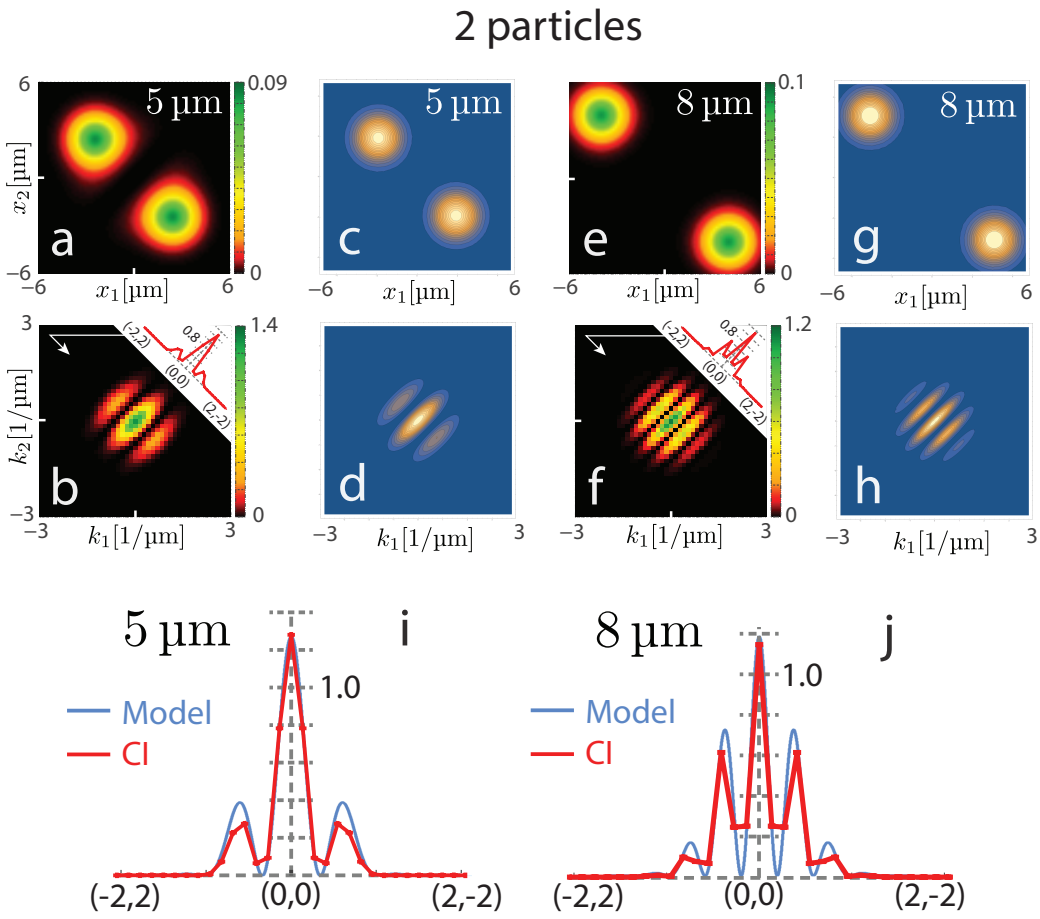

Figure 7.4: Position and momentum space correlation maps for two particles in a single well. This figure is similar to figure 7.2 except that we compare the CI correlation maps (shown in panels a,b,e,f) to the correlation maps obtained from the Heisenberg model (shown in panels c,d,g,h). Panels a,c,e,g show the position space correlation maps, panels b,d,f,h show the momentum correlation maps. Panel i and j show the off-diagonal cut (going from (k_1,k_2)=(-2,2) to (k_1,k_2)=(2,-2)) in momentum space, where the blue curve shows the Heisenberg model results and the red curve shows the full CI results. Note that since we are studying the $S_z = 0$ state of two spin 1/2 particles, the spin resolved and spin unresolved correlation maps look the same. The interaction strength is $g = 54.86\hbar\omega l_0^2$. The parameters for our confining potential are $\epsilon_b = 0.5$, $\hbar\omega = \hbar\omega_x = 1\,\mathrm{kHz}$, $\hbar\omega_y = 100\,\mathrm{kHz}$. The width of our short range (Gaussian type) two particle interaction in the CI calculation is $\sigma = 0.1833\,\mu\mathrm{m}$ (see the technical details section in the introduction of this chapter for additional details). The distance between the wells is annotated in the first row of panels.

7.4 Two particle noise maps

In order to develop a more detailed understanding of the noise maps in panels m-t of figure 7.1 we calculated the analytical noise distributions based on the Heisenberg modeling procedure described in section 7.3. This section shows the results for an analytical noise calculation for two particles separated by a distance $d = 3.4\,\mu\mathrm{m}$.

The definition of the noise distribution in position and momentum space is given in chapter 2 section 2.8.3 and reproduced here for convenience

$$\mathcal{N}_{\mathcal{P}}(\mathbf{x}_1, \mathbf{x}_2) = \mathcal{P}(\mathbf{x}_1, \mathbf{x}_2) - \rho(\mathbf{x}_1)\rho(\mathbf{x}_2), \tag{7.20}$$

$$\mathcal{N}_{\mathcal{G}}(\mathbf{k}_1, \mathbf{k}_2) = \mathcal{G}(\mathbf{k}_1, \mathbf{k}_2) - \tau(\mathbf{k}_1)\tau(\mathbf{k}_2). \tag{7.21}$$

To derive an analytical formula for the second-order noise distribution we need to to calculate the first and second-order correlation functions. The calculation to obtain the second-order correlation function is exactly the same as described in section 7.3. The first order correlation function can be obtained through integration from the second-order correlation function or directly from the many body wavefunction through integration (for details see chapter 2 section 2.8).

We have illustrated equation (7.20) and equation (7.21) in figure 7.5 where we plot the first and second-order position and momentum space correlation functions and the corresponding noise distributions. The noise distributions can be compared to figure 7.1, panel s and t (the Wigner molecule case). The remaining differences in shape between the analytical and the CI noise maps originate from the spatial structure of the Wigner Molecule, which is more complicated than the two separated Gaussians used for the analytical calculation. Nonetheless the qualitative features are well reproduced.

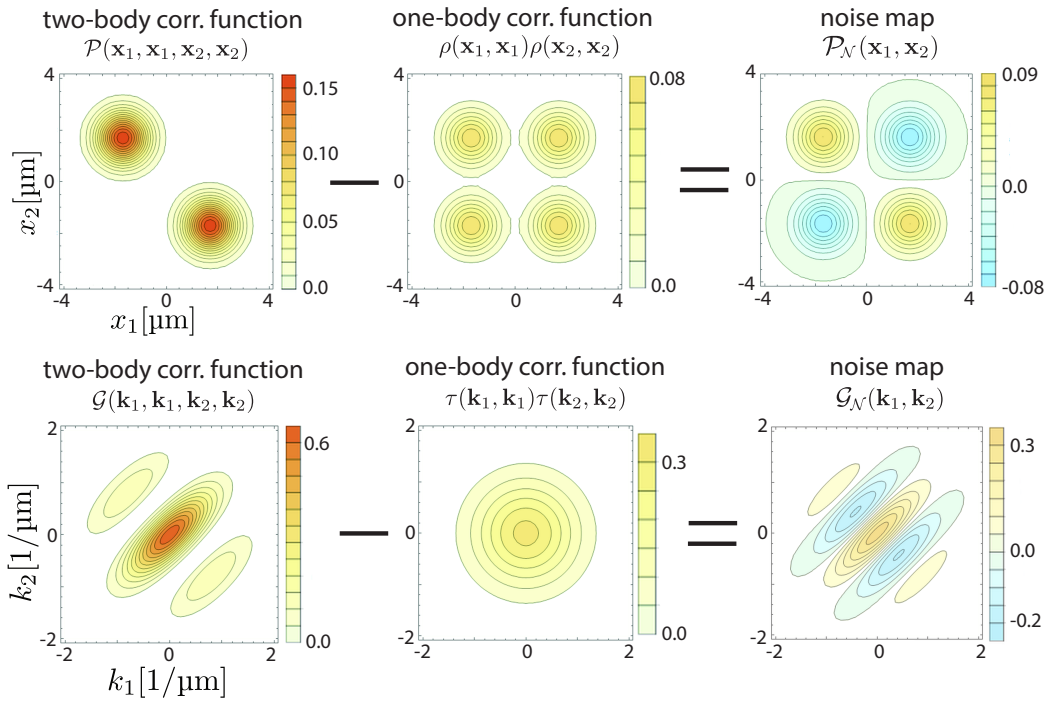

Figure 7.5: Illustration of the noise distribution calculation (see equation (7.20) and equation (7.21)), for two particles separated by a distance $d = 3.4\,\mu\mathrm{m}$. The noise distributions are obtained by subtracting the product of the first order correlation function for each particle from the second-order correlation function. The first row shows the position space correlation functions and the resulting position space noise distribution. The second row shows the same calculation in momentum space. The contour levels and the color scheme are the same throughout each row. The results are in good agreement with the panels s and t in figure 7.1. The Gaussian width σ was set to $\sigma = 0.71\,\mu\mathrm{m}$ in the Heisenberg modeling for this figure.

7.5 Correlation maps for three and four particles in triple and quadruple wells

In addition to the two-particle case that has been described in the preceding sections we also analyzed the second-order correlation maps for three and four particles in triple and quadruple wells. For those systems the spin resolved and spin unresolved results are different and both are studied in the following.

7.5.1 Results for three and four particles spin resolved (f$\downarrow\ell\uparrow$)

The second-order correlation functions for three particles in a triple well at strong repulsion are shown in figure 7.6 for two different inter-well distances ($d = 8\,\mu\mathrm{m}$ and $d = 4\,\mu\mathrm{m}$).

The position space correlations (top row in figure 7.6) now show additional peaks compared to the two particle correlation maps due to the presence of an additional particle. However just like the two-particle correlation maps they don't show any double occupancy which is a result of the strong repulsion. The different amplitudes for the different peaks are a result of the structure of the ground state wavefunction. This can be seen from the Heisenberg model. The ground state of a three particle linear Heisenberg chain with $S_z = 0.5$ is $(|\downarrow\uparrow\uparrow\rangle + 2\,|\uparrow\downarrow\uparrow\rangle + |\uparrow\uparrow\downarrow\rangle)/\sqrt{6}$ and since we are plotting a spin resolved 2nd order correlation map where the first coordinate (x_1) is associated with a down spin and the second coordinate (x_2) is associated with an up spin, the configuration with $x_1 = 0.0$ has four times the weight compared to the other configurations.

While there are some differences between the three particles in a triple well and the two particles in a double well position space correlation maps, the momentum space correlation maps look almost identical. In particular for an inter well distance of $8\,\mu\mathrm{m}$ the momentum space correlation map in figure 7.6 looks almost identical to the two paritcle momentum space correlation map in figure 7.2. They both show five interference fringes and have a similar spatial extend (circular and up to $\approx 1.8\,/\mu\mathrm{m}$). But even for a smaller spatial separation of $4\,\mu\mathrm{m}$ the two and three particle second-order momentum space correlations look

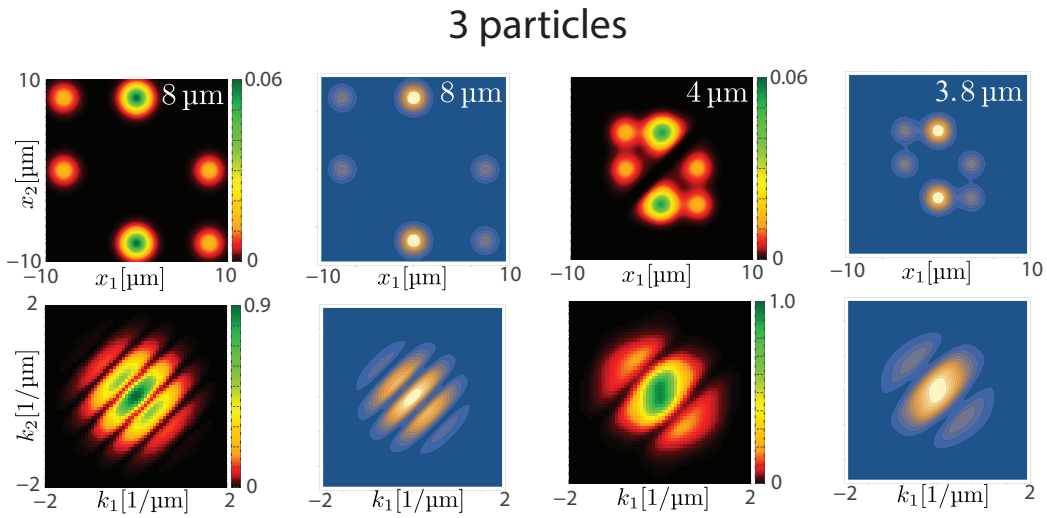

Figure 7.6: The position space (top row) and momentum (bottom row) spin resolved correlation maps for three particles in a triple well at strong repulsion for two different inter-well distances d. The spin configuration for this plot is fix down, look up ($f \downarrow l \uparrow$), meaning that the spin of particle 1 (associated with coordinate x_1 and k_1) is down and the spin of particle 2 (associated with coordinate x_2 and k_2) is up. The value of d is given in the panels and the same throughout a column. The interaction strength is $g = 54.86\hbar\omega l_0^2$. The parameters for our confining single well potential are $\epsilon_b = 0.5$, $\hbar\omega = \hbar\omega_x = 1\,\mathrm{kHz}$, $\hbar\omega_y = 100\,\mathrm{kHz}$ and the width of our short range (Gaussian type) two particle interaction in the CI calculation is $\sigma = 0.1833\,\mu\mathrm{m}$ (see the technical details section in the introduction of this chapter for additional details).

very similar, with the differences being attributable to the spatial overlap. **This suggests an underlying common physical principle**. To investigate this in more detail we are in the following studying the analytical correlation map expression for three particles in a triple well.

The analytic spin resolved expressions for three and four particles can be rather long, but they can be greatly simplified assuming that the Gaussians are equally spaced and far enough separated so that they have negligible overlap (i.e. the case of $2d = 8\,\mu\mathrm{m}$). For three Gaussians centered at $d_1 = -2d$, $d_2 = 0$ and $d_3 = 2d$ we obtain this way for the second-order position space spin resolved correlation function:

$$\begin{aligned}\mathcal{P}^{N=3}_{\downarrow\uparrow}(x_1,x_2) =& \frac{e^{-\frac{8d^2+6d(x_1+x_2)+x_1^2+x_2^2}{2s^2}}}{36\pi\mathcal{A}s^2}\Big(-2e^{\frac{3d(x_1+x_2)}{s^2}} + 4e^{\frac{2d(d+x_1+x_2)}{s^2}} \\ &+4e^{\frac{d(2d+3x_1+x_2)}{s^2}} + e^{\frac{d(5x_1+x_2)}{s^2}} + e^{\frac{d(2d+x_1+3x_2)}{s^2}} + e^{\frac{d(2d+5x_1+3x_2)}{s^2}} \\ &+e^{\frac{d(x_1+5x_2)}{s^2}} + 4e^{\frac{d(2d+3x_1+5x_2)}{s^2}} + 4e^{\frac{2d(d+2(x_1+x_2))}{s^2}}\Big)\end{aligned} \tag{7.22}$$

and in momentum space

$$\mathcal{G}^{N=3}_{\downarrow\uparrow}(k_1,k_2) = -\frac{2s^2e^{-2s^2\left(k_1^2+k_2^2\right)}}{9\pi\mathcal{A}}\Big(-4\cos(2d(k_1-k_2)) + \cos(4d(k_1-k_2)) - 6\Big). \tag{7.23}$$

The analytical correlation map for three particles immediately reveals the origin of the similarities to the two particle correlation map. Just like in the analytic formula for the two particle correlation map (see equation (7.19)) the exponential damping in momentum space is the cause of the circular confinement of the correlations and the $\cos$ terms create the diagonal interference pattern. The only difference to the two particle momentum space correlation function is the additional appearance of the $\cos(4d(k_1-k_2))$ term, which has a smaller amplitude and only slightly modifies the interference pattern created by the the $\cos 2d(k_1-k_2)$ term. The underlying physical reason for the similarity between the spin resolved interference patterns therefore seems to be a **short sightedness** where the smallest

distance in the correlation function has the biggest impact on its structure.

To confirm this hypothesis we looked at the correlation functions for four particles centered at $d_1 = -3d$, $d_2 = -d$, $d_3 = d$ and $d_4 = 3d$. The equation for the position space correlation function contains all the possible localized Gaussian terms and is lengthy and given in full in our publication [123]. The momentum space correlation function however reduces nicely

$$\mathcal{G}^{N=4}_{\downarrow\uparrow}(k_1,k_2) = \frac{s^2 e^{-2s^2\left(k_1^2+k_2^2\right)}}{9\pi\mathcal{A}}\left(\cos(6d(k_1-k_2)) - 2\left(\sqrt{3}-1\right)\cos(4d(k_1-k_2)) + \left(2\sqrt{3}+3\right)\cos(2d(k_1-k_2)) + 12\right). \tag{7.24}$$

Indeed the correlation function now includes a $\cos(6d(k_1 - k_2))$ term corresponding to the largest distance in the system ($6d$, between the outer wells). Its coefficient is even smaller than the one in front of the $\cos(4d(k_1 - k_2))$ term, causing only a small change in the structure of the correlation maps. The dominant contribution comes again from the term that is associated with the smallest distance (the $\cos(2d(k_1 - k_2))$ term). This we call the **short sightedness** of the spin resolved correlation function and could be the underlying reason for the similarity of our results and the results shown in [211] which were obtained for a large number of bosons.

The analytic momentum space correlation functions from equation (7.24) are plotted in figure 7.7. Furthermore in order to better be able to compare the 3-particle and 4-particle correlation function, we also plotted a cut along the off-diagonal and divided by the exponential damping, see figure 7.8.

7.5.2 Results for three and four particles spin unresolved

Figure 7.9 compares the spin unresolved position and momentum space correlation maps for three and four particles. Again the agreement between our microscopic CI results and

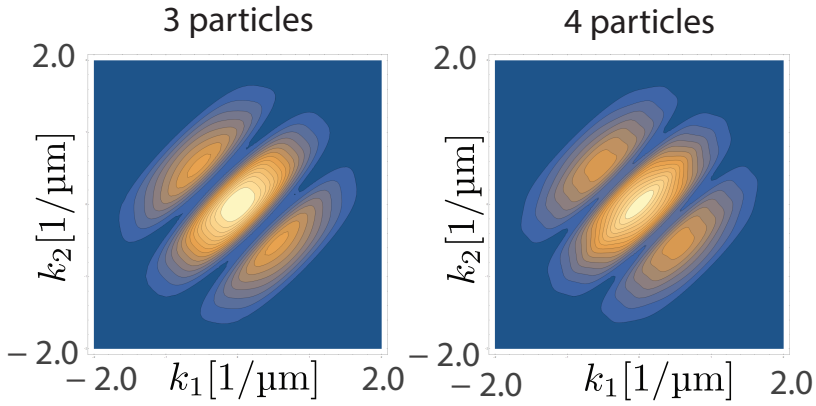

Figure 7.7: Spin resolved (f$\downarrow \ell \uparrow$) correlation maps for three (left panel) and four (right panel) particles at a distance $d = 4.8\,\mu m$. The plots were obtained by plotting equation (7.23) (left) and equation (7.24) (right) with k_1 on the x-axis and k_2 on the y-axis.

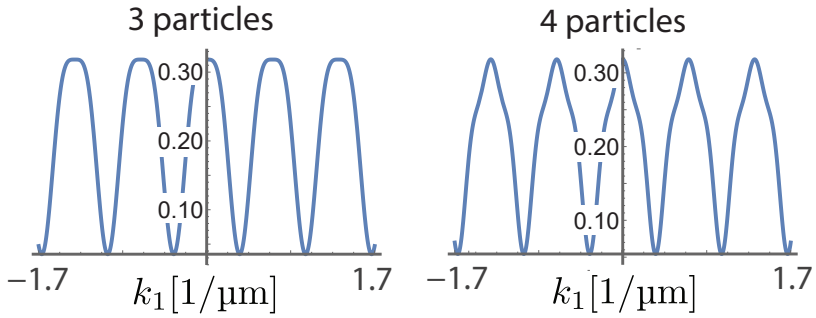

Figure 7.8: Plot of the interference pattern for the fix down look up (f$\downarrow \ell \uparrow$) spin configuration for three (left panel) and four (right panel) particles. The plots were obtained by plotting equation (7.23) and equation (7.24) divided by the exponential term $e^{-k_1^2-k_2^2}$ and setting $k_2 = -k_1$; that is these plots are cuts along the cross diagonal (top left to bottom right in figure 7.7). Neither plot shows higher order oscillations since the coefficients of the additional cosine terms are getting increasingly smaller. They modify the main oscillation pattern created by the $\cos(2d(k_1 - k_2))$ but don't show up as additional higher frequency oscillations.

the results from our analytical Heisenberg model is very good. While one can observe a difference between the two particle (see figure 7.4) and the three and four particle momentum space correlation maps (see figure 7.9), the interference pattern created by the smallest distance is still the dominant feature. The three and four particle spin unresolved momentum space correlation functions look identical which further corroborates the "short" sightedness of the momentum space correlation functions.

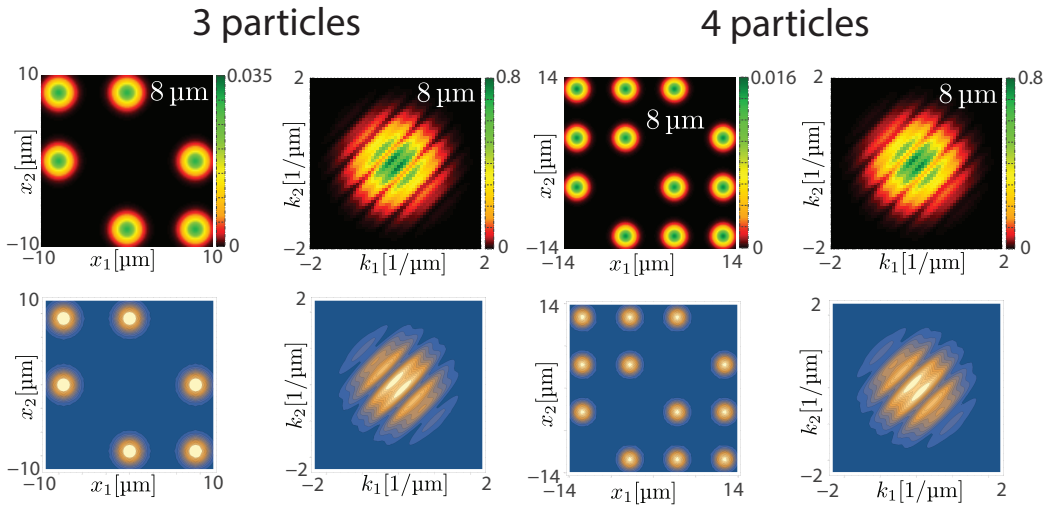

Figure 7.9: Spin unresolved correlation maps for three particles in a triple well and four particles in a quadruple well. The first and third column show the the position space correlation maps, the second and fourth column show the momentum space correlation maps. The top row shows the results from our CI calculation, the bottom row the results based on Heisenberg model. Both are in excellent agreement. The value of the inter well distance $2d$ is given in the panels and the same throughout a column. The interaction strength is $g = 54.86\hbar\omega l_0^2$. The parameters for our confining single well potential are $\epsilon_b = 0.5$, $\hbar\omega = \hbar\omega_x = 1\,\mathrm{kHz}$, $\hbar\omega_y = 100\,\mathrm{kHz}$ and the width of our short range (Gaussian type) two particle interaction in our CI calculation is $\sigma = 0.1833\,\mu\mathrm{m}$ (see the technical details section in the introduction of this chapter for additional details).

In addition to the results shown here, our publication [123] has further details and plots which for the sake of avoiding undue repetition were omitted from this chapter. In particular we provide the full spin resolved and spin unresolved analytic correlation map formulas for two, three and four particles in both position and momentum space. We also provide analytical formulas for the noise maps. We furthermore provide the three and four particle Heisenberg Hamiltonians and the corresponding ground state solutions:

Benedikt B. Brandt, Constantine Yannouleas, and Uzi Landman. "Two-point momentum correlations of few ultracold quasi-one-dimensional trapped fermions: Diffraction patterns". In: *Physical Review A* 96.5 (Nov. 30, 2017)

CHAPTER 8

INTERATOMIC INTERACTION EFFECTS ON SECOND-ORDER MOMENTUM CORRELATIONS OF TWO ULTRACOLD FERMIONS IN QUASI ONE DIMENSIONAL TRAPS

After our exploration of two to four strongly interacting particles in optical traps, we decided to explore the dependence of the correlation maps on the interaction strength in both position and momentum space. In [123] we had only briefly analyzed the interaction strength effects for two particles in a single well and had no analytical model to describe correlation maps away from very strong repulsion. While our CI code is able to accommodate calculations with arbitrary interaction strengths, we needed a different methodology for our analytical modeling, which was so far based on the Heisenberg model and therefore excluded double occupancy. A natural candidate for a spin model to describe the interacting system was the Hubbard model, which we implemented and compared with our microscopic CI results.

In addition to the ground state interaction dependence we decided to explore the correlation maps for the lowest three excited states, which one should be able to model with the Hubbard model Hamiltonian as well.

In section 8.1 we describe the analytical modeling, based on the Hubbard model. Section 8.2 analyses the ground state second-order correlation functions, and section 8.3 describes the correlation functions for the excited states. In section 8.4, we point out an important connection between CPDs and the position space correlation maps, and in section 8.5, we describe the connection between systems of ultracold atoms and the famous Hong Ou Mandel experiment.

Technical details:

The following paragraphs provide technical details about the calculation and are not needed to follow the arguments in the text. They can be skipped until the details become relevant to the reader.

The technical details given in the beginning of chapter 7 also apply to this section. Furthermore, throughout the CI calculations in this thesis we use the following parameters unless otherwise stated (a detailed description of these parameters and how they impact the Hamiltonian can be found in chapter 2):

- $\epsilon_b = 0.5$ (see equation (2.6))
- $\sigma = 0.01\,\mu\mathrm{m}$ in the Gaussian two-particle interaction term (see equation (2.4))
- $M_{^6\mathrm{Li}} = 10964.90 m_e$ where m_e is the mass of $^6\mathrm{Li}$

In this chapter we are exclusively analyzing two particle correlation maps with a spin projection of $S_z = 0$. As explained in chapter 7, the spin resolved and spin unresolved correlation maps are therefore the same, which is why we don't explicitly distinguish between the two in this chapter.

8.1 Analytical modelling (based on the Hubbard model)

To find an analytical model that accuaretely describes our CI results it was clear due to the variety of the interaction strengths that we needed to go beyond the Heisenberg model used in our previous work [123]. The natural candidate was the Hubbard model which turns out to describe our CI results in the case of well separated sites exceptionally well.

In the following, we illustrate in detail the derivation of the analytic interference formulas for two particles, allowing a rather immediate generalization to more complex cases,

like $N = 3$ and $N = 4$ particles. Like in chapter 7, section 7.3 we use localized Gaussians to represent the particles at the different sites (see chapter 7, section 7.3 for details on the Gaussians).

We use the following four spin basisfunctions as a basis of the Hubbard model: $|\uparrow\downarrow,\cdot\rangle$,$|\uparrow,\downarrow\rangle$,$|\downarrow,\uparrow\rangle$ and $|\cdot,\downarrow\uparrow\rangle$. Using these spin basisfunctions we diagonalize the fermionic Hubbard Hamiltonian,

$$H = -t\sum_{\sigma}\left(\hat{c}^{\dagger}_{1,\sigma}\hat{c}_{2,\sigma} + \hat{c}^{\dagger}_{2,\sigma}\hat{c}_{1,\sigma}\right) + U\sum_{i=1}^{2}\hat{n}_{i\uparrow}\hat{n}_{i\downarrow}. \tag{8.1}$$

For details on the Hubbard Hamiltonian and how to solve it, see chapter 3, section 3.1. For our purpose it is convenient to take into account that only the relative strength of U and t in the Hubbard Hamiltonian are important and that it can be written without loss of generality as

$$H = -\sum_{\sigma}\left(\hat{c}^{\dagger}_{1,\sigma}\hat{c}_{2,\sigma} + \hat{c}^{\dagger}_{2,\sigma}\hat{c}_{1,\sigma}\right) + \mathcal{U}\sum_{i=1}^{2}\hat{n}_{i\uparrow}\hat{n}_{i\downarrow}, \tag{8.2}$$

where the only parameter is the ratio $\mathcal{U} = U/t$ and the final energies are expressed in units of t. A general solution of this Hubbard Hamiltonian using the aforementioned spin basisfunctions is of the form

$$\Phi = A(\mathcal{U})\,|\uparrow\downarrow,\cdot\rangle + B(\mathcal{U})\,|\uparrow,\downarrow\rangle + C(\mathcal{U})\,|\downarrow,\uparrow\rangle + D(\mathcal{U})\,|\cdot,\downarrow\uparrow\rangle\,. \tag{8.3}$$

The coefficients $A - D$ of course satisfy the constraint that Φ is normalized. Naturally, such a Hubbard model solution only yields the spin part of the wave function. To include the spatial component of the wave function we need to associate each spin basisfunction with a determinant of spin orbitals. In the following we write a spin orbital as $\Psi_{j,\sigma}(x) = \Psi_j(x)\sigma$, where j denotes the space orbital at position d_j and σ represents the spin. The

corresponding determinants D to each basisfunction are

$$\mathcal{D}_{|\uparrow\downarrow,\cdot\rangle}(x_1,x_2) = \frac{1}{\sqrt{2!}}(\Psi_{1\uparrow}(x_1)\Psi_{1\downarrow}(x_2) - \Psi_{1\uparrow}(x_2)\Psi_{1\downarrow}(x_1)) \tag{8.4}$$

$$\mathcal{D}_{|\uparrow,\downarrow\rangle}(x_1,x_2) = \frac{1}{\sqrt{2!}}(\Psi_{1\uparrow}(x_1)\Psi_{2\downarrow}(x_2) - \Psi_{1\uparrow}(x_2)\Psi_{2\downarrow}(x_1)) \tag{8.5}$$

$$\mathcal{D}_{|\downarrow,\uparrow\rangle}(x_1,x_2) = \frac{1}{\sqrt{2!}}(\Psi_{1\downarrow}(x_1)\Psi_{2\uparrow}(x_2) - \Psi_{1\downarrow}(x_2)\Psi_{2\uparrow}(x_1)) \tag{8.6}$$

$$\mathcal{D}_{|\cdot,\uparrow\downarrow\rangle}(x_1,x_2) = \frac{1}{\sqrt{2!}}(\Psi_{2\uparrow}(x_1)\Psi_{2\downarrow}(x_2) - \Psi_{2\uparrow}(x_2)\Psi_{2\downarrow}(x_1)) \tag{8.7}$$

We can therefore write our full wavefunction, including the space and spin parts, as

$$\begin{aligned}\Phi(x_1,x_2) =& \frac{1}{N}\left(A(\mathcal{U})\mathcal{D}_{|\uparrow\downarrow,\cdot\rangle}(x_1,x_2) + B(\mathcal{U})\mathcal{D}_{|\uparrow,\downarrow\rangle}(x_1,x_2) + \right.\\ & \left. C(\mathcal{U})\mathcal{D}_{|\downarrow,\uparrow\rangle}(x_1,x_2) + D(\mathcal{U})\mathcal{D}_{|\cdot,\uparrow\downarrow\rangle}(x_1,x_2)\right),\end{aligned} \tag{8.8}$$

where the factor $1/N$ normalizes the wavefunction and is in general dependent on the Gaussian positions d_j and the Gaussian width s. In the special case of well separated particles $N = 1$ since the individual determinants are normalized and orthogonal and the coefficients $A - D$ are normalized.

This procedure of obtaining a full spin and space wavefunction from the Hubbard model can be straightforwardly generalized to a larger number of particles by adapting the Hubbard Hamiltonian and the mapping of the spin-primitives to their respective determinants.

We can now use the such obtained wavefunction $\Phi(x_1, x_2)$ together with the formulas for the correlation functions described in chapter 7, section 7.3.

8.2 Analysis of ground state 2nd order correlation functions

In figure 8.1 we analyze the second-order position and momentum space correlation maps from no interaction ($U/t = 0$) to very strong repulsion ($U/t = 20$). Figure 8.1 shows the correlation maps for two different external confining frequencies ($\hbar\omega_x/(2\pi) = 8\,\mathrm{kHz}$ and

$\hbar\omega_x/(2\pi) = 15\,\mathrm{kHz}$) at constant distance $d = 2\,\mu\mathrm{m}$.

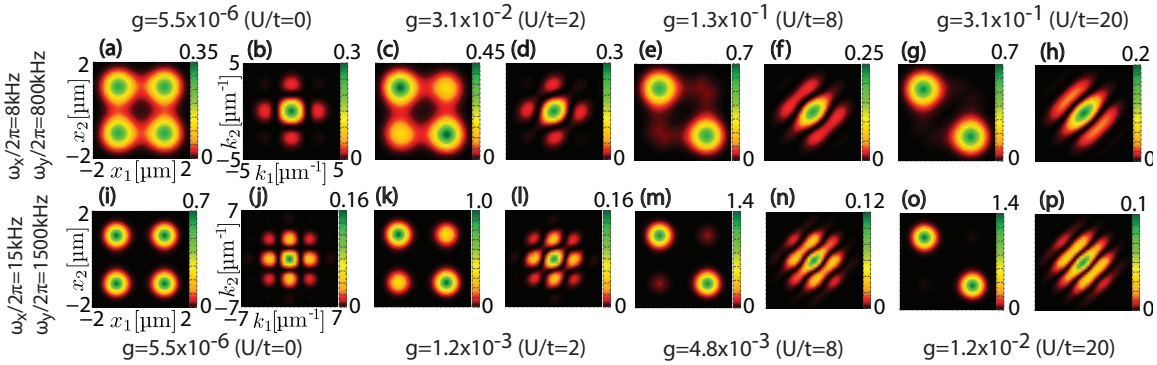

Figure 8.1: second-order position and momentum space correlation maps for two particles in a double well at varying interaction strengths, calculated with our CI methodology. We show results for two different confining frequencies ($\hbar\omega_x/(2\pi) = 8\,\mathrm{kHz}, \hbar\omega_y/(2\pi) = 800\,\mathrm{kHz}$ and $\hbar\omega_x/(2\pi) = 15\,\mathrm{kHz}, \hbar\omega_y/(2\pi) = 1500\,\mathrm{kHz}$) that correspond to quasi 1D systems. The interwell distance is $d = 2\,\mu\mathrm{m}$. For the remaining CI parameters see the introduction to this chapter. Position space correlation maps are shown in panels (a)(c)(e)(g)(i)(k)(m)(o) and momentum space correlation maps are shown in panels (b)(d)(f)(h)(j)(l)(n)(p). The value of the interaction strength expressed in terms of the CI interaction strength g and the corresponding Hubbard on-site interaction U are given next to the panels. The process of extracting the Hubbard model parameters from our CI calculations is described in section A.1

In **position space** the non-interacting correlation map shows four equally sized peaks, reflecting the fact that double (along the main diagonal $x_1 = x_2$) and single occupancy (along the cross diagonal $x_1 = -x_2$) are equally likely for non-interacting particles. For increasing interaction strength the amount of double occupancy decreases and fully vanishes for $U/t = 20$ (see panels (g) and (o) in figure 8.1).

In **momentum space** the evolution of the correlation map is more complex. For non-interacting particles the momentum space correlation map shows a pattern of dots that are arranged in a plaid pattern. With increasing repulsion the dots of the plaid pattern that lie on the same diagonal gradually connect until they form full interference fringes for very strong repulsion (which we are already familiar with based on our analysis in chapter 7).

By comparing the top ($\hbar\omega/(2\pi) = 8\,\mathrm{kHz}$) and bottom ($\hbar\omega/(2\pi) = 8\,\mathrm{kHz}$) rows it is clear that the increased frequency increases the number of interference patterns. This corre-

sponds to additional correlations between the particles. The additional interference fringes in figure 8.1 panel (p) reveal correlations between particles that have the same absolute value, but different sign, momenta.

The analytical modeling described in section 8.1 allows us to write an analytical expression for the two-body correlation functions. In momentum space the two-body correlation function is given by:

$$\begin{aligned}\mathcal{G}^{S=0,S_z=0}_{\mathrm{Hub,gs}}(k_1,k_2) &\propto \frac{2s^2 e^{-2s^2(k_1^2+k_2^2)}}{\pi(\mathcal{U}\mathcal{Q}(\mathcal{U})+16)} \\ &\times \Big((\mathcal{U}\mathcal{Q}(\mathcal{U})+8)\cos(2d(k_1-k_2)) + 8\cos(2d(k_1+k_2)) \\ &+ 4\mathcal{Q}(\mathcal{U})\cos(2dk_1) + 4\mathcal{Q}(\mathcal{U})\cos(2dk_2) + \mathcal{U}\mathcal{Q}(\mathcal{U}) + 16 \Big),\end{aligned} \tag{8.9}$$

---

where:

s:	is the width of the displaced Gaussian
d:	is the distance between the Gaussians
$\mathcal{U}$:	$\mathcal{U} = U/t$
$\mathcal{Q}(\mathcal{U})$:	$\mathcal{Q}(\mathcal{U}) = \sqrt{\mathcal{U}^2+16} + U$

We write equation (8.9) using $\propto$ since equation (8.9) is only normalized for negligible Gaussian overlap (a large inter-well distance). If there is overlap between the Gaussian functions we need to include an additional normalization factor.

Equation (8.9) shows several interesting characteristics. The interference pattern created by the $\cos$ terms is damped by an overall exponential factor which depends on the width s of the displaced Gaussians. This is the reason why the top and bottom row in figure 8.1 show different numbers of interference fringes in momentum space.The larger confining frequency leads to a smaller harmonic oscillator length ($l_0 = (\hbar/(mw_x))^{1/2}$) and therefore a smaller Gaussian width s.

Furthermore it is notable that equation (8.9) includes all possible combinations of k_1 and k_2 in the $\cos$ terms, namely $\cos 2d(k_1 - k_2)$, $\cos 2d(k_1 + k_2)$, $\cos 2d(k_1)$ and $\cos 2d(k_2)$.

For strong repulsion only the $\cos 2d(k_1 - k_2)$ term survives and we recover the result from equation (7.19) chapter 7. The superposition of all the different $\cos$ terms for $U = 0$ is what creates the plaid pattern of dots for the non-interacting correlation map in figure 8.1 panels (b) and (j).

In figure 8.2 panel (a) we plot the coefficients in front of the individual $\cos$ terms in the ground state correlation function as a function of U/t. This allows us to identify the dominant contributions to the interference patterns at varying interaction strengths. Panel (c) shows a plot of the analytical ground state correlation function at $U/t = 8$, where the dominant interference contribution arises due to the $\cos(2d(k_1 - k_2))$ term and is slightly modified by the other cos terms (compare with the case of very strong repulsion in figure 8.1 panel (p)). Panel (b) shows the plot of the coefficients in front of the $\cos$ terms for the 3rd excited state and panel (d) shows the 3rd excited state momentum correlation map for an interaction strength of $U/t = 8$. The interference pattern now develops along the cross-diagonal ($k_1 = -k_2$), although the overall pattern is still reminiscent of the ground state correlation map pattern in panel (c).

This indicates that the excited states should also have insightful analytical expressions and we are going to explore their behavior in the next section.

8.3 Analysis of excited state 2nd order correlation functions

In figure 8.3 panels (b)-(f) we show 2nd order correlation maps for the excited states. The interaction strengths at which the correlation maps were calculated are given next to the figures and are indicated by stars in the spectrum in panel (a).

The correlation map for the 1st excited state (panel (b)) shows a node along the main diagonal, in contrast to the ground state correlation map (compare with figure 8.1 panel (n)). The first excited state is a triplet (total spin $S = 1$) and the appearance of a node along the main diagonal is a manifestation of the Pauli exclusion principle (since the space-part of the wavefunction needs to be antisymmetric for a triplet). Furthermore we have verified

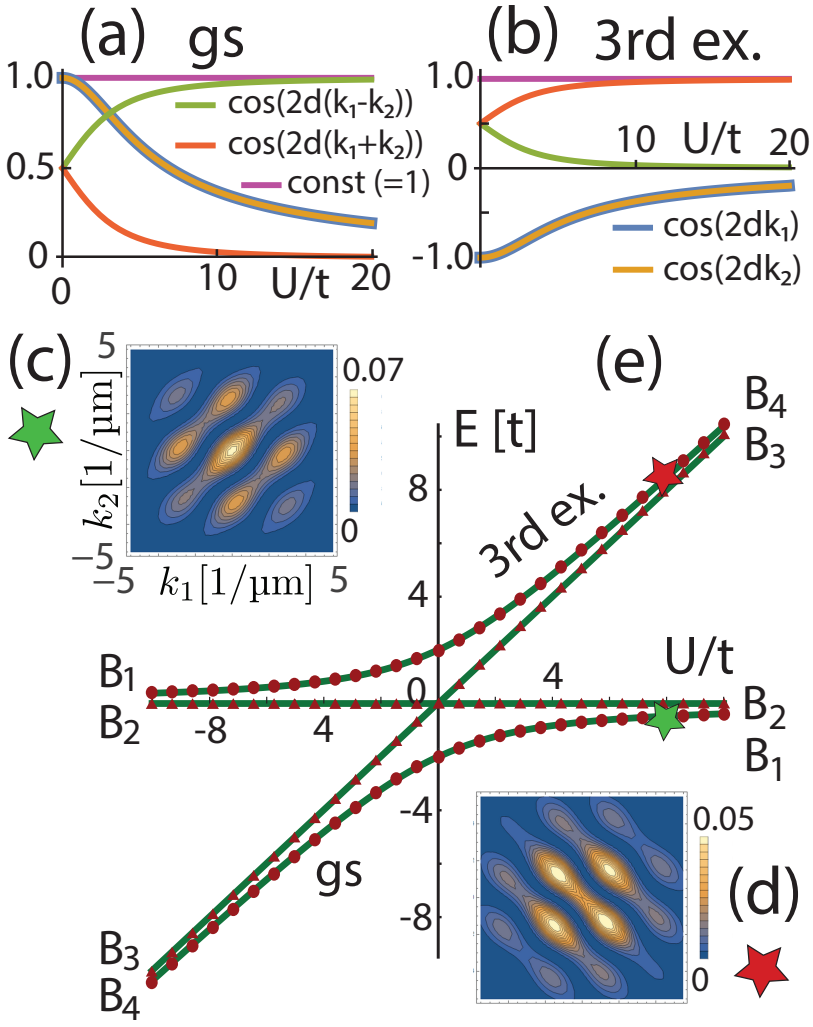

Figure 8.2: Analysis of the Hubbard model 2nd order momentum correlation maps for the ground and 3rd excited state. The ground state 2nd order momentum correlation map is shown in panel (c) and the correlation map for the 3rd excited state is shown in panel (d). As shown in equation (8.9) the momentum correlation maps are created by a superposition of cos terms, where the coefficients in the superposition depend on U. In panels (a) and (b) we plot those coefficients as a function of U for the ground and 3rd excited state respectively. In panel (e) we show the energy spectrum of the two-site Hubbard model, where the red dots indicate values obtained from our CI calculations. The agreement between the Hubbard and CI energies is excellent. The symbols B_1, B_2, B_3, B_4 represent the four Bell states to which the Hubbard model states converge at $U/t \to \pm\infty$. It is worth noting that the order of the bell states in the energy spectrum is reversed for $U/t \to -\infty$ compared to $U/t \to \infty$. For a description of how we map the Hubbard parameters to our CI parameters see section A.1. The majority of parameters for the CI calculation are given in the introduction to this chapter and the remaining ones for this plot are $\hbar\omega/(2\pi) = 15\,\mathrm{kHz}$, $d = 2\,\mu\mathrm{m}$.

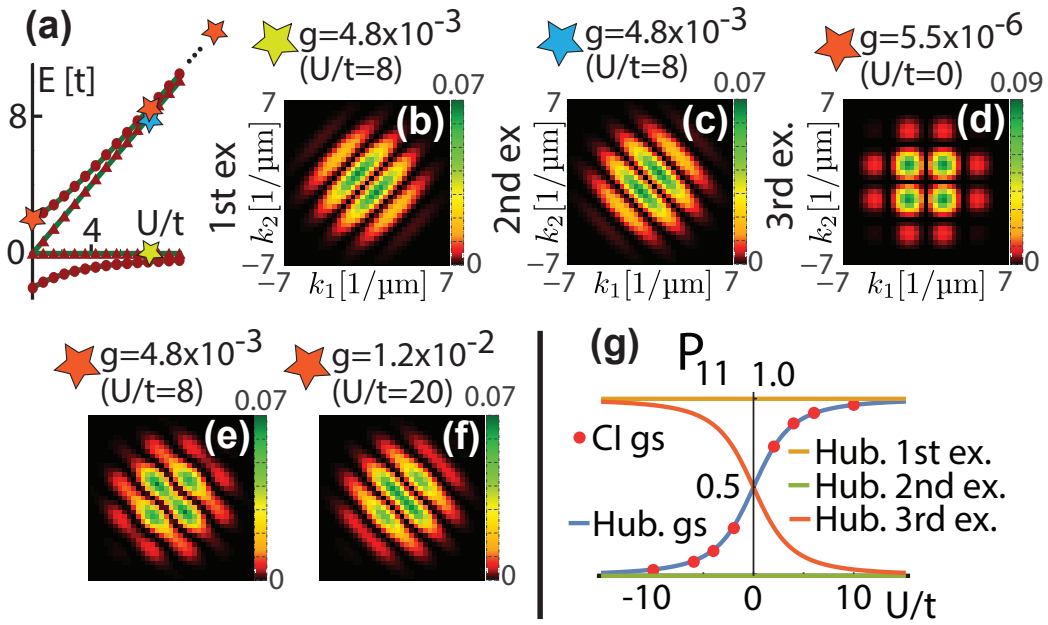

Figure 8.3: Analysis of the first three excited states 2nd order momentum correlation maps for two fermions in a double well. Panel (b) shows the momentum correlation map for the first excited state, panel (c) shows the momentum correlation map for the 2nd excited state and panels (d) (e) and (f) show the correlation map for the third excited state at varying interaction strengths. It should be noted that the correlation maps for the 1st and 2nd excited state are independent of the interaction strength, whereas the third excited state has a strong dependence (similar to the ground state) on the interaction strength. Panel (a) shows a plot of the Hubbard model energy spectrum and the calculated CI energies (red dots) for the lowest four states which are in very good agreement. The CI calculation gives the values of higher excited states as well, but here we only plot the four lowest to facilitate the Hubbard model comparison. Panel (a) also marks the values of U/t for which the correlation maps were calculated (the yellow star corresponds to panel (b), the blue star to panel (c) and the orange stars to panels (d)-(f)). Panel (g) shows the probability for single occupancy (P_{11}) for the four Hubbard model states (solid lines) and our CI results (red dots) for the ground state. The majority of parameters for the CI calculation are given in the introduction to this chapter and the remaining ones for this plot are $\hbar\omega/(2\pi) = 15\,\mathrm{kHz}$, $d = 2\,\mu\mathrm{m}$.

using our CI calculations that the correlation function for the 1st excited state is independent of the interaction strength. This can also directly be seen from the Hubbard model eigenfunctions (see chapter 3, section 3.1 for the solutions of the two-particle Hubbard model).

The correlation map for the 2nd excited state (panel (c), a singlet, total spin $S = 0$) is also independent of the interaction strength, however this time the interference pattern develops along the cross-diagonal ($k_1 = -k_2$).

The correlation maps for the 3rd excited state (panels (d)-(f)) show a strong dependence on the interaction strength. Just like the ground state the third excited state correlation maps in general have single and double occupancy components. However the third excited state shows some interesting differences compared to the ground state. For non interacting particles (panel (d), $U/t = 0$) the correlation map shows a square pattern of circular dots, with a prominent hole in the middle (compare this to figure 8.1 panel (j)). Furthermore the interference pattern for the 3rd excited state develops along the cross-diagonal ($k_1 = -k_2$).

In equation (8.10), equation (8.11) and equation (8.12) we give the momentum space correlation function for the first, second and third excited state. The first excited state is a triplet (total spin $S = 1$), while the second and third excited states are singlets (total spin $S = 0$).

$$\mathcal{G}^{S=1,S_z=0}_{\text{Hub,1st ex}}(k_1, k_2) \propto \frac{4s^2 e^{-2s^2(k_1^2+k_2^2)} \sin^2(d(k_1 - k_2))}{\pi}, \tag{8.10}$$

---

where:

- s: is the width of the displaced Gaussian
- d: is the distance between the Gaussians

The 2nd order momentum correlation function for the 1st excited state is shown in equation (8.10) and it is note worthy that the correlation function and therefore the interference pattern does not depend on the interaction strength. This is a result of the wavefunction

structure, which does not contain any double occupancy for the first excited state.

$$\mathcal{G}^{S=0,S_z=0}_{\text{Hub,2nd ex}}(k_1,k_2) \propto \frac{4s^2 e^{-2s^2(k_1^2+k_2^2)} \sin^2(d(k_1+k_2))}{\pi}, \tag{8.11}$$

---

where:

s: is the width of the displaced Gaussian

d: is the distance between the Gaussians

The 2nd order momentum correlation function for the 2nd excited state is shown in equation (8.11). Just like the 1st excited state it also doesn't depend on the interaction strength. However in this case the underlying wavefunction contains only terms with double occupancy. The 2nd order momentum correlation function for the third excited state is given in equation (8.12)

$$\begin{aligned}\mathcal{G}^{S=0,S_z=0}_{\text{Hub,3rd ex}}(k_1,k_2) &\propto \frac{2s^2 e^{-2s^2(k_1^2+k_2^2)}}{\pi(16-\mathcal{U}\mathcal{P}(\mathcal{U}))} \\ &\times \Big((8-\mathcal{U}\mathcal{P}(\mathcal{U}))\cos(2d(k_1-k_2)) + 8\cos(2d(k_1+k_2)) \\ &- 4\mathcal{P}(\mathcal{U})\cos(2dk_1) - 4\mathcal{P}(\mathcal{U})\cos(2dk_2) + 16 - \mathcal{U}\mathcal{P}(\mathcal{U}) \Big),\end{aligned} \tag{8.12}$$

---

where:

s: is the width of the displaced Gaussian

d: is the distance between the Gaussians

$\mathcal{U}$: $\mathcal{U} = U/t$

$\mathcal{P}(\mathcal{U})$: $\mathcal{P}(\mathcal{U}) = \sqrt{\mathcal{U}^2+16} - U$

Similar to the ground state wavefuntion the wavefunction of the third excited state in general contains singly and doubly occupied terms, which is why it shows a strong dependence on the interaction strength.

The position space correlation maps can be obtained in a similar fashion, however they do not reduce to nice compact expressions and are therefore not given here. They can however easily be calculated according to the methodology described in section 8.1.

In order to compare the analytic correlation function formulas with the microscopic CI results we plot the analytic formulas in position and momentum space for the ground and excited states in figure 8.4.

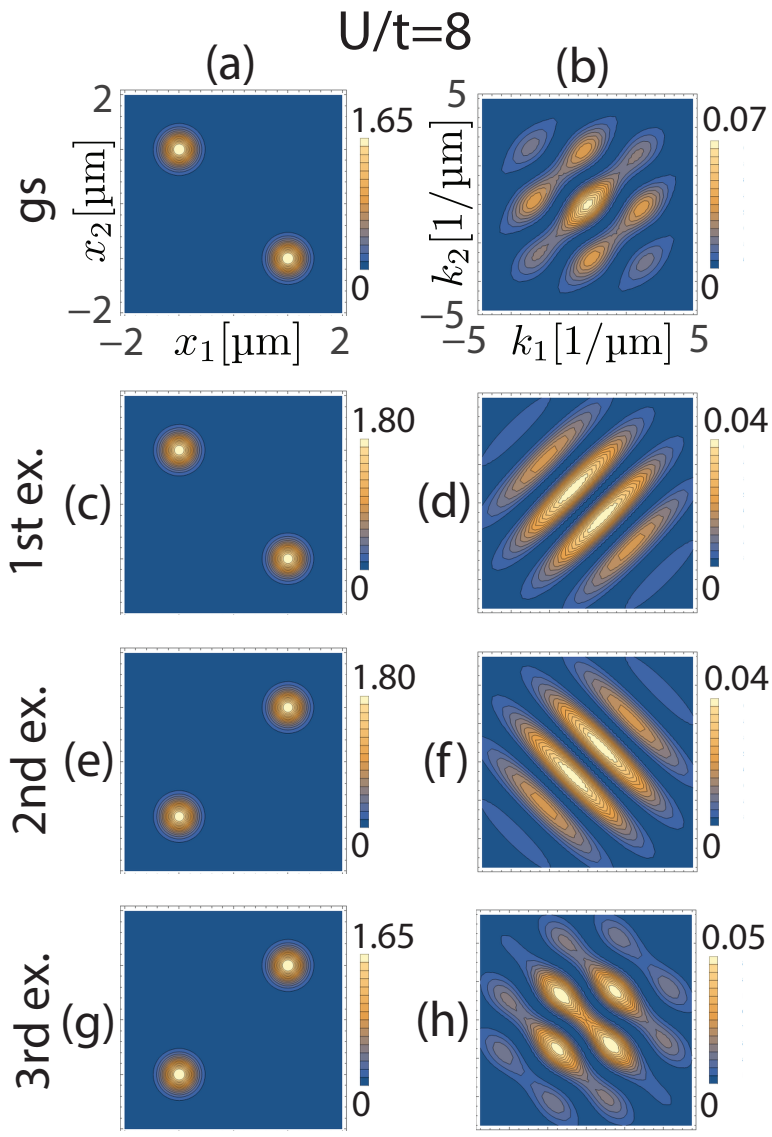

Figure 8.4: The left column shows the position space correlation function, the right column shows the momentum space correlation function. The parameters for our analytical correlation maps (which are based on the Hubbard model and displaced Gaussians) are $d = 2\,\mu\mathrm{m}$ (inter-well distance) and $s = 0.2\,\mu\mathrm{m}$ (Gaussian width).

Panels (a) and (b) in figure 8.4 represent the ground state position and momentum space correlation functions and should be compared with figure 8.1 panel (m) and (n). Panel (d)

in figure 8.4 should be compared with figure 8.3 panel (b), panel (f) in figure 8.4 should be compared with figure 8.3 panel (c) and panel (h) in figure 8.4 should be compared with figure 8.3 panel (e). The agreement in all these cases is excellent. Even though we don't show the corresponding CI results for the position space correlation maps of figure 8.4 we have checked that the agreement with the CI results in position space is excellent as well.

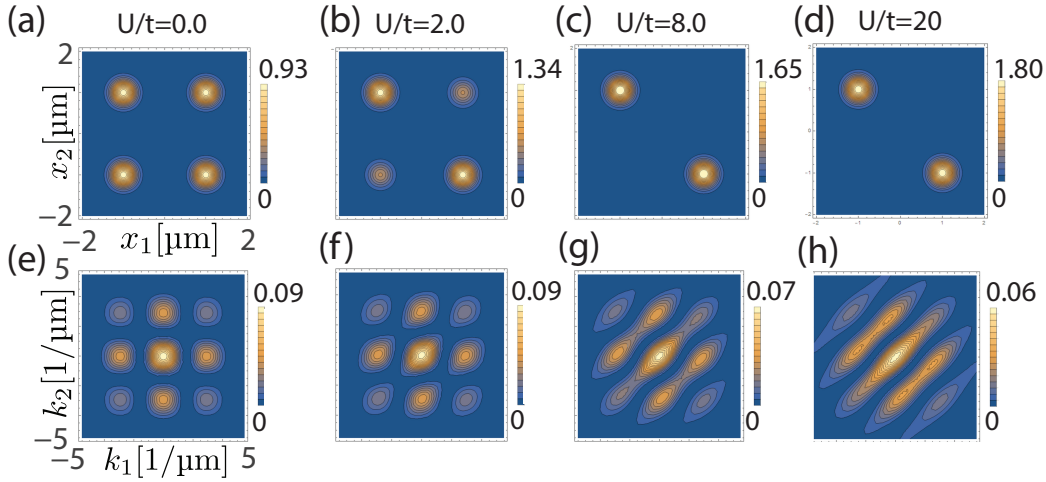

Figure 8.5: Ground state Hubbard model 2nd order position (first row) and momentum space (second row) correlation maps for varying interaction strengths. The value of U/t for which the plots were calculated is given above the panels. This figure should be compared with the bottom row in figure 8.1. The parameters for our analytical correlation maps (which are based on the Hubbard model and displaced Gaussians) are $d = 2\,\mu\mathrm{m}$ (inter-well distance) and $s = 0.2\,\mu\mathrm{m}$ (Gaussian width).

Furthermore we compared our analytic modeling results with the ground state CI results at varying interaction strength. The analytical correlation maps in position and momentum space are plotted in figure 8.5 and should be compared with the bottom row in figure 8.1. Again the analytical results are in excellent agreement with the microscopic CI calculations.

8.4 Connection between CPDs and position space correlation maps

Plots of the position space correlation function and the SR-CPD are closely related. Both visualize second-order correlations. For a SR-CPD we fix the spin and position of one particle and look for the resulting density of the other particles. We can obtain the same

information from our spin resolved position space correlation maps, by taking a vertical (fixing particle one) or horizontal (fixing particle two) cut in the correlation map. This is best explained by example.

Figure 8.5 panel (a) shows the position space correlation map for two **non-interacting** particles in a double well. The two wells are centered at $\pm 1\,\mu\mathrm{m}$. If we take a vertical cut at $x_1 = 1\,\mu\mathrm{m}$ we get a doubly humped density, that reflects the double -well nature of the system. If we take a vertical cut at $x_1 = 0\,\mu\mathrm{m}$ we don't see any features which is as expected since the inter-well barrier is high and no particles have any occupation probability in the middle. If we take a vertical cut $x_1 = -1\,\mu\mathrm{m}$ we again see two humps, corresponding to the double well. This is exactly the behavior we would see in a SR-CPD as well.

Figure 8.5 panel (d) shows the same double well system at **strong repulsion**. Naturally double occupancy is strongly suppressed. If we now take a vertical cut at $x_1 = 1\,\mu\mathrm{m}$ we only see a single hump at $x_2 = -1\,\mu\mathrm{m}$, reflecting the fact that the particles are occupying separate wells. If we take the vertical cut at $x_1 = -1\,\mu\mathrm{m}$ the single hump will be at $x_2 = 1\,\mu\mathrm{m}$. This is again in perfect agreement with what we would expect from plotting a SR-CPD.

In the case of quasi 1D systems we can therefore read off the SR-CPDs from the correlation maps. For 2D systems however the only feasible way to plot the second-order correlation functions is the use of SR-CPDs since the second-order correlation functions are a function of four variables (x_1, y_1, x_2, y_2) while the SR-CPDs are a function of two variables (x, y) for any given fixed point.

8.5 Connection to Hong-Ou-Mandel and Handbury-Brown-Twiss experiments

Some aspects of the ultracold atom experiments can be interpreted in terms of the famous Hong-Ou-Mandel experiment.

In the Hong-Ou-Mandel experiment bunching and antibunching of photons was observed [222] using two photons incident on opposite sides of a beam splitter and the ex-

periment was later extended to electrons [223, 224] and bosonic atoms [225]. A Hong-Ou-Mandel like bunching and antibunching effect should be observable with systems of ultracold atoms as well, as long as the interaction strength and the prepared state (ground state, 1st excited state, 2nd excited state, etc.) are appropriately chosen.

The connection of ultracold atom experiments to particle statistics dependent interference effects and fundamental questions in quantum mechanics is likely going to play an interesting role in the development and analysis of future ultracold atom experiments and will be particularly insightful once those experiments are able to measure the results for larger number of particles.

In addition to the results presented in this chapter our paper [124] shows additional plots of analytical correlation maps for negative interaction strengths, illustrates the double occupancy in the second excited states using SR-CPDs and provides the analytical density matrices for all four Hubbard model states.

Benedikt B. Brandt, Constantine Yannouleas, and Uzi Landman. "Interatomic interaction effects on second-order momentum correlations and Hong-Ou-Mandel interference of double-well-trapped ultracold fermionic atoms". In: *Physical Review A* 97.5 (May 4, 2018). arXiv: 1801.02295

LIST OF PUBLICATIONS

Benedikt B. Brandt, Constantine Yannouleas, and Uzi Landman. "Double-Well Ultracold-Fermions Computational Microscopy: Wave-Function Anatomy of Attractive-Pairing and Wigner-Molecule Entanglement and Natural Orbitals". In: *Nano Letters* (Sept. 9, 2015)

Constantine Yannouleas, Benedikt B Brandt, and Uzi Landman. "Ultracold few fermionic atoms in needle-shaped double wells: spin chains and resonating spin clusters from microscopic Hamiltonians emulated via antiferromagnetic Heisenberg and t-J models". In: *New Journal of Physics* 18.7 (July 8, 2016)

Benedikt B. Brandt, Constantine Yannouleas, and Uzi Landman. "Bottom-up configuration-interaction emulations of ultracold fermions in entangled optical plaquettes: building blocks of unconventional superconductivity". In: *Physical Review A* 95.4 (2017), p. 043617

Benedikt B. Brandt, Constantine Yannouleas, and Uzi Landman. "Two-point momentum correlations of few ultracold quasi-one-dimensional trapped fermions: Diffraction patterns". In: *Physical Review A* 96.5 (Nov. 30, 2017)

Benedikt B. Brandt, Constantine Yannouleas, and Uzi Landman. "Interatomic interaction effects on second-order momentum correlations and Hong-Ou-Mandel interference of double-well-trapped ultracold fermionic atoms". In: *Physical Review A* 97.5 (May 4, 2018). arXiv: 1801.02295

CHAPTER 9
CONCLUSION

Systems of ultracold atoms are one of the most versatile tools in condensed matter physics. Their applications range from the study of fundamental quantum mechanics and the realization of quantum simulators to practical applications in quantum information.

As we have shown in chapter 4 and chapter 5 of this thesis, ultracold atom systems are well suited to probe the many body wavefunction and its entanglement properties. We analyzed the wave function anatomy of two atoms in a double well, revealing interesting phenomena like the formation of Wigner Molecules and fermionization at strong repulsion. Furthermore, we studied the von Neuman entropy and the structure and occupation numbers of the natural orbitals for the full range of interaction strengths for select states. Moreover systems of ultracold atoms are well suited for the formation of spin chains, which enables the study of quantum magnetism. To that aim we studied three and four particle systems in different configurations and interpreted our results in the context of the well known Heisenberg and t-J model. Using our microscopic methodology, we assessed the accuracy and applicability of these spin models, provided insight into the wave function anatomy and demonstrated how the Wigner molecule formation is underlying the mapping to spin chains.

Furthermore we have shown in chapter 6 how systems of ultracold atoms can be used to observe the energetics of pairing in hole-doped plaquette systems. Such systems are believed to be at the heart of unconventional superconductivity and its underlying pairing mechanism. Using conditional probability densities and symmetry braking we directly observed the presence of hole pairing in the many body wavefunction. Our microscopic calculations provide essential guidance in the choice of parameters and demonstrate the shortcomings of the commonly used t-J and Hubbard model in certain parameter ranges.

Scaling plaquette systems to larger numbers of particles and sites will allow for fascinating insight into the still open question about the origin of high T_c superconductivity.

A third promising aspect of ultracold atom systems that was explored in this thesis in chapter 7 and chapter 8 is the study of second order correlation functions in position and momentum space. Recent experimental advances have made the second-order correlation functions directly accessible through time of flight measurements of ultracold atoms released from their traps. Measurements of such correlation functions can be interpreted in the context of the famous Hong-Ou-Mandel effect, which was first discovered and studied in quantum optics and allows for the probing of fundamental quantum statistics. We show detailed results for the full range of interaction strengths from the strongly attractive to the strongly repelling (Tonks–Girardeau) limit, for the ground and several excited states. We furthermore developed an analytical methodology for calculating the second order position and momentum space correlation functions from approximate models like the Hubbard model and confirmed their accuracy using our microscopic configuration interaction calculations.

Throughout this thesis we have demonstrated through various calculations the regions where ultracold atom systems are well approximated by spin models and where they show a more complex behavior, which necessitates guidance from microscopic CI calculations.

Future efforts of our group will include the study of higher order correlations, the impact of the particle statistics and a more detailed analysis of the entanglement properties in ultracold atom systems.

Realization of Feynman's vision of a quantum simulator that behaves just like nature seems to be in the not too distant future. Experimental advances leading to the control of larger numbers of particles and larger system sizes seem to be within reach. Such scaling of ultracold atom systems will allow for fascinating insights into some of the most important open questions in physics.

Appendices

APPENDIX A

A.1 Determination of Hubbard parameters from CI results

In order to compare our analytical model with the CI results it is important to relate the CI interaction strength g with the Hubbard parameter U and to extract the value of t from the external potential. Given the single particle basis spectrum the value of t can be extracted as $t = (E_2 - E_1)/2$ where E_1 and E_2 are the ground and first excited single particle energies respectively. This can be easily seen from a tight-binding calculation.

In order to determine U from the CI, we first need to take a close look at the Hubbard model energy levels and their properties. An exact diagonalization of the Hubbard Hamiltonian shows that the second excited state energy $E_3(U)$ is directly proportional to U with $E_3(U) = U + 2t + E_1(0)$, where $E_1(0)$ is the non-interacting ground state energy. For non-interacting ($U = 0$) particles the energy of the second excited state is therefore simply given as $E_3(0) = 2t + E_1(0)$. Consequently one can extract the parameter U directly from the difference between the non-interacting and interacting second excited state energy $U = E_3(U) - E_3(0)$. This is a trivial result within the Hubbard model but it extends nicely to our CI calculations.

In order to verify that we can use the same energy difference in our CI spectrum $U = E_3(g) - E_3(0)$ we look at the properties of the second excited CI state. In the Hubbard model the second excited state is given as $(|LL\rangle - |RR\rangle)/\sqrt{2}$, containing only doubly occupied sites (as we would expect since U represents the on-site interaction energy). It is easily verified via conditional probability densities (CPDs) that the second excited CI state consists of doubly occupied wells. We therefore proceed to determine U using $U = E_3(g) - E_3(0)$.

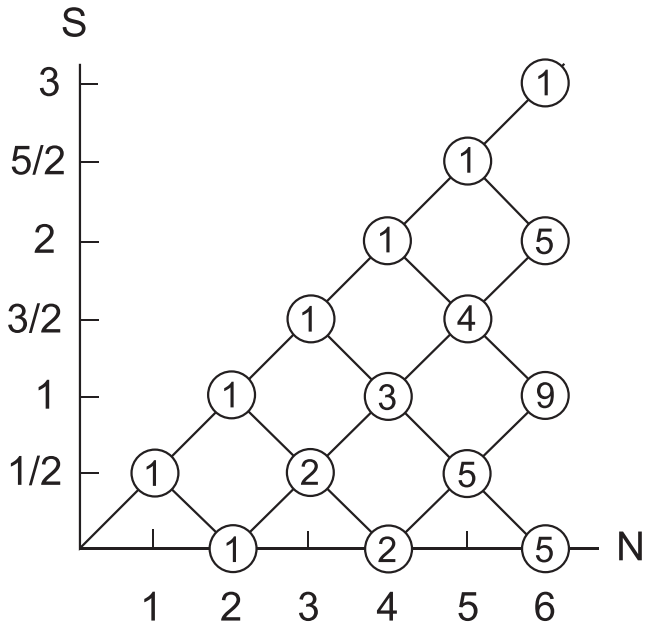

Figure A.1: The branching diagram of spin multiplicities. The x-axis represents the number of particles N, the y-axis the total spin quantum number S and the numbers in circles represent the number of spin functions there are for a particular combination of N and S. The total number of spin functions can be obtained by summing all the numbers in a column. For instance a system of four particles has 6 distinct spin functions in total.

A.2 Branching diagram

For more than two particles the classification of the spin functions according to the total spin S and the spin projection S_z ceases to be unique. This results in degeneracies in the spin functions for a particular total spin (i.e. there are multiple spin functions with the same total spin and the same spin projection). The branching diagram shown in figure A.1 indicates the multiplicity of total-spin S degeneracies for N spin 1/2 fermions. For instance for a three particle system (with spin projection $S_z = 0.5$) there are two spin functions with total spin $S = 0.5$ and one spin function with total spin $S = 1.5$.

More information can be found in [132, 226, 227].

APPENDIX B

USEFUL SNEG CODE

This chapter contains several useful pieces of code using SNEG.

B.1 SNEG code for the two-site Hubbard model

Listing B.1 gives the SNEG code for a two-site spin 1/2 Hubbard model. It illustrates the usage of SNEG and calculates the analytical eigenvalues and eigenvectors of the system.

```
1  Print["=== Loading SNEG... ==="];
2  currentdir = NotebookDirectory[];
3  SetDirectory[StringJoin[currentdir, "/sneg-1.234"]];
4  << sneg.m
5  SetDirectory[currentdir];
6
7  Print["=== Setting up Hubbard model ==="]
8  snegfermionoperators[c];
9  snegrealconstants[U, t, Psi1d, Psi1u, Psi2u, Psi2d];
10 Print["Hubbard model:"]
11 hubbardH = U (hubbard[c[1]] + hubbard[c[2]]) - t hop[c[1], c[2]]
12
13 Print["=== Setting up spin 1/2 basis ==="]
14 MatrixForm[hubbardbfull = qszbasisvc[{c[1], c[2]}]];
15 hubbardb = {hubbardbfull[[5]]}
16 Print["Hubbard basis in ket form:"]
17 Print[hubbardb[[1, 2]]]
18 Print["Hubbard basis in operator form:"]
19 Print[vc2ops[hubbardb[[1, 2]]]]
```

```
20
21 Print["=== Hubbard Hamiltonian in Matrix Form ==="]
22 hubbardm = matrixrepresentationvc[hubbardH, hubbardb[[1, 2]]];
23 hubbardm // MatrixForm
24 Print["Hamiltonian matrix is hermitian: ", HermitianMatrixQ[
      hubbardm]]
25 diagsolution = Eigensystem[hubbardm];
26 Print["Hubbard eigenenergies:"]
27 Print[diagsolution[[1]]]
28 Print["Hubbard eigenvectors:"]
29 Print[diagsolution[[2]]]
30 Print["Third Hubbard eigenvector with basis functions explicitly \
31 included:"]
32 Print["in ket notation:"]
33 Print[diagsolution[[2]][[3]].hubbardb[[1, 2]]]
34 Print["in second quantized notation:"]
35 Print[diagsolution[[2]][[3]].vc2ops[hubbardb[[1, 2]]]]
36
37 Print["=== Plot of Hubbard model eigenenergies ==="]
38 t = 1.;
39 Plot[diagsolution[[1]], {U, -8, 8}]
40 t =.;
```

Listing B.1: Mathematica Hubbard model solution and plot of the energy levels for two spin 1/2 particles on two sites using SNEG. In order to run this code the SNEG source code folder ”sneg-1.234” needs to be in the same directory as the Mathematica notebook containing this code.

B.2 SNEG code for large particle numbers

For a large number of sites running "qszbasisvc[...]" can be very slow (since the basises for all possible particle numbers and spin projections are constructed). In listing B.2 we give a performant method of how to create the SNEG basis functions for a particlular number of particles in the $S_z = 0$ spin projection.

```
Print["=== Loading SNEG... ==="];
currentdir = NotebookDirectory[];
SetDirectory[StringJoin[currentdir, "/sneg-1.234"]];
<< sneg.m
SetDirectory[currentdir];

snegfermionoperators[c];
n = 18
makebasis[Table[c[i], {i, 1, n}]]
% == BASIS
combinations = Subsets[Table[i, {i, 0, 2 n - 1}], {2}];
combinations =
 DeleteCases[combinations,
  x_ /; Mod[Total[x], 2] == 0](*delte non Sz=0 basis states*)
f[x_] := 2^x[[1]] + 2^x[[2]];
twoParticleBasisPositions = f /@ combinations;

g[x_] := BASIS IntegerDigits[x, 2, 2*n]
twoParticleBasisop = g /@ twoParticleBasisPositions;
twoParticleBasisop =
  Map[nc @@ Delete[#, Position[#, 0, 1]] &, twoParticleBasisop];

h[x_] := ap[x, VACUUM]
```

```
twoParticleBasisvc = h /@ twoParticleBasisop;

hubbardb = {{{-n + 2, 0}, twoParticleBasisvc}}
```

Listing B.2: Code to generate a basis in SNEG for a particular number of spin 1/2 particles and spin projection $S_z = 0$. The standard and simpler way of obtaining a basis is to use "qszbasisvc" however this call creates a basis set for all possible spin projections and all particle numbers for the given number of sites, which can take a long time if the number of sites is large. This code specifically creates the basis functions for the $S_z = 0$ spin projection for a particular number of particles.

REFERENCES

[1] Vladilen Letokhov. "Doppler line narrowing in a standing light wave." In: *JETP Lett.* 7 (1968), pp. 272–274.

[2] A. Ashkin. "Acceleration and Trapping of Particles by Radiation Pressure". In: *Physical Review Letters* 24.4 (Jan. 26, 1970), pp. 156–159. URL: https://link.aps.org/doi/10.1103/PhysRevLett.24.156.

[3] T.W. Hänsch and A.L. Schawlow. "Cooling of gases by laser radiation". In: *Optics Communications* 13.1 (Jan. 1975), pp. 68–69. URL: http://linkinghub.elsevier.com/retrieve/pii/0030401875901595.

[4] A. Ashkin. "Trapping of Atoms by Resonance Radiation Pressure". In: *Physical Review Letters* 40.12 (Mar. 20, 1978), pp. 729–732. URL: https://link.aps.org/doi/10.1103/PhysRevLett.40.729.

[5] J. E. Bjorkholm et al. "Observation of Focusing of Neutral Atoms by the Dipole Forces of Resonance-Radiation Pressure". In: *Physical Review Letters* 41.20 (Nov. 13, 1978), pp. 1361–1364. URL: https://link.aps.org/doi/10.1103/PhysRevLett.41.1361.

[6] John V. Prodan, William D. Phillips, and Harold Metcalf. "Laser Production of a Very Slow Monoenergetic Atomic Beam". In: *Physical Review Letters* 49.16 (Oct. 18, 1982), pp. 1149–1153. URL: https://link.aps.org/doi/10.1103/PhysRevLett.49.1149.

[7] Alan L. Migdall et al. "First Observation of Magnetically Trapped Neutral Atoms". In: *Physical Review Letters* 54.24 (June 17, 1985), pp. 2596–2599. URL: https://link.aps.org/doi/10.1103/PhysRevLett.54.2596.

[8] W. Ertmer et al. "Laser Manipulation of Atomic Beam Velocities: Demonstration of Stopped Atoms and Velocity Reversal". In: *Physical Review Letters* 54.10 (Mar. 11, 1985), pp. 996–999. URL: https://link.aps.org/doi/10.1103/PhysRevLett.54.996.

[9] Steven Chu et al. "Three-dimensional viscous confinement and cooling of atoms by resonance radiation pressure". In: *Physical Review Letters* 55.1 (July 1, 1985), pp. 48–51. URL: https://link.aps.org/doi/10.1103/PhysRevLett.55.48.

[10] Steven Chu et al. “Experimental Observation of Optically Trapped Atoms”. In: *Physical Review Letters* 57.3 (July 21, 1986), pp. 314–317. URL: https://link.aps.org/doi/10.1103/PhysRevLett.57.314.

[11] E. L. Raab et al. “Trapping of Neutral Sodium Atoms with Radiation Pressure”. In: *Physical Review Letters* 59.23 (Dec. 7, 1987), pp. 2631–2634. URL: https://link.aps.org/doi/10.1103/PhysRevLett.59.2631.

[12] Paul D. Lett et al. “Observation of Atoms Laser Cooled below the Doppler Limit”. In: *Physical Review Letters* 61.2 (July 11, 1988), pp. 169–172. URL: https://link.aps.org/doi/10.1103/PhysRevLett.61.169.

[13] J. Dalibard and C. Cohen-Tannoudji. “Laser cooling below the Doppler limit by polarization gradients: simple theoretical models”. In: *Journal of the Optical Society of America B* 6.11 (Nov. 1, 1989), p. 2023. URL: https://www.osapublishing.org/abstract.cfm?URI=josab-6-11-2023.

[14] A. Aspect et al. “Laser Cooling below the One-Photon Recoil Energy by Velocity-Selective Coherent Population Trapping”. In: *Physical Review Letters* 61.7 (Aug. 15, 1988), pp. 826–829. URL: https://link.aps.org/doi/10.1103/PhysRevLett.61.826.

[15] J. Lawall et al. “Two-Dimensional Subrecoil Laser Cooling”. In: *Physical Review Letters* 73.14 (Oct. 3, 1994), pp. 1915–1918. URL: https://link.aps.org/doi/10.1103/PhysRevLett.73.1915.

[16] J. Lawall et al. “Three-Dimensional Laser Cooling of Helium Beyond the Single-Photon Recoil Limit”. In: *Physical Review Letters* 75.23 (Dec. 4, 1995), pp. 4194–4197. URL: https://link.aps.org/doi/10.1103/PhysRevLett.75.4194.

[17] Nobelprize.org. *The Nobel Prize in Physics 1997 - Advanced Information*. 1997. URL: https://www.nobelprize.org/nobel_prizes/physics/laureates/1997/advanced.html (visited on 01/02/2018).

[18] C.S. Adams and E. Riis. “Laser cooling and trapping of neutral atoms”. In: *Progress in Quantum Electronics* 21.1 (Jan. 1997), pp. 1–79. URL: http://linkinghub.elsevier.com/retrieve/pii/S0079672796000067.

[19] Harold J. Metcalf and Peter van der Straten. “Laser Cooling and Trapping of Neutral Atoms”. In: *The Optics Encyclopedia*. Ed. by Thomas G. Brown et al. Weinheim, Germany: Wiley-VCH Verlag GmbH & Co. KGaA, July 15, 2007. ISBN: 978-3-527-60044-1. URL: http://doi.wiley.com/10.1002/9783527600441.oe005.

[20] William D. Phillips. “Nobel Lecture: Laser cooling and trapping of neutral atoms”. In: *Reviews of Modern Physics* 70.3 (July 1, 1998), pp. 721–741. URL: https://link.aps.org/doi/10.1103/RevModPhys.70.721.

[21] Alessio Celi et al. “Quantum optics and frontiers of physics: the third quantum revolution”. In: *Physica Scripta* 92.1 (Jan. 1, 2017), p. 013003. URL: http://stacks.iop.org/1402-4896/92/i=1/a=013003?key=crossref.1d2d860672d166faed2db4e6d4b217ab.

[22] Harald F. Hess. “Evaporative cooling of magnetically trapped and compressed spin-polarized hydrogen”. In: *Physical Review B* 34.5 (Sept. 1, 1986), pp. 3476–3479. URL: https://link.aps.org/doi/10.1103/PhysRevB.34.3476.

[23] Albert Einstein. “Quantum Theory of the Monatomic Ideal Gas”. In: *Sitzungsberichte der Preussischen Akademie der Wissenschaften, Physikalisch-mathematische Klasse* (1924), pp. 261–267.

[24] Albert Einstein. “Quantum Theory of the Monatomic Ideal Gas, Part II”. In: *Sitzungsberichte der Preussischen Akademie der Wissenschaften (Berlin), Physikalisch-mathematische Klasse* (1925), pp. 3–14.

[25] K. B. Davis et al. “Bose-Einstein Condensation in a Gas of Sodium Atoms”. In: *Physical Review Letters* 75.22 (Nov. 27, 1995), pp. 3969–3973. URL: https://link.aps.org/doi/10.1103/PhysRevLett.75.3969.

[26] M. H. Anderson et al. “Observation of Bose-Einstein Condensation in a Dilute Atomic Vapor”. In: *Science* 269.5221 (July 14, 1995), pp. 198–201. URL: http://www.sciencemag.org/cgi/doi/10.1126/science.269.5221.198.

[27] C. C. Bradley et al. “Evidence of Bose-Einstein Condensation in an Atomic Gas with Attractive Interactions”. In: *Physical Review Letters* 75.9 (Aug. 28, 1995), pp. 1687–1690. URL: https://link.aps.org/doi/10.1103/PhysRevLett.75.1687.

[28] L. P. Pitaevskiĭ and S. Stringari. *Bose-Einstein condensation*. Oxford science publications 116. Oxford ; New York: Clarendon Press, 2003. 382 pp. ISBN: 978-0-19-850719-2.

[29] L. P. Pitaevskii and S. Stringari. *Bose-Einstein condensation and superfluidity*. First edition. International series of monographs on physics 164. Oxford, United Kingdom: Oxford University Press, 2016. 553 pp. ISBN: 978-0-19-875888-4.

[30] Wolfgang Ketterle. “Nobel lecture: When atoms behave as waves: Bose-Einstein condensation and the atom laser”. In: *Reviews of Modern Physics* 74.4 (Nov. 20,

2002), pp. 1131–1151. URL: https://link.aps.org/doi/10.1103/RevModPhys.74.1131.

[31] Anthony J. Leggett. “Bose-Einstein condensation in the alkali gases: Some fundamental concepts”. In: *Reviews of Modern Physics* 73.2 (Apr. 24, 2001), pp. 307–356. URL: https://link.aps.org/doi/10.1103/RevModPhys.73.307.

[32] Franco Dalfovo et al. “Theory of Bose-Einstein condensation in trapped gases”. In: *Reviews of Modern Physics* 71.3 (Apr. 1, 1999), pp. 463–512. URL: https://link.aps.org/doi/10.1103/RevModPhys.71.463.

[33] B. DeMarco. “Onset of Fermi Degeneracy in a Trapped Atomic Gas”. In: *Science* 285.5434 (Sept. 10, 1999), pp. 1703–1706. URL: http://www.sciencemag.org/cgi/doi/10.1126/science.285.5434.1703.

[34] J. Bardeen, L. N. Cooper, and J. R. Schrieffer. “Theory of Superconductivity”. In: *Physical Review* 108.5 (Dec. 1, 1957), pp. 1175–1204. URL: https://link.aps.org/doi/10.1103/PhysRev.108.1175.

[35] Nobelprize.org. *The Nobel Prize in Physics 1972*. 1972. URL: https://www.nobelprize.org/nobel_prizes/physics/laureates/1972/ (visited on 01/03/2018).

[36] D. M. Eagles. “Possible Pairing without Superconductivity at Low Carrier Concentrations in Bulk and Thin-Film Superconducting Semiconductors”. In: *Physical Review* 186.2 (Oct. 10, 1969), pp. 456–463. URL: https://link.aps.org/doi/10.1103/PhysRev.186.456.

[37] Andrzej Pekalski and Jerzy A. Przystawa, eds. *Modern Trends in the Theory of Condensed Matter*. Vol. 115. Lecture Notes in Physics. Berlin, Heidelberg: Springer Berlin Heidelberg, 1980. ISBN: 978-3-540-09752-5 978-3-540-38628-5. URL: http://link.springer.com/10.1007/BFb0120123.

[38] Q Chen et al. “BCS–BEC crossover: From high temperature superconductors to ultracold superfluids”. In: *Physics Reports* 412.1 (June 2005), pp. 1–88. URL: http://linkinghub.elsevier.com/retrieve/pii/S0370157305001067.

[39] Mohit Randeria. “Pre-pairing for condensation: Ultracold Fermi gases”. In: *Nature Physics* 6.8 (Aug. 2010), pp. 561–562. URL: http://www.nature.com/articles/nphys1748.

[40] C. A. R. Sá de Melo, Mohit Randeria, and Jan R. Engelbrecht. “Crossover from BCS to Bose superconductivity: Transition temperature and time-dependent

Ginzburg-Landau theory". In: *Physical Review Letters* 71.19 (Nov. 8, 1993), pp. 3202–3205. URL: https://link.aps.org/doi/10.1103/PhysRevLett.71.3202.

[41] K. M. O'Hara. "Observation of a Strongly Interacting Degenerate Fermi Gas of Atoms". In: *Science* 298.5601 (Dec. 13, 2002), pp. 2179–2182. URL: http://www.sciencemag.org/cgi/doi/10.1126/science.1079107.

[42] C. Chin. "Observation of the Pairing Gap in a Strongly Interacting Fermi Gas". In: *Science* 305.5687 (Aug. 20, 2004), pp. 1128–1130. URL: http://www.sciencemag.org/cgi/doi/10.1126/science.1100818.

[43] Markus Greiner, Cindy A. Regal, and Deborah S. Jin. "Emergence of a molecular Bose–Einstein condensate from a Fermi gas". In: *Nature* 426.6966 (Dec. 4, 2003), pp. 537–540. URL: http://www.nature.com/doifinder/10.1038/nature02199.

[44] S. Jochim. "Bose-Einstein Condensation of Molecules". In: *Science* 302.5653 (Dec. 19, 2003), pp. 2101–2103. URL: http://www.sciencemag.org/cgi/doi/10.1126/science.1093280.

[45] M. W. Zwierlein et al. "Observation of Bose-Einstein Condensation of Molecules". In: *Physical Review Letters* 91.25 (Dec. 15, 2003). URL: https://link.aps.org/doi/10.1103/PhysRevLett.91.250401.

[46] Cindy A. Regal et al. "Creation of ultracold molecules from a Fermi gas of atoms". In: *Nature* 424.6944 (July 3, 2003), pp. 47–50. URL: http://www.nature.com/doifinder/10.1038/nature01738.

[47] M. W. Zwierlein et al. "Condensation of Pairs of Fermionic Atoms near a Feshbach Resonance". In: *Physical Review Letters* 92.12 (Mar. 25, 2004). URL: https://link.aps.org/doi/10.1103/PhysRevLett.92.120403.

[48] C. A. Regal, M. Greiner, and D. S. Jin. "Observation of Resonance Condensation of Fermionic Atom Pairs". In: *Physical Review Letters* 92.4 (Jan. 28, 2004). URL: https://link.aps.org/doi/10.1103/PhysRevLett.92.040403.

[49] Immanuel Bloch, Jean Dalibard, and Wilhelm Zwerger. "Many-body physics with ultracold gases". In: *Reviews of Modern Physics* 80.3 (July 18, 2008), pp. 885–964. URL: https://link.aps.org/doi/10.1103/RevModPhys.80.885.

[50] Stefano Giorgini, Lev P. Pitaevskii, and Sandro Stringari. "Theory of ultracold atomic Fermi gases". In: *Reviews of Modern Physics* 80.4 (Oct. 2, 2008), pp. 1215–1274. URL: https://link.aps.org/doi/10.1103/RevModPhys.80.1215.

[51] U. Fano. “Effects of Configuration Interaction on Intensities and Phase Shifts”. In: *Physical Review* 124.6 (Dec. 15, 1961), pp. 1866–1878. URL: https://link.aps.org/doi/10.1103/PhysRev.124.1866.

[52] Herman Feshbach. “A unified theory of nuclear reactions. II”. In: *Annals of Physics* 19.2 (Aug. 1962), pp. 287–313. URL: http://linkinghub.elsevier.com/retrieve/pii/000349166290221X.

[53] Cheng Chin et al. “Feshbach resonances in ultracold gases”. In: *Reviews of Modern Physics* 82.2 (Apr. 29, 2010), pp. 1225–1286. URL: http://link.aps.org/doi/10.1103/RevModPhys.82.1225.

[54] Richard P. Feynman. “Simulating physics with computers”. In: *International journal of theoretical physics* 21.6 (1982), pp. 467–488. URL: http://www.springerlink.com/index/t2x8115127841630.pdf.

[55] Richard P. Feynman. “Quantum Mechanical Computers”. In: *Optics News* 11.2 (Feb. 1, 1985), p. 11. URL: https://www.osapublishing.org/abstract.cfm?URI=on-11-2-11.

[56] P. S. Jessen et al. “Observation of quantized motion of Rb atoms in an optical field”. In: *Physical Review Letters* 69.1 (July 6, 1992), pp. 49–52. URL: https://link.aps.org/doi/10.1103/PhysRevLett.69.49.

[57] G. Grynberg et al. “Quantized motion of cold cesium atoms in two- and three-dimensional optical potentials”. In: *Physical Review Letters* 70.15 (Apr. 12, 1993), pp. 2249–2252. URL: https://link.aps.org/doi/10.1103/PhysRevLett.70.2249.

[58] P. Verkerk et al. “Dynamics and spatial order of cold cesium atoms in a periodic optical potential”. In: *Physical Review Letters* 68.26 (June 29, 1992), pp. 3861–3864. URL: https://link.aps.org/doi/10.1103/PhysRevLett.68.3861.

[59] A. Hemmerich and T. W. Hänsch. “Two-dimesional atomic crystal bound by light”. In: *Physical Review Letters* 70.4 (Jan. 25, 1993), pp. 410–413. URL: https://link.aps.org/doi/10.1103/PhysRevLett.70.410.

[60] G. Birkl et al. “Bragg Scattering from Atoms in Optical Lattices”. In: *Physical Review Letters* 75.15 (Oct. 9, 1995), pp. 2823–2826. URL: https://link.aps.org/doi/10.1103/PhysRevLett.75.2823.

[61] Matthias Weidemüller et al. “Bragg Diffraction in an Atomic Lattice Bound by Light”. In: *Physical Review Letters* 75.25 (Dec. 18, 1995), pp. 4583–4586. URL: https://link.aps.org/doi/10.1103/PhysRevLett.75.4583.

[62] Maxime Ben Dahan et al. “Bloch Oscillations of Atoms in an Optical Potential”. In: *Physical Review Letters* 76.24 (June 10, 1996), pp. 4508–4511. URL: https://link.aps.org/doi/10.1103/PhysRevLett.76.4508.

[63] S. R. Wilkinson et al. “Observation of Atomic Wannier-Stark Ladders in an Accelerating Optical Potential”. In: *Physical Review Letters* 76.24 (June 10, 1996), pp. 4512–4515. URL: https://link.aps.org/doi/10.1103/PhysRevLett.76.4512.

[64] B. P. Anderson. “Macroscopic Quantum Interference from Atomic Tunnel Arrays”. In: *Science* 282.5394 (Nov. 27, 1998), pp. 1686–1689. URL: http://www.sciencemag.org/cgi/doi/10.1126/science.282.5394.1686.

[65] C. Orzel. “Squeezed States in a Bose-Einstein Condensate”. In: *Science* 291.5512 (Mar. 23, 2001), pp. 2386–2389. URL: http://www.sciencemag.org/cgi/doi/10.1126/science.1058149.

[66] Oliver Morsch and Markus Oberthaler. “Dynamics of Bose-Einstein condensates in optical lattices”. In: *Reviews of Modern Physics* 78.1 (Feb. 27, 2006), pp. 179–215. URL: https://link.aps.org/doi/10.1103/RevModPhys.78.179.

[67] D. Jaksch et al. “Cold Bosonic Atoms in Optical Lattices”. In: *Physical Review Letters* 81.15 (Oct. 12, 1998), pp. 3108–3111. URL: https://link.aps.org/doi/10.1103/PhysRevLett.81.3108.

[68] Markus Greiner et al. “Quantum phase transition from a superfluid to a Mott insulator in a gas of ultracold atoms”. In: *nature* 415.6867 (2002), pp. 39–44. URL: http://www.nature.com/nature/journal/v415/n6867/abs/415039a.html.

[69] L. Fallani et al. “Ultracold Atoms in a Disordered Crystal of Light: Towards a Bose Glass”. In: *Physical Review Letters* 98.13 (Mar. 30, 2007). URL: https://link.aps.org/doi/10.1103/PhysRevLett.98.130404.

[70] Thilo Stöferle et al. “Transition from a Strongly Interacting 1D Superfluid to a Mott Insulator”. In: *Physical Review Letters* 92.13 (Mar. 31, 2004). URL: https://link.aps.org/doi/10.1103/PhysRevLett.92.130403.

[71] S. Ospelkaus et al. “Localization of Bosonic Atoms by Fermionic Impurities in a Three-Dimensional Optical Lattice”. In: *Physical Review Letters* 96.18 (May 9, 2006). URL: https://link.aps.org/doi/10.1103/PhysRevLett.96.180403.

[72] Kenneth Günter et al. “Bose-Fermi Mixtures in a Three-Dimensional Optical Lattice”. In: *Physical Review Letters* 96.18 (May 9, 2006). URL: https://link.aps.org/doi/10.1103/PhysRevLett.96.180402.

[73] Michael Köhl et al. “Fermionic Atoms in a Three Dimensional Optical Lattice: Observing Fermi Surfaces, Dynamics, and Interactions”. In: *Physical Review Letters* 94.8 (Mar. 4, 2005). URL: https://link.aps.org/doi/10.1103/PhysRevLett.94.080403.

[74] U. Schneider et al. “Metallic and Insulating Phases of Repulsively Interacting Fermions in a 3D Optical Lattice”. In: *Science* 322.5907 (Dec. 5, 2008), pp. 1520–1525. URL: http://www.sciencemag.org/cgi/doi/10.1126/science.1165449.

[75] Robert Jördens et al. “A Mott insulator of fermionic atoms in an optical lattice”. In: *Nature* 455.7210 (Sept. 11, 2008), pp. 204–207. URL: http://www.nature.com/doifinder/10.1038/nature07244.

[76] Y.-J. Lin et al. “Synthetic magnetic fields for ultracold neutral atoms”. In: *Nature* 462.7273 (Dec. 3, 2009), pp. 628–632. URL: http://www.nature.com/doifinder/10.1038/nature08609.

[77] R. Jördens et al. “Quantitative Determination of Temperature in the Approach to Magnetic Order of Ultracold Fermions in an Optical Lattice”. In: *Physical Review Letters* 104.18 (May 6, 2010). URL: https://link.aps.org/doi/10.1103/PhysRevLett.104.180401.

[78] N. Levy et al. “Strain-Induced Pseudo-Magnetic Fields Greater Than 300 Tesla in Graphene Nanobubbles”. In: *Science* 329.5991 (July 30, 2010), pp. 544–547. URL: http://www.sciencemag.org/cgi/doi/10.1126/science.1191700.

[79] S. Trotzky et al. “Suppression of the critical temperature for superfluidity near the Mott transition”. In: *Nature Physics* 6.12 (Dec. 2010), pp. 998–1004. URL: http://www.nature.com/doifinder/10.1038/nphys1799.

[80] Immanuel Bloch, Jean Dalibard, and Sylvain Nascimbène. “Quantum simulations with ultracold quantum gases”. In: *Nature Physics* 8.4 (Apr. 2, 2012), pp. 267–276. URL: http://www.nature.com/doifinder/10.1038/nphys2259.

[81] Belén Paredes et al. “Tonks–Girardeau gas of ultracold atoms in an optical lattice”. In: *Nature* 429.6989 (May 20, 2004), pp. 277–281. URL: http://www.nature.com/doifinder/10.1038/nature02530.

[82] J M Kosterlitz and D J Thouless. “Ordering, metastability and phase transitions in two-dimensional systems”. In: *Journal of Physics C: Solid State Physics* 6.7 (Apr. 12, 1973), pp. 1181–1203. URL: http://stacks.iop.org/0022-3719/6/i=7/a=010?key=crossref.f2d443370878b9288c142e398ad429b1.

[83] D. J. Bishop and J. D. Reppy. “Study of the Superfluid Transition in Two-Dimensional He 4 Films”. In: *Physical Review Letters* 40.26 (June 26, 1978), pp. 1727–1730. URL: https://link.aps.org/doi/10.1103/PhysRevLett.40.1727.

[84] D. J. Bishop and J. D. Reppy. “Study of the superfluid transition in two-dimensional He 4 films”. In: *Physical Review B* 22.11 (Dec. 1, 1980), pp. 5171–5185. URL: https://link.aps.org/doi/10.1103/PhysRevB.22.5171.

[85] Zoran Hadzibabic et al. “Berezinskii–Kosterlitz–Thouless crossover in a trapped atomic gas”. In: *Nature* 441.7097 (June 2006), pp. 1118–1121. URL: http://www.nature.com/articles/nature04851.

[86] Nobelprize.org. *The Nobel Prize in Physics 2016*. 2016. URL: https://www.nobelprize.org/nobel_prizes/physics/laureates/2016/ (visited on 01/05/2018).

[87] Jonathan Simon et al. “Quantum simulation of antiferromagnetic spin chains in an optical lattice”. In: *Nature* 472.7343 (Apr. 21, 2011), pp. 307–312. URL: http://www.nature.com/doifinder/10.1038/nature09994.

[88] J. J. García-Ripoll, M. A. Martin-Delgado, and J. I. Cirac. “Implementation of Spin Hamiltonians in Optical Lattices”. In: *Physical Review Letters* 93.25 (Dec. 15, 2004). URL: http://link.aps.org/doi/10.1103/PhysRevLett.93.250405.

[89] Russell A. Hart et al. “Observation of antiferromagnetic correlations in the Hubbard model with ultracold atoms”. In: *Nature* 519.7542 (Feb. 23, 2015), pp. 211–214. URL: http://www.nature.com/doifinder/10.1038/nature14223.

[90] Martin Boll et al. “Spin-and density-resolved microscopy of antiferromagnetic correlations in Fermi-Hubbard chains”. In: *Science* 353.6305 (2016), pp. 1257–1260. URL: http://science.sciencemag.org/content/353/6305/1257.short.

[91] M. F. Parsons et al. “Site-resolved measurement of the spin-correlation function in the Fermi-Hubbard model”. In: *Science* 353.6305 (Sept. 16, 2016), pp. 1253–1256.

URL: http://www.sciencemag.org/cgi/doi/10.1126/science.aag1430.

[92] N Goldman et al. "Light-induced gauge fields for ultracold atoms". In: *Reports on Progress in Physics* 77.12 (Dec. 1, 2014), p. 126401. URL: http://stacks.iop.org/0034-4885/77/i=12/a=126401?key=crossref.215014e4d266d4dc153d5445fad5981b.

[93] Marco Anderlini et al. "Controlled exchange interaction between pairs of neutral atoms in an optical lattice". In: *Nature* 448.7152 (July 26, 2007), pp. 452–456. URL: http://www.nature.com/doifinder/10.1038/nature06011.

[94] Antonio Negretti, Philipp Treutlein, and Tommaso Calarco. "Quantum computing implementations with neutral particles". In: *Quantum Information Processing* 10.6 (Dec. 2011), pp. 721–753. URL: http://link.springer.com/10.1007/s11128-011-0291-5.

[95] D. Jaksch and P. Zoller. "The cold atom Hubbard toolbox". In: *Annals of Physics* 315.1 (Jan. 2005), pp. 52–79. URL: http://linkinghub.elsevier.com/retrieve/pii/S0003491604001782.

[96] S. Nascimbène et al. "Experimental Realization of Plaquette Resonating Valence-Bond States with Ultracold Atoms in Optical Superlattices". In: *Physical Review Letters* 108.20 (May 14, 2012). URL: http://link.aps.org/doi/10.1103/PhysRevLett.108.205301.

[97] F. Serwane et al. "Deterministic Preparation of a Tunable Few-Fermion System". In: *Science* 332.6027 (Apr. 15, 2011), pp. 336–338. URL: http://www.sciencemag.org/cgi/doi/10.1126/science.1201351.

[98] G. Zürn et al. "Fermionization of two distinguishable fermions". In: *Physical review letters* 108.7 (2012), p. 075303. URL: http://prl.aps.org/abstract/PRL/v108/i7/e075303.

[99] Simon Murmann et al. "Two Fermions in a Double Well: Exploring a Fundamental Building Block of the Hubbard Model". In: *Physical Review Letters* 114.8 (Feb. 23, 2015). URL: http://link.aps.org/doi/10.1103/PhysRevLett.114.080402.

[100] Simon Murmann et al. "Antiferromagnetic Heisenberg spin chain of few cold atoms in a one-dimensional trap". In: *arXiv preprint arXiv:1507.01117* (2015). URL: http://arxiv.org/abs/1507.01117.

[101] Immanuel Bloch. “Ultracold quantum gases in optical lattices”. In: *Nature Physics* 1.1 (2005), pp. 23–30. URL: http://www.nature.com/nphys/journal/v1/n1/abs/nphys138.html.

[102] A. Ashkin. “History of optical trapping and manipulation of small-neutral particle, atoms, and molecules”. In: *IEEE Journal of Selected Topics in Quantum Electronics* 6.6 (Nov. 2000), pp. 841–856. URL: http://ieeexplore.ieee.org/document/902132/.

[103] Keir C. Neuman and Steven M. Block. “Optical trapping”. In: *Review of Scientific Instruments* 75.9 (Sept. 2004), pp. 2787–2809. URL: http://aip.scitation.org/doi/10.1063/1.1785844.

[104] Thomas Busch et al. “Two cold atoms in a harmonic trap”. In: *Foundations of Physics* 28.4 (1998), pp. 549–559. URL: http://link.springer.com/article/10.1023/A:1018705520999.

[105] A. N. Wenz et al. “From Few to Many: Observing the Formation of a Fermi Sea One Atom at a Time”. In: *Science* 342.6157 (2013), pp. 457–460. URL: http://www.sciencemag.org/content/342/6157/457.short.

[106] A. M. Kaufman et al. “Two-particle quantum interference in tunnel-coupled optical tweezers”. In: *science* 345.6194 (2014), pp. 306–309. URL: http://www.sciencemag.org/content/345/6194/306.short.

[107] A. M. Kaufman et al. “Entangling two transportable neutral atoms via local spin exchange”. In: *Nature* 527.7577 (Nov. 2015), pp. 208–211. URL: http://www.nature.com/articles/nature16073.

[108] Tilman Esslinger. “Fermi-Hubbard Physics with Atoms in an Optical Lattice”. In: *Annual Review of Condensed Matter Physics* 1.1 (Aug. 10, 2010), pp. 129–152. URL: http://www.annualreviews.org/doi/10.1146/annurev-conmatphys-070909-104059.

[109] F. Deuretzbacher et al. “Exact Solution of Strongly Interacting Quasi-One-Dimensional Spinor Bose Gases”. In: *Physical Review Letters* 100.16 (Apr. 23, 2008). URL: https://link.aps.org/doi/10.1103/PhysRevLett.100.160405.

[110] Xiaoling Cui and Tin-Lun Ho. “Ground-state ferromagnetic transition in strongly repulsive one-dimensional Fermi gases”. In: *Physical Review A* 89.2 (Feb. 13, 2014). URL: https://link.aps.org/doi/10.1103/PhysRevA.89.023611.

[111] F. Deuretzbacher et al. “Quantum magnetism without lattices in strongly interacting one-dimensional spinor gases”. In: *Physical Review A* 90.1 (July 14, 2014). URL: http://link.aps.org/doi/10.1103/PhysRevA.90.013611.

[112] J. Levinsen et al. “Strong-coupling ansatz for the one-dimensional Fermi gas in a harmonic potential”. In: *Science Advances* 1.6 (July 1, 2015), e1500197–e1500197. URL: http://advances.sciencemag.org/cgi/doi/10.1126/sciadv.1500197.

[113] Liming Guan et al. “Exact Solution for Infinitely Strongly Interacting Fermi Gases in Tight Waveguides”. In: *Physical Review Letters* 102.16 (Apr. 22, 2009). URL: http://link.aps.org/doi/10.1103/PhysRevLett.102.160402.

[114] M. D. Girardeau and A. Minguzzi. “Soluble Models of Strongly Interacting Ultracold Gas Mixtures in Tight Waveguides”. In: *Physical Review Letters* 99.23 (Dec. 5, 2007). URL: https://link.aps.org/doi/10.1103/PhysRevLett.99.230402.

[115] M. D. Girardeau. “Two super-Tonks-Girardeau states of a trapped one-dimensional spinor Fermi gas”. In: *Physical Review A* 82.1 (July 20, 2010). URL: https://link.aps.org/doi/10.1103/PhysRevA.82.011607.

[116] Seyed Ebrahim Gharashi and D. Blume. “Correlations of the Upper Branch of 1D Harmonically Trapped Two-Component Fermi Gases”. In: *Physical Review Letters* 111.4 (July 24, 2013). URL: http://link.aps.org/doi/10.1103/PhysRevLett.111.045302.

[117] Seyed Ebrahim Gharashi, K. M. Daily, and D. Blume. “Three s -wave-interacting fermions under anisotropic harmonic confinement: Dimensional crossover of energetics and virial coefficients”. In: *Physical Review A* 86.4 (Oct. 4, 2012). URL: http://link.aps.org/doi/10.1103/PhysRevA.86.042702.

[118] X. Y. Yin and D. Blume. “Trapped unitary two-component Fermi gases with up to ten particles”. In: *Physical Review A* 92.1 (July 6, 2015). URL: http://link.aps.org/doi/10.1103/PhysRevA.92.013608.

[119] Atilla Szabo and Neil S. Ostlund. *Modern Quantum Chemistry: Introduction to Advanced Electronic Structure Theory*. 1996. URL: http://store.doverpublications.com/0486691861.html.

[120] Benedikt B. Brandt, Constantine Yannouleas, and Uzi Landman. “Double-Well Ultracold-Fermions Computational Microscopy: Wave-Function Anatomy of Attractive-Pairing and Wigner-Molecule Entanglement and Natural Orbitals”. In: *Nano Letters* 15.10 (Oct. 14, 2015), pp. 7105–7111. URL: http://pubs.acs.org/doi/10.1021/acs.nanolett.5b03199.

[121] Constantine Yannouleas, Benedikt B Brandt, and Uzi Landman. "Ultracold few fermionic atoms in needle-shaped double wells: spin chains and resonating spin clusters from microscopic Hamiltonians emulated via antiferromagnetic Heisenberg and t-J models". In: *New Journal of Physics* 18.7 (July 8, 2016). URL: http://stacks.iop.org/1367-2630/18/i=7/a=073018?key=crossref.fad4ffd3403388f4488bd02efa45b163.

[122] Benedikt B. Brandt, Constantine Yannouleas, and Uzi Landman. "Bottom-up configuration-interaction emulations of ultracold fermions in entangled optical plaquettes: building blocks of unconventional superconductivity". In: *Physical Review A* 95.4 (2017), p. 043617. URL: https://journals.aps.org/pra/abstract/10.1103/PhysRevA.95.043617.

[123] Benedikt B. Brandt, Constantine Yannouleas, and Uzi Landman. "Two-point momentum correlations of few ultracold quasi-one-dimensional trapped fermions: Diffraction patterns". In: *Physical Review A* 96.5 (Nov. 30, 2017). URL: https://link.aps.org/doi/10.1103/PhysRevA.96.053632.

[124] Benedikt B. Brandt, Constantine Yannouleas, and Uzi Landman. "Interatomic interaction effects on second-order momentum correlations and Hong-Ou-Mandel interference of double-well-trapped ultracold fermionic atoms". In: *Physical Review A* 97.5 (May 4, 2018). arXiv: 1801.02295. URL: http://arxiv.org/abs/1801.02295.

[125] Barry P. Martins. *Frontiers in superconductivity research*. Nova Publishers, 2003.

[126] M. Casas et al. "Cooper pairing in a soluble one-dimensional many-fermion model". In: *Physical Review A* 44.8 (Oct. 1, 1991), pp. 4915–4922. URL: https://link.aps.org/doi/10.1103/PhysRevA.44.4915.

[127] Rostislav A. Doganov et al. "Two trapped particles interacting by a finite-range two-body potential in two spatial dimensions". In: *Physical Review A* 87.3 (Mar. 28, 2013). URL: http://link.aps.org/doi/10.1103/PhysRevA.87.033631.

[128] Pere Mujal et al. "Quantum correlations and degeneracy of identical bosons in a two-dimensional harmonic trap". In: *Physical Review A* 96.4 (Oct. 16, 2017). URL: https://link.aps.org/doi/10.1103/PhysRevA.96.043614.

[129] Joanna Jankowska and Zbigniew Idziaszek. "Reactive collisions of two ultracold particles in a harmonic trap". In: *Physical Review A* 93.5 (May 23, 2016). URL: https://link.aps.org/doi/10.1103/PhysRevA.93.052714.

[130] Javier von Stecher and Chris H. Greene. "Spectrum and Dynamics of the BCS-BEC Crossover from a Few-Body Perspective". In: *Physical Review Letters* 99.9

(Aug. 31, 2007). URL: https://link.aps.org/doi/10.1103/PhysRevLett.99.090402.

[131] Raphael Beinke et al. "Many-body tunneling dynamics of Bose-Einstein condensates and vortex states in two spatial dimensions". In: *Physical Review A* 92.4 (Oct. 27, 2015). URL: https://link.aps.org/doi/10.1103/PhysRevA.92.043627.

[132] Ying Li, Constantine Yannouleas, and Uzi Landman. "Artificial quantum-dot helium molecules: Electronic spectra, spin structures, and Heisenberg clusters". In: *Physical Review B* 80.4 (July 2009). URL: http://link.aps.org/doi/10.1103/PhysRevB.80.045326.

[133] Benedikt B. Brandt, Constantine Yannouleas, and Uzi Landman. "Double-Well Ultracold-Fermions Computational Microscopy: Wave-Function Anatomy of Attractive-Pairing and Wigner-Molecule Entanglement and Natural Orbitals". In: *Nano Letters* (Sept. 9, 2015). URL: http://pubs.acs.org/doi/10.1021/acs.nanolett.5b03199.

[134] Constantine Yannouleas and Uzi Landman. "Spontaneous symmetry breaking in single and molecular quantum dots". In: *Physical review letters* 82.26 (1999), p. 5325. URL: http://prl.aps.org/abstract/PRL/v82/i26/p5325_1.

[135] Constantine Yannouleas and Uzi Landman. "Symmetry breaking and quantum correlations in finite systems: studies of quantum dots and ultracold Bose gases and related nuclear and chemical methods". In: *Reports on Progress in Physics* 70.12 (Dec. 1, 2007), pp. 2067–2148. URL: http://stacks.iop.org/0034-4885/70/i=12/a=R02?key=crossref.a87571c73f468fd22015f9bd887ae1fa.

[136] T. A. Driscoll, N. Hale, and L. N. Trefethen. *Chebfun Guide*. Oxford: Pafnuty Publications, 2014.

[137] Andrea Bergschneider. "Strong correlations in few-fermion systems". PhD thesis. 2017.

[138] Andrea Bergschneider. "Studying strongly correlated few-fermion systems with ultracold atoms". Jan. 17, 2018. URL: https://theorie.ikp.physik.tu-darmstadt.de/hirschegg/2018/program.php.

[139] Huoy-Jen Yuh et al. "Electron Correlation and Kellman-Herrick Quantization in Doubly Excited Helium". In: *Physical Review Letters* 47.7 (Aug. 17, 1981), pp. 497–500. URL: http://link.aps.org/doi/10.1103/PhysRevLett.47.497.

[140] Gregory S. Ezra and R. Stephen Berry. “Collective and independent-particle motion in doubly excited two-electron atoms”. In: *Physical Review A* 28.4 (1983), p. 1974. URL: http://journals.aps.org/pra/abstract/10.1103/PhysRevA.28.1974.

[141] R. Stephen Berry. “How good is Niels Bohr’s atomic model?” In: *Contemporary Physics* 30.1 (Jan. 1989), pp. 1–19. URL: http://www.tandfonline.com/doi/abs/10.1080/00107518908222587.

[142] Constantine Yannouleas and Uzi Landman. “Collective and independent-particle motion in two-electron artificial atoms”. In: *Physical review letters* 85.8 (2000), p. 1726. URL: http://prl.aps.org/abstract/PRL/v85/i8/p1726_1.

[143] Per-Olov Löwdin. “Quantum theory of many-particle systems. I. Physical interpretations by means of density matrices, natural spin-orbitals, and convergence problems in the method of configurational interaction”. In: *Physical Review* 97.6 (1955), p. 1474. URL: https://journals.aps.org/pr/abstract/10.1103/PhysRev.97.1474.

[144] Per-Olov Löwdin and Harrison Shull. “Natural orbitals in the quantum theory of two-electron systems”. In: *Physical Review* 101.6 (1956), p. 1730. URL: http://journals.aps.org/pr/abstract/10.1103/PhysRev.101.1730.

[145] John von Neumann. *Mathematische Grundlagen der Quantenmechanik*. Berlin, Heidelberg: Springer Berlin Heidelberg, 1996. ISBN: 978-3-642-64828-1 978-3-642-61409-5. URL: http://link.springer.com/10.1007/978-3-642-61409-5.

[146] A. John Coleman. “Structure of fermion density matrices”. In: *Reviews of modern Physics* 35.3 (1963), p. 668. URL: https://journals.aps.org/rmp/abstract/10.1103/RevModPhys.35.668.

[147] Benedikt B. Brandt, Constantine Yannouleas, and Uzi Landman. “Interaction-strength evolution of two-particle momentum correlation maps of two ultracold fermions in a double well”. In: *arXiv preprint arXiv:1801.02295* (2018).

[148] *Mixed states and pure states*. URL: http://pages.uoregon.edu/svanenk/solutions/Mixed_states.pdf.

[149] J. Hubbard. “Electron Correlations in Narrow Energy Bands”. In: *Proceedings of the Royal Society A: Mathematical, Physical and Engineering Sciences* 276.1365 (Nov. 26, 1963), pp. 238–257. URL: http://rspa.royalsocietypublishing.org/cgi/doi/10.1098/rspa.1963.0204.

[150] J. Hubbard. “Electron Correlations in Narrow Energy Bands. II. The Degenerate Band Case”. In: *Proceedings of the Royal Society A: Mathematical, Physical and Engineering Sciences* 277.1369 (Jan. 21, 1964), pp. 237–259. URL: http://rspa.royalsocietypublishing.org/cgi/doi/10.1098/rspa.1964.0019.

[151] J. Hubbard. “Electron Correlations in Narrow Energy Bands. III. An Improved Solution”. In: *Proceedings of the Royal Society A: Mathematical, Physical and Engineering Sciences* 281.1386 (Sept. 22, 1964), pp. 401–419. URL: http://rspa.royalsocietypublishing.org/cgi/doi/10.1098/rspa.1964.0190.

[152] J. Hubbard. “Electron Correlations in Narrow Energy Bands. IV. The Atomic Representation”. In: *Proceedings of the Royal Society A: Mathematical, Physical and Engineering Sciences* 285.1403 (May 11, 1965), pp. 542–560. URL: http://rspa.royalsocietypublishing.org/cgi/doi/10.1098/rspa.1965.0124.

[153] J. Hubbard. “Electron correlations in narrow energy bands. v. a perturbation expansion about the atomic limit”. In: *Proceedings of the Royal Society of London A: Mathematical, Physical and Engineering Sciences*. Vol. 296. The Royal Society, 1967, pp. 82–99.

[154] J. Hubbard. “Electron Correlations in Narrow Energy Bands. VI. The Connexion with Many-Body Perturbation Theory”. In: *Proceedings of the Royal Society A: Mathematical, Physical and Engineering Sciences* 296.1444 (Jan. 10, 1967), pp. 100–112. URL: http://rspa.royalsocietypublishing.org/cgi/doi/10.1098/rspa.1967.0008.

[155] Hal Tasaki. “The Hubbard model - an introduction and selected rigorous results”. In: *Journal of Physics: Condensed Matter* 10.20 (May 25, 1998), pp. 4353–4378. URL: http://stacks.iop.org/0953-8984/10/i=20/a=004?key=crossref.4f1adfb655c30a4a8d6369e44259f4a5.

[156] Fabian H. L. Essler et al. *The One-Dimensional Hubbard Model*. Cambridge: Cambridge University Press, 2005. ISBN: 978-0-511-53484-3 978-0-521-80262-8 978-0-521-14394-3. URL: https://www.cambridge.org/core/product/identifier/9780511534843/type/book.

[157] Elliott H. Lieb. “The Hubbard model: Some Rigorous Results and Open Problems”. In: *Condensed Matter Physics and Exactly Soluble Models*. Ed. by Bruno Nachtergaele, Jan Philip Solovej, and Jakob Yngvason. Berlin, Heidelberg: Springer Berlin Heidelberg, 2004, pp. 59–77. ISBN: 978-3-642-06093-9 978-3-662-06390-3. URL: http://link.springer.com/10.1007/978-3-662-06390-3_4.

[158] S. Akbar Jafari. “Introduction to Hubbard model and exact diagonalization”. In: *arXiv preprint arXiv:0807.4878* (2008).

[159] Antoine Georges et al. “Dynamical mean-field theory of strongly correlated fermion systems and the limit of infinite dimensions”. In: *Reviews of Modern Physics* 68.1 (Jan. 1, 1996), pp. 13–125. URL: https://link.aps.org/doi/10.1103/RevModPhys.68.13.

[160] Wei-Feng Tsai and Steven A. Kivelson. “Superconductivity in inhomogeneous Hubbard models”. In: *Physical Review B* 73.21 (June 9, 2006). URL: http://link.aps.org/doi/10.1103/PhysRevB.73.214510.

[161] Wei-Feng Tsai et al. “Optimal inhomogeneity for superconductivity: Finite-size studies”. In: *Physical Review B* 77.21 (June 4, 2008). URL: http://link.aps.org/doi/10.1103/PhysRevB.77.214502.

[162] N. Bulut. “d x 2 - y 2 superconductivity and the Hubbard model”. In: *Advances in Physics* 51.7 (Nov. 2002), pp. 1587–1667. URL: http://www.tandfonline.com/doi/abs/10.1080/00018730210155142.

[163] A.-M. S. Tremblay, B. Kyung, and D. Sénéchal. “Pseudogap and high-temperature superconductivity from weak to strong coupling. Towards a quantitative theory (Review Article)”. In: *Low Temperature Physics* 32.4 (Apr. 2006), pp. 424–451. URL: http://aip.scitation.org/doi/10.1063/1.2199446.

[164] Rok Žitko. “SNEG – Mathematica package for symbolic calculations with second-quantization-operator expressions”. In: *Computer Physics Communications* 182.10 (Oct. 2011), pp. 2259–2264. URL: http://linkinghub.elsevier.com/retrieve/pii/S0010465511001792.

[165] B Bauer et al. “The ALPS project release 2.0: open source software for strongly correlated systems”. In: *Journal of Statistical Mechanics: Theory and Experiment* 2011.5 (May 4, 2011), P05001. URL: http://stacks.iop.org/1742-5468/2011/i=05/a=P05001?key=crossref.daddd50b02cf756d327700cf9019e11a.

[166] R. Schumann. “Thermodynamics of a 4-site Hubbard model by analytical diagonalization”. In: *arXiv preprint cond-mat/0101476* (2001). URL: http://arxiv.org/abs/cond-mat/0101476.

[167] Omjyoti Dutta et al. “Non-standard Hubbard models in optical lattices: a review”. In: *Reports on Progress in Physics* 78.6 (June 1, 2015), p. 066001. URL: http://stacks.iop.org/0034-4885/78/i=6/a=066001?key=crossref.01377f11f365801cf5357ba2b9bf9ee1.

[168] Michał Maik et al. “Density-dependent tunneling in the extended Bose–Hubbard model”. In: *New Journal of Physics* 15.11 (Nov. 20, 2013), p. 113041. URL: http://stacks.iop.org/1367-2630/15/i=11/a=113041?key=crossref.99a6f320c2f4cfacf3d566b820d6801d.

[169] F. Meinert et al. “Quantum Quench in an Atomic One-Dimensional Ising Chain”. In: *Physical Review Letters* 111.5 (July 31, 2013). URL: https://link.aps.org/doi/10.1103/PhysRevLett.111.053003.

[170] Ole Jürgensen et al. “Observation of Density-Induced Tunneling”. In: *Physical Review Letters* 113.19 (Nov. 7, 2014). URL: https://link.aps.org/doi/10.1103/PhysRevLett.113.193003.

[171] G. K. Campbell. “Imaging the Mott Insulator Shells by Using Atomic Clock Shifts”. In: *Science* 313.5787 (Aug. 4, 2006), pp. 649–652. URL: http://www.sciencemag.org/cgi/doi/10.1126/science.1130365.

[172] Sebastian Will et al. “Time-resolved observation of coherent multi-body interactions in quantum phase revivals”. In: *Nature* 465.7295 (May 2010), pp. 197–201. URL: http://www.nature.com/articles/nature09036.

[173] K A Chao, J Spalek, and A M Oles. “Kinetic exchange interaction in a narrow S-band”. In: *Journal of Physics C: Solid State Physics* 10.10 (May 28, 1977), pp. L271–L276. URL: http://stacks.iop.org/0022-3719/10/i=10/a=002?key=crossref.fbbec591eca85001d6d14108a6dd45a0.

[174] Jozef Spalek. “tJ model then and now: a personal perspective from the pioneering times”. In: *arXiv preprint arXiv:0706.4236* (2007).

[175] V. Yu. Irkhin. “Derivation of the t - J model: Electron spectrum and exchange interactions in narrow energy bands”. In: *Physical Review B* 57.21 (June 1, 1998), pp. 13375–13378. URL: https://link.aps.org/doi/10.1103/PhysRevB.57.13375.

[176] Simone Hamerla. *Systematic derivation of generalized t-J models from Hubbard models in one and two dimensions at and away from half-filling*. 2009. URL: http://t1.physik.tu-dortmund.de/files/uhrig/diploma/diploma_Hamerla_Simone_2009-09.pdf.

[177] A. Auerbach. “Quantum Magnetism Approaches to Strongly Correlated Electrons”. In: *arXiv:cond-mat/9801294* (Jan. 28, 1998). arXiv: cond-mat/9801294. URL: http://arxiv.org/abs/cond-mat/9801294.

[178] Elbio Dagotto. “Correlated electrons in high-temperature superconductors”. In: *Reviews of Modern Physics* 66.3 (July 1, 1994), pp. 763–840. URL: https://link.aps.org/doi/10.1103/RevModPhys.66.763.

[179] J. Jaklič and P. Prelovšek. “Finite-temperature properties of doped antiferromagnets”. In: *Advances in Physics* 49.1 (Jan. 2000), pp. 1–92. URL: http://www.tandfonline.com/doi/abs/10.1080/000187300243381.

[180] G. Baskaran, Z. Zou, and P.W. Anderson. “The resonating valence bond state and high-Tc superconductivity — A mean field theory”. In: *Solid State Communications* 63.11 (Sept. 1987), pp. 973–976. URL: http://linkinghub.elsevier.com/retrieve/pii/0038109887906429.

[181] Y. Hasegawa and D. Poilblanc. “Hole dynamics in the t-J model: An exact diagonalization study”. In: *Physical Review B* 40.13 (Nov. 1, 1989), pp. 9035–9043. URL: https://link.aps.org/doi/10.1103/PhysRevB.40.9035.

[182] T. Barnes et al. “Detailed Lanczos study of one- and two-hole band structure and finite-size effects in the t-J model”. In: *Physical Review B* 45.1 (Jan. 1, 1992), pp. 256–265. URL: https://link.aps.org/doi/10.1103/PhysRevB.45.256.

[183] Michael Brunner, Fakher F. Assaad, and Alejandro Muramatsu. “Single-hole dynamics in the t - J model on a square lattice”. In: *Physical Review B* 62.23 (Dec. 15, 2000), pp. 15480–15492. URL: https://link.aps.org/doi/10.1103/PhysRevB.62.15480.

[184] W.-F. Tsai. “Inhomogeneous Hubbard models”. PhD thesis. University of California, Los Angeles, 2008.

[185] *Advanced Solid State Theory*. URL: https://itp.uni-frankfurt.de/~lb/solidstateII09/problems/ps12.pdf.

[186] Assa Auerbach. *Interacting Electrons and Quantum Magnetism*. Graduate Texts in Contemporary Physics. New York: Springer-Verlag, 1994. ISBN: 978-0-387-94286-5. URL: //www.springer.com/us/book/9780387942865.

[187] Eva Pavarini and Institute for Advanced Simulation, eds. *The LDA+DMFT approach to strongly correlated materials: Autumn school organized by the DFG Research Unit 1346 Dynamical Mean-Field Approach with Predictive Power for Strongly Correlated Materials at Forschungszentrum Jülich, 4-7 October 2011 ; Lecture notes*. Schriften des Forschungszentrums Jülich Reihe Modeling and Simulation 1. Jülich: Forschungszentrum Jülich, 2011. ISBN: 978-3-89336-734-4.

[188] K. Eckert et al. “Quantum Correlations in Systems of Indistinguishable Particles”. In: *Annals of Physics* 299.1 (July 2002), pp. 88–127. URL: http://linkinghub.elsevier.com/retrieve/pii/S0003491602962688.

[189] K. Winkler et al. “Repulsively bound atom pairs in an optical lattice”. In: *Nature* 441.7095 (June 15, 2006), pp. 853–856. URL: http://www.nature.com/doifinder/10.1038/nature04918.

[190] G. J. Pryde and A. G. White. “Creation of maximally entangled photon-number states using optical fiber multiports”. In: *Physical Review A* 68.5 (Nov. 21, 2003). URL: http://link.aps.org/doi/10.1103/PhysRevA.68.052315.

[191] R. Egger et al. “Crossover from Fermi liquid to Wigner molecule behavior in quantum dots”. In: *Physical review letters* 82.16 (1999), p. 3320. URL: http://journals.aps.org/prl/abstract/10.1103/PhysRevLett.82.3320.

[192] C. Ellenberger et al. “Excitation Spectrum of Two Correlated Electrons in a Lateral Quantum Dot with Negligible Zeeman Splitting”. In: *Physical Review Letters* 96.12 (Mar. 2006). URL: http://link.aps.org/doi/10.1103/PhysRevLett.96.126806.

[193] Achintya Singha et al. “Correlated Electrons in Optically Tunable Quantum Dots: Building an Electron Dimer Molecule”. In: *Physical Review Letters* 104.24 (June 15, 2010). URL: http://link.aps.org/doi/10.1103/PhysRevLett.104.246802.

[194] Gerald Hönig et al. “Manifestation of unconventional biexciton states in quantum dots”. In: *Nature Communications* 5 (Dec. 16, 2014), p. 5721. URL: http://www.nature.com/doifinder/10.1038/ncomms6721.

[195] Yuesong Li, Constantine Yannouleas, and Uzi Landman. “Three-electron anisotropic quantum dots in variable magnetic fields: Exact results for excitation spectra, spin structures, and entanglement”. In: *Physical Review B* 76.24 (Dec. 11, 2007). URL: http://link.aps.org/doi/10.1103/PhysRevB.76.245310.

[196] R. Schumann. *Analytical form of eigenvectors of a 4-site Hubbard model*. URL: https://www.physik.tu-dresden.de/itp/members/schumann/4site.html (visited on 03/20/2018).

[197] Patrik. Fazekas. *Lecture notes on electron correlation and magnetism*. Series in modern condensed matter physics ; vol. 5. Singapore ; River Edge, NJ: World Scientific, 1999. xvi+777. ISBN: 978-981-02-2474-5.

[198] M. Roncaglia, G. Sierra, and M. A. Martin-Delgado. “Dimer–resonating valence bond state of the four-leg Heisenberg ladder: Interference among resonances”. In: *Physical Review B* 60.17 (Nov. 1, 1999), pp. 12134–12137. URL: https://link.aps.org/doi/10.1103/PhysRevB.60.12134.

[199] A. M. Rey et al. “Controlled preparation and detection of d-wave superfluidity in two-dimensional optical superlattices”. In: *EPL (Europhysics Letters)* 87.6 (Sept. 1, 2009), p. 60001. URL: http://stacks.iop.org/0295-5075/87/i=6/a=60001?key=crossref.4595511ec9b5a803034b249fddbd2b74.

[200] Simon Trebst et al. “d -Wave Resonating Valence Bond States of Fermionic Atoms in Optical Lattices”. In: *Physical Review Letters* 96.25 (June 29, 2006). URL: http://link.aps.org/doi/10.1103/PhysRevLett.96.250402.

[201] N. B. Christensen et al. “Quantum dynamics and entanglement of spins on a square lattice”. In: *Proceedings of the National Academy of Sciences* 104.39 (Sept. 25, 2007), pp. 15264–15269. URL: http://www.pnas.org/cgi/doi/10.1073/pnas.0703293104.

[202] P W Anderson et al. “The physics behind high-temperature superconducting cuprates: the plain vanilla version of RVB”. In: *Journal of Physics: Condensed Matter* 16.24 (June 23, 2004), R755–R769. URL: http://stacks.iop.org/0953-8984/16/i=24/a=R02?key=crossref.38f5639cca68caa4782c9835db3a7cb5.

[203] Masao Ogata and Hidetoshi Fukuyama. “The *t* – J model for the oxide high- T $_{c}$ superconductors”. In: *Reports on Progress in Physics* 71.3 (Mar. 1, 2008), p. 036501. URL: http://stacks.iop.org/0034-4885/71/i=3/a=036501?key=crossref.32783ad89bee9b27f75e50a35b650215.

[204] F. C. Zhang and T. M. Rice. “Effective Hamiltonian for the superconducting Cu oxides”. In: *Physical Review B* 37.7 (Mar. 1, 1988), pp. 3759–3761. URL: https://link.aps.org/doi/10.1103/PhysRevB.37.3759.

[205] Józef Spałek, Michał Zegrodnik, and Jan Kaczmarczyk. “Universal properties of high-temperature superconductors from real-space pairing: t - J - U model and its quantitative comparison with experiment”. In: *Physical Review B* 95.2 (Jan. 13, 2017). URL: https://link.aps.org/doi/10.1103/PhysRevB.95.024506.

[206] Ehud Altman and Assa Auerbach. “Plaquette boson-fermion model of cuprates”. In: *Physical Review B* 65.10 (Feb. 14, 2002). URL: http://link.aps.org/doi/10.1103/PhysRevB.65.104508.

[207] S.S. Hodgman et al. “Solving the Quantum Many-Body Problem via Correlations Measured with a Momentum Microscope”. In: *Physical Review Letters* 118.24 (June 14, 2017). URL: http://link.aps.org/doi/10.1103/PhysRevLett.118.240402.

[208] Marie Bonneau et al. “Characterizing two-particle entanglement in a double-well potential”. In: *arXiv:1711.08977 [cond-mat, physics:physics, physics:quant-ph]* (Nov. 24, 2017). arXiv: 1711.08977. URL: http://arxiv.org/abs/1711.08977.

[209] Simon Fölling et al. “Spatial quantum noise interferometry in expanding ultracold atom clouds”. In: *Nature* 434.7032 (Mar. 2005), pp. 481–484. URL: http://www.nature.com/articles/nature03500.

[210] T. Rom et al. “Free fermion antibunching in a degenerate atomic Fermi gas released from an optical lattice”. In: *Nature* 444.7120 (Dec. 2006), pp. 733–736. URL: http://www.nature.com/articles/nature05319.

[211] Bess Fang et al. “Momentum-Space Correlations of a One-Dimensional Bose Gas”. In: *Physical Review Letters* 116.5 (Feb. 2, 2016). URL: https://link.aps.org/doi/10.1103/PhysRevLett.116.050402.

[212] P. Treutlein et al. “Quantum information processing in optical lattices and magnetic microtraps”. In: *Fortschritte der Physik* 54.8 (Aug. 23, 2006), pp. 702–718. URL: http://doi.wiley.com/10.1002/prop.200610325.

[213] Rajibul Islam et al. “Measuring entanglement entropy in a quantum many-body system”. In: *Nature* 528.7580 (Dec. 2, 2015), pp. 77–83. URL: http://www.nature.com/doifinder/10.1038/nature15750.

[214] Constantine Yannouleas and Uzi Landman. “Symmetry breaking and quantum correlations in finite systems: studies of quantum dots and ultracold Bose gases and related nuclear and chemical methods”. In: *Reports on Progress in Physics* 70.12 (Dec. 1, 2007), pp. 2067–2148. URL: http://stacks.iop.org/0034-4885/70/i=12/a=R02?key=crossref.a87571c73f468fd22015f9bd887ae1fa.

[215] Igor Romanovsky, Constantine Yannouleas, and Uzi Landman. “Crystalline Boson Phases in Harmonic Traps: Beyond the Gross-Pitaevskii Mean Field”. In: *Physical Review Letters* 93.23 (Dec. 2004). URL: http://link.aps.org/doi/10.1103/PhysRevLett.93.230405.

[216] Leslie O. Baksmaty, Constantine Yannouleas, and Uzi Landman. “Rapidly rotating boson molecules with long- or short-range repulsion: An exact diagonalization

study". In: *Physical Review A* 75.2 (Feb. 26, 2007). URL: http://link.aps.org/doi/10.1103/PhysRevA.75.023620.

[217] M A García-March et al. "Quantum correlations and spatial localization in one-dimensional ultracold bosonic mixtures". In: *New Journal of Physics* 16.10 (Oct. 8, 2014), p. 103004. URL: http://stacks.iop.org/1367-2630/16/i=10/a=103004?key=crossref.a65c8f855402dab9a39318802aa80f4e.

[218] L. Mathey, A. Vishwanath, and E. Altman. "Noise correlations in low-dimensional systems of ultracold atoms". In: *Physical Review A* 79.1 (Jan. 14, 2009). URL: https://link.aps.org/doi/10.1103/PhysRevA.79.013609.

[219] Ehud Altman, Eugene Demler, and Mikhail D. Lukin. "Probing many-body states of ultracold atoms via noise correlations". In: *Physical Review A* 70.1 (July 6, 2004). URL: https://link.aps.org/doi/10.1103/PhysRevA.70.013603.

[220] M. Alvioli et al. "Universality of nucleon-nucleon short-range correlations: Two-nucleon momentum distributions in few-body systems". In: *Physical Review C* 85.2 (Feb. 17, 2012). URL: https://link.aps.org/doi/10.1103/PhysRevC.85.021001.

[221] C. A. Coulson. "Momentum Distribution in Molecular Systems". In: *Mathematical Proceedings of the Cambridge Philosophical Society* 37.1 (Jan. 1941), p. 55. URL: http://www.journals.cambridge.org/abstract_S0305004100021526.

[222] C. K. Hong, Z. Y. Ou, and L. Mandel. "Measurement of subpicosecond time intervals between two photons by interference". In: *Physical Review Letters* 59.18 (Nov. 2, 1987), pp. 2044–2046. URL: https://link.aps.org/doi/10.1103/PhysRevLett.59.2044.

[223] R. C. Liu et al. "Quantum interference in electron collision". In: *Nature* 391.6664 (Jan. 1998), pp. 263–265. URL: http://www.nature.com/articles/34611.

[224] E. Bocquillon et al. "Coherence and Indistinguishability of Single Electrons Emitted by Independent Sources". In: *Science* 339.6123 (Mar. 1, 2013), pp. 1054–1057. URL: http://www.sciencemag.org/cgi/doi/10.1126/science.1232572.

[225] R. Lopes et al. "Atomic Hong–Ou–Mandel experiment". In: *Nature* 520.7545 (Apr. 2015), pp. 66–68. URL: http://www.nature.com/articles/nature14331.

[226] Ruben Pauncz. *The Construction of Spin Eigenfunctions: An Exercise Book*. Springer US, 2000. ISBN: 978-0-306-46400-3. URL: //www.springer.com/us/book/9780306464003.

[227] Ruben Pauncz. *Spin Eigenfunctions: Construction and Use*. Springer US, 1979. ISBN: 978-1-4684-8528-8. URL: //www.springer.com/us/book/9781468485288.